ABSTRACT

Title of dissertation:	AN INVESTIGATION OF THE PARAMETERIZED PREDICTION OF LIGHTNING IN CLOUD-RESOLVED CONVECTION AND THE RESULTING CHEMISTRY
	Kristin Ashley Cummings, Doctor of Philosophy, 2017
Dissertation directed by:	Visiting Research Professor Kenneth E. Pickering Department of Atmospheric and Oceanic Science

The Deep Convective Clouds and Chemistry (DC3) field campaign provided a unique set of observations to further investigate the role lightning and lightning-generated nitrogen oxides (LNO_x) have on the composition of the upper troposphere. With the Weather Research and Forecasting model coupled with Chemistry (WRF-Chem), a cloud-resolved simulation of the 29-30 May 2012 severe supercell system investigated 18 flash rate parameterization schemes (FRPSs), the mean LNO_x production flash^{-1}, and the transport and distribution of other trace gases.

Most of the observed storm's meteorological and chemical conditions were well represented when the model included convective damping and lightning data assimilation techniques. Newly-developed FRPSs based on DC3 radar observations and Lightning Mapping Array (LMA) data are implemented in the model, along with previously developed schemes from the literature. The schemes are based on relationships between lightning and various kinematic, structural, and microphysical thunderstorm characteristics available in the model. The results suggest the simulated graupel and

snow/ice hydrometeors require scaling factors to more closely represent proxy observations. The model flash rates generated over the simulation period are compared with LMA observations. Thirteen FRPSs overpredicted flashes by > 100%. Generally, FRPSs based on storm kinematics and structure (particularly updraft volume) perform slightly better than schemes based on hydrometeors. However, the upward cloud ice flux FRPS best represents the observed lightning.

The 10 WRF-Chem simulations included one run with no LNO_x and nine runs with different LNO_x production scenarios. The simulated CO and O_3 are within 1% and 3% of aircraft observations, respectively, when compared with one model layer lower, which suggests the model slightly underestimates the convective transport. A LNO_x production scenario of 82 moles flash^{-1} best represents the observed NO_x mixing ratios in anvil outflow when combined with the observed flash channel vertical profiles and intracloud to cloud-to-ground ratios. This estimate is smaller than the mean 250 moles NO flash^{-1} suggested for a typical thunderstorm, but within the lower end of the estimated range (33-660 moles fl^{-1}). Analysis of the convective outflow using observations made 12-24 hours downwind indicates the mean daytime photochemical O_3 production rate is about 1.6 ppbv hour^{-1}.

AN INVESTIGATION OF THE PARAMETERIZED PREDICTION OF LIGHTNING
IN CLOUD-RESOLVED CONVECTION AND THE RESULTING CHEMISTRY

by

Kristin Ashley Cummings

Dissertation submitted to the Faculty of the Graduate School of the
University of Maryland, College Park in partial fulfillment
of the requirements for the degree of
Doctor of Philosophy
2017

Advisory Committee:

Professor Sumant Nigam, Chair
Visiting Research Professor Kenneth Pickering, Advisor and Co-chair
Professor Eugenia Kalnay
Associate Research Scientist Dale Allen
Professor Neil Blough, Dean's Representative

ACKNOWLEDGEMENTS

TABLE OF CONTENTS

LIST OF TABLES

LIST OF FIGURES

LIST OF ABBREVIATIONS

°C	degrees Celsius
2D	two-dimensional
3D	three-dimensional
35EV	35 dBZ echo volume
45WS	45th Weather Squadron
ACTIVE	Aerosol and Chemical Transport in Tropical Convection
AMMA	African Monsoon Multidisciplinary Analysis
AMU	Applied Meteorology Unit
CAPE	convective available potential energy
CCAFS	Cape Canaveral Air Force Station
CG	cloud-to-ground
CH_4	methane
CH_2O	formaldehyde
CO	carbon monoxide
CO_2	carbon dioxide
CSU	Colorado State University
CTH	cloud top height
DART	Data Assimilation Research Testbed
dBZ	decibels of reflectivity
DC3	Deep Convective Clouds and Chemistry
DE	detection efficiency
DLA	diabatic Lagrangian analysis
DMSP	Defense Meteorological Satellite Program
ECMWF	European Centre for Medium-Range Weather Forecasting
ENTLN	Earth Networks Total Lightning Network
EOL	Earth Observing Laboratory
EOS	Earth Observing System
EPA	Environmental Protection Agency
EULINOX	European Lightning Nitrogen Oxides Project
f	total flash rate
FD	flash density
FLEXPART	Flexible Particle
FRPS	flash rate parameterization scheme
GEV	graupel echo volume
GEV5	GEV between -5 °C > temperature > -40 °C
GEV10	GEV between -10 °C > temperature > -40 °C
GEV5S	GEV5 for supercells
GEV10S	GEV10 for supercells
GFS	Global Forecasting System
GLM	Geostationary Lightning Mapper
GOCART	Goddard Chemistry Aerosol Radiation and Transport
GOES-R	Geostationary Operational Environmental Satellite R-Series
GV	Gulfstream-V

H_2O_2	hydrogen peroxide
HNO_3	nitric acid
HYSPLIT	Hybrid Single-Particle Lagrangian Integrated Trajectory
hPa	hectoPascals
HRRR	High-Resolution Rapid Refresh
IC	intracloud
IC:CG	intracloud to cloud-to-ground ratio
ICEFLUX	upward cloud ice flux
IMFP	ice mass flux product
IOP	intensive operational period
ISCCP	International Satellite Cloud Climatology Project
ISS	International Space Station
IWP	ice water path
KPP	Kinetic PreProcessor
KSC	Kennedy Space Center
LCL	lifting condensation left
LDA	lightning data assimilation
LDAR	Lightning Detection and Ranging
LF	low frequency
LINET	lightning detection network
LIS	Lightning Imaging Sensor
LMA	lightning mapping array
LNO_x	lightning-generated nitrogen oxides
LNOM	Lightning Nitrogen Oxides Model
LSM	land surface model
LTG3	McCaul blended lightning threat method
M	third body
MCS	mesoscale convective system
MGAUS	Mobile GPS Advanced Upper-Air Sounding System
MLCAPE	mixed-layer convective available potential energy
MOZART	Model for Ozone and Related chemical Tracers
MSFC	Marshall Space Flight Center
MYJ	Mellor-Yamada-Janjic
N	nitrogen
NAM-ANL	North American Mesoscale Analysis
NARR	North American Regional Reanalysis
NASA	National Aeronautics and Space Administration
NCAPE	normalized convective available potential energy
NCAR	National Center for Atmospheric Research
NCEP	National Centers for Environmental Prediction
NEXRAD	Next Generation Radar
NLDN	National Lightning Detection Network
N_2	molecular nitrogen
NO	nitric oxide
NO_2	nitrogen dioxide
NO_x	nitrogen oxides

NOAA	National Oceanic and Atmospheric Administration
NOXP	NOAA X-band polarimetric
NSSL	National Severe Storms Laboratory
O_2	molecular oxygen
O_3	ozone
OH	hydroxyl radical
OMI	Ozone Monitoring Instrument
ONERA	Office Nationale d'Etudes et de Recherches Aerospatiales
OTD	Optical Transient Detector
PAN	peroxyacetyl nitrate
PBL	planetary boundary layer
PIM	precipitation ice mass
ppbv	parts per billion volume
pptv	parts per trillion volume
R	organic group
RH	hydrocarbon
RO_2	organic peroxy radical
RRTMG	Rapid radiative transfer model for General Circulation Models
SCOUT-O3	Stratospheric-Climate Links with Emphasis on the Upper Troposphere and Lower Stratosphere
SIP	State Implementation Plan
SMART	Shared Mobile Atmospheric Research Teaching
STEPS	Severe Thunderstorm Electrification and Precipitation Study
STERAO-A	Stratospheric-Tropospheric Experiment: Radiation, Aerosols and Ozone
TELEX	Thunderstorm Electrification and Lightning Experiment
TRMM	Tropical Rainfall Measuring Mission
TROCCINOX	Tropical Convection, Cirrus and Nitrogen Oxides Experiment
UAH	University of Alabama in Huntsville
UTC	Coordinated Universal Time
UV	updraft volume
UVS	UV for supercells
VHF	very high frequency
VII	vertically integrated ice
VLF	very low frequency
vts	snow fall speed
w	vertical velocity
w_{max}	maximum vertical velocity
WRF	Weather Research and Forecasting
WRF-AqChem	Weather Research and Forecasting model coupled with a simple gas and aqueous chemistry module
WRF-Chem	Weather Research and Forecasting model coupled with Chemistry
WSR-88D	Weather Surveillance Radar-1988 Doppler
YSU	Yonsei University

CHAPTER 1: INTRODUCTION

1.1 Motivation

Lightning prediction is desirable in weather forecasting models and is necessary in chemistry and climate models. Prior to the 1970s the lack of adequate detection techniques made it difficult to analyze global lightning activity or determine relationships between lightning and storm parameters that could be employed in prediction schemes; however, lightning detection instrumentation has evolved over time. The first optical sensor that orbited Earth could only observe lightning at night (Turman, 1978; Orville and Henderson, 1986). Over the next forty years advancements in detection technology (e.g., optical, magnetic direction finding, and time-of-arrival sensors) allowed for improvements in detection efficiency, spatial accuracy, the ability to distinguish between cloud-to-ground (CG) and intracloud (IC) lightning, and three-dimensional (3D) mapping of total lightning activity (Rison et al., 1999; Krehbiel et al., 2000; Christian et al., 2003; Thomas et al., 2004; Cummins and Murphy, 2009; Heckman and Liu, 2010; Liu and Heckman, 2011).

The availability of high-detection-efficiency flash data, together with radar observations or model data, has allowed the development of flash rate parameterization schemes (FRPSs; relationships between lightning activity and thunderstorm characteristics) to estimate lightning flash rates and location. Currently lightning threat forecasts (McCaul et al., 2009; 2011) are being run in operational models to predict lightning flash rate densities in short-range weather forecasts (i.e., 12-72 hours). These models include the National Severe Storms Laboratory (NSSL) Weather Research and

Forecasting (WRF) model (McCaul et al., 2011), the National Oceanic and Atmospheric

Administration (NOAA)/National Centers for Environmental Prediction (NCEP) High-

Resolution Rapid Refresh (HRRR) model (Wong et al., 2013), the National Center for

Atmospheric Research (NCAR) ensemble forecast (Schwartz et al., 2015), and the United

Kingdom (UK) Met Office UK-variable resolution (UKV) model (Wilkinson and

Bornemann, 2014). Giannaros et al. (2016) evaluated operational lightning forecasts in

Central-South Europe using the WRF model with a convective parameterization and

FRPS based on cloud top height (Price and Rind, 1992). Such forecasts are beneficial

from an operations and public safety perspective for those individuals who are required

or plan to spend an extended amount of time outdoors (e.g., construction, lawn care,

airports, rocket launch preparations, and recreational activities). In addition to

forecasting future lightning activity, FRPSs may be used to reproduce flash rates from

past convective events to verify their performance against lightning observations (Barthe

et al., 2010; Cummings et al., 2017a), generate model-simulated flash counts in areas

where observed lightning data are unavailable, or use observed total lightning activity to

estimate storm parameters that are not routinely measured or observed in real-time (e.g.,

cloud top height, updraft volume, and ice water path). Evaluating FRPS performance

through case studies may reveal that some schemes are more representative of a

particular latitude band, region, type of convection (e.g., airmass, multicell, and

supercell), or time of year than others. If true, models will benefit from capturing the

spatial and temporal variation of lightning through the use of FRPSs.

Additionally, FRPSs play a key role in calculating the production of lightning-

generated nitrogen oxides (LNO_x) and provide a means for the LNO_x production trend to

vary in time within a model. An accurate model replication of the observed flash rate as a function of time would provide researchers with additional details on the chemical influence of LNO_x within and downwind of a thunderstorm. As one of the largest natural sources of nitrogen oxides (NO_x = nitric oxide (NO) + nitrogen dioxide (NO_2)), lightning accounts for roughly 5 ± 3 Tg (N) yr^{-1}, or 10-15%, of the total NO_x budget (Schumann and Huntrieser, 2007). Other major sources of tropospheric NO_x include fossil fuel combustion, biomass burning, and microbial activity in soils (Schumann and Huntrieser, 2007). While the lower troposphere is mainly dominated by surface emissions, especially those due to human activity (Zhang et al., 2003), lightning is the largest source of NO_x in the upper troposphere, where most LNO_x is present above an altitude of 7 km (Martin et al., 2007). In this portion of the atmosphere, NO_x has a longer lifetime and a large influence on ozone (O_3) (e.g., Allen et al., 2010), a significant greenhouse gas (Lacis et al., 1990), with implications for indirectly having a positive radiative forcing on the climate. Following a convective event, enhancements in O_3 can be found downwind within the thunderstorm outflow (DeCaria et al., 2005; Ott et al., 2010; Martini et al., 2011). The enhancements in O_3 influence its radiative forcing, which maximizes near the tropopause. Nitrogen oxides are also important because they increase the hydroxyl radical (OH) concentration, which is known as the "detergent of the atmosphere" because of its ability to react with and remove various trace gas species (e.g., carbon monoxide (CO), carbon dioxide (CO_2), hydrocarbons, and NO_2) from the atmosphere. If a future climate features more lightning, the resulting greater OH will decrease the methane (CH_4) lifetime (Fiore et al., 2006), and have a negative forcing on tropospheric radiative forcing of climate.

Many factors affect the uncertainty of LNO_x production, including the variation in the type, length, energy, peak current, and number of lightning flashes (Price et al., 1997), as well as the location and strength of the convection. Although other natural and anthropogenic NO_x sources may have uncertainty ranges that are similar to or greater than that associated with lightning, the potential feedback mechanisms between lightning and surface temperatures makes narrowing the uncertainty range of LNO_x critical (Schumann and Huntrieser, 2007). In addition, a better understanding of the global LNO_x budget would be beneficial for properly modeling variations and trends in NO_x and O_3 and in analyzing the influence of other NO_x sources, such as the injection of stratospheric NO_x and aircraft emissions (Bond et al., 2001; Zhang et al. 2000).

Therefore, model-simulated lightning flash rates have the ability to enhance our knowledge of the role of LNO_x in global climate-chemistry models (e.g., Banerjee et al., 2014; Liaskos et al., 2015) and regional air quality models (e.g., Allen et al., 2012). Incorporation of these FRPSs in past and future model simulations is also valuable for furthering our understanding of the potential impacts of climate change on convection and the resulting lightning activity (Reeve and Toumi, 1999; Petersen and Rutledge, 2001; Williams, 2005; Price, 2009; Romps et al., 2014; Magi, 2015).

For FRPSs to be truly helpful to the atmospheric chemistry, lightning, and modeling communities, it is important to understand if there is variability in scheme performance by latitude zone, region, and storm type, and how schemes perform at different resolutions (e.g., cloud-resolved and global). To do this, thunderstorms from different environments and of differing updraft strength, size, and severity must be analyzed. In a study of storms over northern Alabama, Mecikalski and Carey (2017)

showed that the altitude and reflectivity where flashes initiate and propagate vary as a function of storm type (i.e., multicell, mesoscale convective systems, and supercell), thereby showing the importance of differentiating between various storm types when performing lightning-related studies. Barthe and Barth (2008) and Barthe et al. (2010) emphasize the need for modeling numerous convective case studies. Without understanding these variations, the true potential of the relationships between model storm parameters and total lightning activity will not be fully understood and the community will not be able to expand our knowledge of the impact of lightning in other areas (e.g., LNO_x, air quality, and climate).

By building on the successes of previous experiments, the Deep Convective Clouds and Chemistry (DC3) field campaign made simultaneous observations of the microphysics, dynamics, chemistry, and lightning within convective systems, which was something that had been lacking in prior field experiments (Barthe and Barth, 2008), in addition to post-convection observations of the outflow plume (Barth et al., 2015). The availability of this large, cohesive dataset provides the necessary ground and upper air measurements required for my further analysis of the electrical and chemical relationships within thunderstorms.

1.2 Objectives

The objectives of my research are to evaluate previously published and recently developed FRPSs in a cloud-resolved WRF model simulation of the 29-30 May 2012 Oklahoma severe supercell system (Bela et al., 2016; DiGangi et al., 2016; Pollack et al., 2016; Li et al., 2017) observed during DC3 (Barth et al., 2015) and to determine which scheme or schemes perform the best in representing the observed lightning flashes. To

address how LNO_x and other trace gases are influenced by convective transport and lightning flash rates, additional cloud-resolved simulations will be run using the WRF model coupled with Chemistry (WRF-Chem). The scientific questions that will be addressed include:

1. How does FRPS performance vary between schemes based on the model-simulated total flashes and flash rates?

2. Can a microphysically-based FRPS produce realistic predictions of flash rate in a cloud-resolved model?

3. How do observed versus default model vertical distributions of flash channel lengths and IC:CG ratios affect the model-simulated LNO_x and other trace gases in the anvil outflow?

4. Does LNO_x production per flash in a high flash rate Oklahoma storm vary from other midlatitude storms?

5. How do flash extent and flash energy relate to flash rate for an Oklahoma severe supercell system in comparison to other observed storms?

6. Is there a relationship between flash rate and LNO_x production per flash?

7. By how much is the upper tropospheric chemistry (e.g., O_3) in convective outflow affected by LNO_x?

Chapter 2 will discuss the processes involved in generating lightning, how lightning detection instrumentation has evolved over time, and how models can be used to predict lightning. The formation of LNO_x will be reviewed in Chapter 3, along with a

description of the available parameterization schemes and the chemical interactions that involve NO_x. An overview of the DC3 field experiment and the 29-30 May 2012 Oklahoma severe supercell system is provided in Chapter 4, including the available instrumentation and WRF model preparation. Chapter 5 will describe the WRF-Chem model set-up used to simulate the observed 29-30 May convective event and the modifications made to the model (e.g., convective damping, observation-based LNO_x placement, etc.). Chapter 6 reviews the methodologies and analyses used to investigate the model's performance in simulating the observed meteorological features and predicting lightning flash rates with FRPSs. The observed and model-simulated trace gases will be analyzed in Chapter 7 with a specific focus on the best LNO_x production scenario that represents the case study, as well as the relationships between lightning characteristics and LNO_x production. Chapter 8 will investigate how the trace gases observed by the aircraft in the storm anvil evolved in the outflow plume between the anvil and a flight approximately 24 hours downwind. Chapter 9 summarizes the key findings and Chapter 10 will provide a discussion of future work.

Chapters 2 and 6, along with introductory material from Chapters 1, 4, and 5 form the Cummings et al. (2017a) paper that has been submitted to the *Journal of Geophysical Research – Atmospheres.* The Cummings et al. (2017b) paper in preparation will contain the results in Chapters 7 and 8.

CHAPTER 2: LIGHTNING

2.1 Lightning formation

Lightning typically occurs in association with deep convective clouds, called

cumulonimbi, where the cloud top height is at an altitude greater than the freezing level.

Due to the tendency for thunderstorms to exhibit cold cloud characteristics, a mixed-

phase region often develops, which contains both supercooled droplets and ice particles

(Wallace and Hobbs, 2006). Lightning has occasionally been observed in warm clouds

whose vertical development does not reach the freezing level.

Currently, there are two theories that attempt to explain the electrical charge

distribution within a thunderstorm. According to the precipitation theory, as heavier

precipitation, such as graupel and hail, forms and falls through the cloud, collisions occur

with the smaller droplets and particles. Upon colliding and rebounding, the smaller and

larger hydrometeors exhibit opposite polarities. Generally, graupel and hail gain a

negative charge, while a positive charge is given to small droplets and particles.

However, the charge received by particles is also dependent on factors such as

temperature and riming rate (MacGorman and Rust, 1998; Uman, 2001; MacGorman et

al., 2005; Mansell et al., 2005; Lund et al., 2009). Charge separation is achieved as

updrafts, downdrafts, and gravity transport the cloud and precipitation particles within the

cloud. Although the precipitation theory is more widely accepted, some researchers

believe the convection theory is responsible for a thunderstorm's charge structure. Based

on this theory, positive charge is transported from the earth's surface to the cloud's

interior via updrafts and negative charge is carried by downward motion of the cloud

boundary from the negative screening layer at the cloud top, along the cloud's sides, and into the lower cloud interior (MacGorman and Rust, 1998; Uman, 2001).

Following either theory, the electric charge distribution in a thunderstorm generally exhibits a positive dipole structure with a negative charge center in the lower region of the convective cloud and a positive charge center in the upper portion (Figure 1a; MacGorman and Rust, 1998). Sometimes the thunderstorm may display a positive tripole structure, where a second, but smaller, positively charged region is also present near the base of the cloud (Figure 1b). Although atypical, thunderstorms may also exhibit an inverted-polarity structure, where the altitudes of the negative and positive charge regions reverse within the cloud (Figure 1c and 1d; Rust et al., 2005).
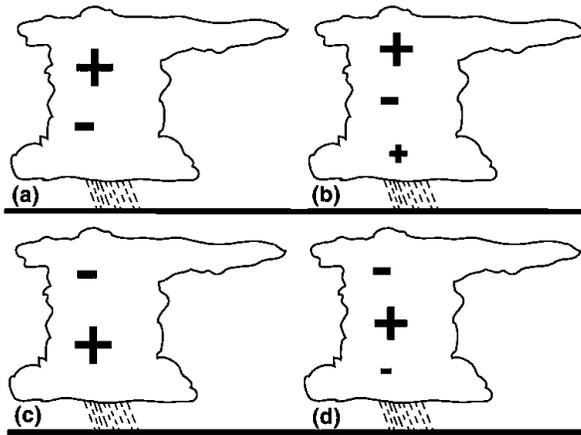
Figure 1. Schematic of a (1a) dipole, (1b) tripole, (1c) inverted dipole, and (1d) inverted tripole charge structure within a thunderstorm (from Kuhlman et al., 2006).

The charge separation continues until the air can no longer maintain the strength of the electric field in the storm. The typical electric field within a thunderstorm is less than 200 kV m^{-1} with a mean of 50 kV m^{-1} and a maximum of 400 kV m^{-1} (Price et al., 1997; Stolzenburg et al., 2007). When the critical threshold is reached, a lightning flash occurs. This threshold is dependent on air density and decreases with altitude (Gurevich

and Zybin, 2005). Lightning flashes occur between cloud and ground (CG flashes), between different portions of the cloud (IC flashes), between clouds (cloud-to-cloud flashes), or between cloud and air (Schumann and Huntrieser, 2007). Researchers initially suggested the global lightning flash rate was roughly 100 flashes s^{-1}, but this estimate has decreased in recent years (~46 flashes s^{-1}) due to satellite observations (Cecil et al., 2014).

Approximately 44,000 thunderstorms occur each day around the globe (Huntrieser et al., 1998), with most lightning occurring over the land versus the ocean (Figure 2). Two theories support this observation. The thermal hypothesis suggests the land surface, which is hotter than the ocean, generates strong lifting necessary to produce a deep mixed-phase region. Over the ocean, clouds contain fewer droplets, but they are larger than in continental clouds. This reduces cloud buoyancy, which decreases updraft strength and limits the vertical development of the mixed-phase region. The aerosol hypothesis suggests the air over land contains more aerosols, which act to reduce cloud droplet size, suppress precipitation, and increase the mixed-phase region (Cooray, 2003; Williams, 2005; Schumann and Huntrieser, 2007).

Thunderstorms form almost every day in the tropics, unlike other regions of the globe (Figure 3; Huntrieser et al., 2011), with the majority of the earth's lightning occurring within the tropical belt between ±30° latitude (Cooray, 2003; Schumann and Huntrieser, 2007). In the midlatitudes, thunderstorms primarily occur in the spring and summer. With longer days and a higher angle of incoming solar radiation, the land surface is hotter and the overlying air can become unstable. Therefore, lightning is most common in the Northern Hemisphere where a greater percentage of earth's surface is

composed of land, unlike the Southern Hemisphere, which is largely ocean (Cooray, 2003; Schumann and Huntrieser, 2007). Due to these land surface differences, lightning occurs roughly 1.2 times more often in the Northern Hemisphere summer versus winter (Schumann and Huntrieser, 2007). In the United States, lightning occurs most frequently in the southeast during summer (Zhang et al., 2003). Lightning is not as common during the winter because lifting is primarily at the synoptic scale and there is not as much water vapor available to fully develop the mixed-phase region (Cooray, 2003).
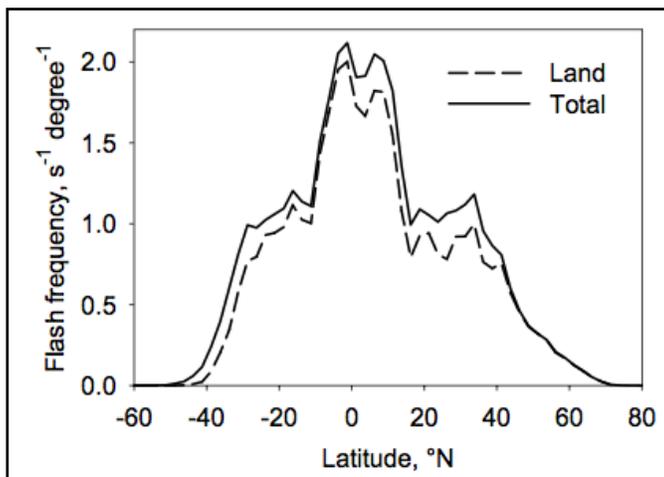
Figure 2. Contribution of lightning flashes over land to the total mean flash frequency (land and ocean) by latitude (from Schumann and Huntrieser, 2007). Observations were taken from the OTD from April 1995 to March 2000.
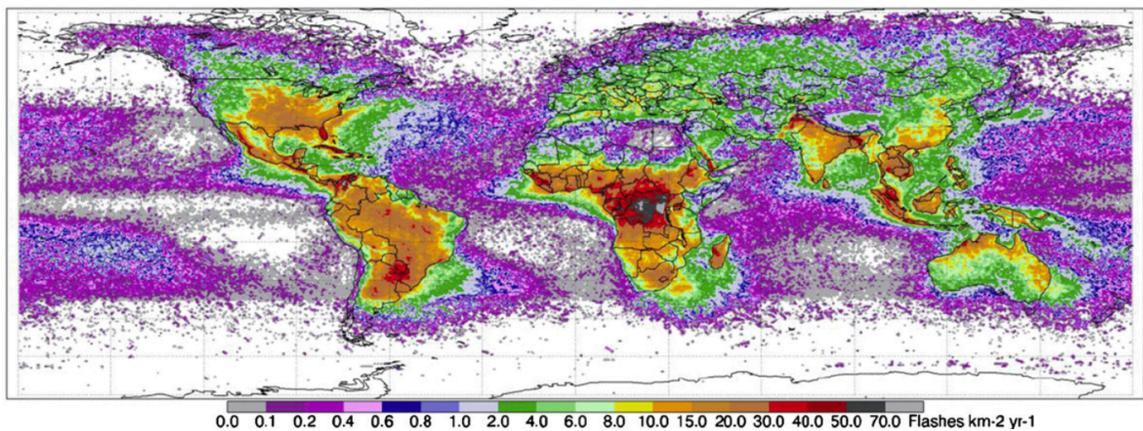
Figure 3. Mean annual flash rate detected by LIS and OTD on a high resolution 0.5° × 0.5° grid (from Cecil et al., 2014).

2.2 Evolution of lightning instrumentation

Prior to the 1970s the lack of adequate detection techniques made it difficult to analyze global lightning activity or determine relationships between lightning and storm parameters that could be employed in prediction schemes; however, lightning detection instrumentation has evolved over time. Lightning observations improved spatially with the development of the Defense Meteorological Satellite Program (DMSP). The first optical sensor that orbited Earth onboard DMSP satellite 8531 could only observe lightning at night (Turman, 1978; Orville and Henderson, 1986). Over the next forty years advancements in detection technology (e.g., optical, magnetic direction finding, and time-of-arrival sensors) allowed for improvements in detection efficiency, spatial accuracy, the ability to distinguish between CG and IC lightning, and 3D mapping of total lightning activity (Rison et al., 1999; Krehbiel et al., 2000; Christian et al., 2003; Thomas et al., 2004; Cummins and Murphy, 2009; Heckman and Liu, 2010; Liu and Heckman, 2011).

Observations were first collected for CG, IC, and cloud-to-cloud lightning between ±75° latitude, both day and night, with the launch of the Optical Transient Detector (OTD) on the MicroLab-1 satellite in April 1995 (Christian et al., 2003). Before the OTD mission ended in March 2000, the Lightning Imaging Sensor (LIS) was launched in November 1997 aboard the Tropical Rainfall Measuring Mission (TRMM) satellite. While both OTD and LIS observed lightning based on changes in the optical scene, LIS could observe lightning flashes at a storm-scale resolution, but only between ±38° latitude (Blakeslee et al., 2014; Buechler et al., 2014).

Two-dimensional (2D) ground-based observations are available from several sources. The National Lightning Detection Network (NLDN) was established in 1989 and has gone through several upgrades over the last 25 years. More than 100 sensors make up the network, which uses magnetic direction finding and time-of-arrival techniques to detect the low frequency (LF) and very low frequency (VLF) emissions released by flashes occurring over the continental United States and several hundred kilometers off the coast (LaJoie and Laing, 2008; Orville, 2008; Vaisala, 2014). The NLDN CG flash detection efficiency is ~95%, and approximately 50% of IC flashes are detected, although network improvements are increasing this value (Nag et al., 2011; Holle et al., 2014). The data provides information regarding the time and location of the flash, as well as its polarity, strength, the number of return strokes (multiplicity), 50% location error ellipse, and several other parameters.

The Earth Networks Total Lightning Network (ENTLN) also uses a time-of-arrival method; its sensors use a broad frequency range (1 Hz to 12 MHz) to detect both CG and IC strokes (Liu et al., 2015). The network has over 1,200 sensors deployed globally (Earth Networks, 2017), with the best coverage over the United States. The CG and IC detection efficiency is generally greater than 90% and 50% across the United States, respectively. The CG detection efficiency exceeds 95% east of the High Plains, and the IC detection efficiency increases up to 65% in the West and 95% over portions of the Midwest and East Coast (Liu and Heckman, 2011; Saunders, 2012; Liu et al., 2015). Flashes are generated by grouping strokes that are within 700 ms and 10 km of each other. If the cluster contains a return stroke, it is considered to be a CG flash. The observed data also provide information about polarity and peak current (Liu et al., 2015).

If the detection efficiency for IC flashes is too uncertain, a rough estimate of the

number of total lightning flashes observed by a network may be calculated by:

$$total\ flashes = CG\ flashes \times \left[\frac{1}{DE}\right] \times [IC{:}CG\ ratio + 1], \quad (1)$$

where *DE* is a network's CG detection efficiency and the *IC:CG ratio* is the ratio of

intracloud to cloud-to-ground flashes, which may be based on the gridded climatological

mean IC:CG ratios over the United States (Boccippio et al., 2001). However, IC:CG

ratios vary considerably from storm to storm and during a particular storm.

In the mid-1970s a 3D total lightning location mapping system, called the

Lightning Detection and Ranging (LDAR) system, was developed at NASA Kennedy

Space Center (KSC) and installed in and around KSC and Cape Canaveral Air Force

Station (CCAFS; Starr et al., 1998). The LDAR system was used as a model by lightning

researchers at New Mexico Tech as they began designing a new generation of permanent

and mobile lightning mapping arrays (LMAs) in the mid-1990s. Currently, LMAs are

located in 11 regions across North America: central New Mexico, northeast Colorado,

west Texas, Oklahoma, Houston, northern Alabama, northern Georgia, Kennedy Space

Center (KSC), Washington D.C., Wallops Island, and Toronto, Canada (Padula and

Goodman, 2016). Each network includes multiple stations, which use time-of-arrival

sensors to detect the very high frequency (VHF) electromagnetic pulses emitted by a

lightning flash. The result is a 3D map of total lightning activity, although the sensors

mainly detect IC flashes and the upper segments of CG flashes (Stano et al., 2010). After

data processing, the LMA data can provide information about the VHF source density,

flash extent density, flash initiation density, average flash area, and the vertical distribution of flash channel lengths.

In a continuing effort to improve lightning observations and extend the length of historical records, the first Geostationary Lightning Mapper (GLM) was launched in November 2016 onboard the Geostationary Operational Environmental Satellite R-Series (GOES-R; renamed GOES-16 by NOAA). With the addition of future satellites from the GOES-R series, continuous monitoring of CG, IC, and cloud-to-cloud lightning flashes will be provided over the Western Hemisphere from New Zealand to the west coast of Africa at a spatial resolution of roughly 8 km (Chronis et al., 2008; Goodman et al., 2013; Buechler et al., 2014). The increased coverage over land and ocean locations will allow for the quantity, intensity, and variation of lightning activity to be examined with greater detail, especially areas where lightning monitoring is sparse. In addition, a duplicate of the LIS instrument was installed on the International Space Station (ISS) in late February 2017. The ISS LIS provides coverage to much higher latitudes (±54° latitude; Blakeslee et al., 2014) than TRMM LIS (±38° latitude), along with the ability to sample 98% of the lightning that occurs annually across the globe. The ISS LIS observes lightning at a given location only during an overpass and with the same field of view as TRMM LIS (600 km × 600 km). However, the data collected by ISS LIS will be used to help improve the global lightning climatology and LNO_x estimates, in addition to many other scientific applications (Blakeslee and Koshak, 2016).

2.3 Flash rate parameterization schemes

Cloud-resolved models may incorporate explicit electrical schemes to study lightning activity in thunderstorms (e.g., Helsdon et al., 1992; Mansell et al., 2002; Barthe et al.,

2005; Fierro et al., 2013). The difficulties with using explicit schemes for simulating lightning flashes include the complexity of the electrical activity and the computational cost of modeling the intricate behavior (McCaul et al., 2009). To avoid these difficulties, FRPSs based on storm parameters output by models is a useful way to replicate a thunderstorm's electrification. However, the schemes are only as good as the model's ability to predict the location and strength of the convection and the distribution of hydrometeors (Fierro et al., 2013). If the kinematic and microphysical characteristics are inaccurate, the non-inductive charging, which is believed to be the main mechanism for cloud electrification (Takahashi, 1978; Jayaratne et al., 1983; Saunders et al., 1991; Latham et al., 2007; Barthe et al., 2010; Rakov, 2016), will not be properly represented by the proxy parameters (e.g., updraft volume and graupel echo volume). This charging mechanism usually occurs where a strong updraft coincides with the mixed-phase region of the cloud (Zipser and Lutz, 1994; Deierling and Petersen, 2008; Deierling et al., 2008). Here graupel and ice crystals collide and rebound in the presence of supercooled liquid water and are transported by updrafts and gravity to achieve charge separation and eventually lightning initiation (Takahashi, 1978; Saunders et al., 1991; MacGorman and Rust, 1998; Deierling and Petersen, 2008; Basarab et al., 2015). Described below are eighteen FRPSs for predicting total lightning. The schemes are evaluated in our study at a cloud-resolving scale and include those developed prior to and after the DC3 field experiment. The earliest FRPSs were based on kinematic and structural characteristics of thunderstorms, while more recent schemes evolved toward the use of microphysical variables. Table 1 lists each FRPS equation and Table 2 highlights the type of criteria threshold required by each scheme.

Table 1. Flash rate parameterization schemes tested in WRF cloud-resolved simulation of 29-30 May 2012 Oklahoma case study, where f is total flash rate in flashes min^{-1}, FD is flash density in flashes km^{-2} day^{-1}, FD_l is flash density over land in flashes $m_{grid\ cell}^{-2}$ s^{-1}, and FD_{LTG3} is flash density in flashes km^{-2} 5-min^{-1}.

Flash Rate Parameterization Scheme	Flash Rate Equation (reference) [+]
Maximum vertical velocity (w_{max})	$f = 5\times10^{-6} \times (w_{max})^{4.5}$ (Price & Rind, 1992)
Cloud top height (CTH)	$f = 3.44\times10^{-5} \times H^{4.9}$ (Price & Rind, 1992)
Updraft volume (UV)	$f = 6.75\times10^{-11} \times w_5 - 13.9$ (Deierling & Petersen, 2008)
Ice water path (IWP)	$FD = 33.33 \times IWP - 0.17$ (Petersen et al., 2005)
Precipitation ice mass (PIM)	$f = 3.4\times10^{-8} \times p_m - 18.1$ (Deierling et al., 2008)
Ice mass flux product (IMFP)	$f = 9.0\times10^{-15} \times (f_p \times f_{np}) + 13.4$ (Deierling, 2006; Deierling et al., 2008)
CSU graupel echo volume (CSU GEV)	$f = 7.0\times10^{-2} \times GEV$ (Basarab et al., 2015)
CSU 35dBZ echo volume (CSU 35EV)	$f = 7.2\times10^{-2} \times 35EV$ (Basarab et al., 2015)
CSU precipitation ice mass (CSU PIM)	$f = 1.2\times10^{-7} \times PIM$ (Basarab et al., 2015)
UAH graupel echo volume (UAH GEV10)	See Carey et al. (2015)
UAH graupel echo volume (UAH GEV5)	See Carey et al. (2015)
UAH updraft volume (UAH UV)	See Carey et al. (2015)
UAH graupel echo volume for supercells (UAH GEV10S)	See Carey et al. (2015)
UAH graupel echo volume for supercells (UAH GEV5S)	See Carey et al. (2015)
UAH updraft volume for supercells (UAH UVS)	See Carey et al. (2015)
Upward cloud ice flux (ICEFLUX)	$FD_l = 6.58\times10^{-7} \times \varphi_{ice}$ (Finney et al., 2014)
OK 35dBZ echo volume (OK 35EV)	$f = 0.0111 \times 35EV + 1.6619$ (CSU/T. Davis)
Blended lightning threat (LTG3)	$FD_{LTG3} = (0.95\times graupel\ flux) + (0.05\times VII)$ (McCaul et al., 2009)

[+] Units for each storm parameter are: w_{max} in (m s^{-1}); CTH in (km); UV in (m^3); IWP in (kg m^{-2}); PIM and CSU PIM in (kg); IMFP in (kg^2 m s^{-2}); every GEV and 35EV are in (km^3); UAH UV and UVS in (km^3); ICEFLUX in (kg_{ice} m_{cloud}^{-2} s^{-1}); graupel flux in (m s^{-1} g kg^{-1}) and VII in (kg kg^{-1})

Table 2. Required criteria thresholds for each flash rate parameterization scheme.

Flash Rate Parameterization Scheme	Required Criteria Thresholds			
	Reflectivity (dBZ)	Temperature (°C)	Vertical Velocity (m s^{-1})	Hydrometeor (g kg^{-1})
w$_{max}$			maximum	
CTH $^{+}$	> 20	< 0		
UV		< -5	> 5	
IWP	> 25	< -10		
PIM *		< -5	w < vts	snow > 0.25 graupel > 0.5
IMFP *		< -5	Non-precip: w > vts Precip: w < vts	ice > 0 snow > 0.25 graupel > 0.5
CSU GEV	> 35	-40 < T < -5		graupel > 0.5
CSU 35EV	> 35	-40 < T < -5		
CSU PIM	> 35	-40 < T < -5		
UAH GEV10		-40 < T < -10		graupel > 0.5
UAH GEV5		-40 < T < -5		graupel > 0.5
UAH UV		-40 < T < -10	> 5	
UAH GEV10S		-40 < T < -10		graupel > 0.5
UAH GEV5S		-40 < T < -5		graupel > 0.5
UAH UVS		-40 < T < -10	> 5	
ICEFLUX *			w < vts	ice > 0 snow > 0.25
OK 35EV	> 35	-40 < T < -5		
LTG3		T = -15		graupel > 0.5

$^{+}$ indicates the highest altitude where both criteria are met.

* indicates the storm vertical velocity (w) and snow fall speed (vts) are both required.

2.3.1 Cloud top height and maximum vertical velocity

Early research investigated correlations between lightning flash rate and either cloud top height (CTH) or maximum vertical velocity (w$_{max}$). Williams (1985) indicated a non-linear relationship existed between total lightning and CTH, as well as CTH and w$_{max}$, based on thunderstorms observed in New England, Florida, and New Mexico (i.e., continental, midlatitude convection). Using these same data, Price and Rind (1992) further developed the relationships with the intent that they could be used at a coarse

resolution to predict global lightning patterns. For use in cloud-resolved models, such as WRF, the CTH (km) is represented by the maximum height of the 20 dBZ radar reflectivity where the temperature is below freezing (0 °C). Since updraft velocities play an important role in cloud electrification, Price and Rind (1992) used additional field measurements to investigate the differences in the relationships between w_{max} and CTH for thunderstorms over land and water. The results show there is a positive correlation between the two storm parameters and that when CTHs are similar, the w_{max} tends to be stronger for continental versus marine convection. This supported conclusions previously made by researchers regarding why lightning activity may vary given certain convective cloud characteristics. By combining the two equations, which link lightning flash rate (flashes min^{-1}) with CTH and CTH with w_{max}, a non-linear relationship between lightning activity and w_{max} (m s^{-1}) was defined. The horizontal resolution that is suggested as most appropriate for applying either FRPS is an area that is as wide as the storm is tall (Williams, 1985; Pickering et al., 1998).

2.3.2 Updraft volume

The updraft volume (UV) scheme (Deierling and Petersen, 2008) was developed on a storm scale using ground-based dual-polarimetric and dual-Doppler radar data and total lightning data from 11 convective events, which include single cell, multicell, and supercell thunderstorms. The events were observed in northern Alabama in 2005 and in Kansas and Colorado during the Stratospheric-Tropospheric Experiment: Radiation, Aerosols and Ozone (STERAO-A) and Severe Thunderstorm Electrification and Precipitation Study (STEPS) field campaigns. Total lightning data were provided by the Northern Alabama LMA and by the Office Nationale d'Etudes et de Recherches

Aerospatiales (ONERA) lightning interferometer (in STERAO-A and STEPS). Deierling and Petersen (2008) indicate there is a strong correlation ($r = +0.93$) with total lightning when UV is computed within the mixed-phase region (i.e., temperature < -5 °C) where vertical velocities > 5 m s^{-1}. It is also suggested that this combination of criteria required for developing the scheme creates a robust relationship that is at least applicable in the two different regional environments in which the above thunderstorm events were observed. Negative flash rates are generated when UV $< 2.06 \times 10^{11}$ m^3 because the linear relationship between UV and total lightning activity (flashes min^{-1}) has a non-zero y-intercept.

2.3.3 Ice mass flux product and precipitation ice mass

Ice mass flux product (IMFP) and precipitation ice mass (PIM) (Deierling, 2006; Deierling et al., 2008) are examples of flash rate-storm parameter relationships involving ice-phase hydrometeors. The IMFP and PIM schemes were both developed using the same thunderstorm cases and observed data as the UV scheme (Deierling and Petersen, 2008). The storm parameters were calculated at temperatures < -5 °C, where PIM (kg) is a summation of only the graupel mass and IMFP (kg^2 m s^{-2}) involves the vertical motion of both the precipitation and nonprecipitation (suspended) ice masses through each grid point.

Hydrometeor types were derived from polarimetric radar data using fuzzy logic algorithms (Vivekanandan et al., 1999). The hydrometeor categories used by Deierling et al. (2008) to define precipitation ice included hail, hail/rain mixture, graupel/small hail/rain mix, and graupel/small hail. Nonprecipitation ice was classified as dry snow and ice crystals that were either irregular or horizontally oriented. Using the dominant

hydrometeor identified at each radar grid point, Deierling et al. (2008) used the reflectivity (Z) – mass content (M) relationships to calculate the ice mass (Heymsfield and Palmer, 1986; Heymsfield and Miller, 1988).   The precipitation ice mass flux calculated by Deierling et al. (2008) used the precipitation ice terminal fall speed, while Barthe et al. (2010) indicated this could be replaced by the difference between vertical wind velocity and precipitation ice fall speed. Barthe et al. (2010) also suggested nonprecipitation ice mass flux may be determined using the difference between vertical wind velocity and nonprecipitation ice fall speed instead of horizontal divergence.

Both FRPSs indicate a linear relationship exists on a storm scale between the independent (IMFP or PIM) and dependent (total lightning activity) variables (Deierling et al., 2008). However, the y-intercepts are non-zero. This means lightning is produced (flashes min^{-1}) when IMFP is zero and negative flash rates occur when PIM $< 5.32 \times 10^8$ kg.

For our WRF simulation, precipitation ice includes graupel/hail and snow, while nonprecipitation ice includes snow and cloud ice. Precipitation (nonprecipitation) snow is considered to occur at model grid points where the snow terminal fall speed determined by the microphysics scheme is greater (less) than the updraft velocity. Nonprecipitation ice is identified at model grid points where cloud ice exists and the vertical velocity > 0 m s^{-1}. Model-simulated graupel/hail at any grid point is assumed to be precipitation.

2.3.4 Ice water path

The ice water path (IWP) scheme is another example of a FRPS based on hydrometeors and was developed using data from the LIS and Precipitation Radar instruments onboard the TRMM satellite during the 1998-2000 warm seasons (Petersen et al., 2005). Data

points used in developing this relationship represent IWP (kg m^{-2}) and flash density

(flashes km^{-2} day^{-1}) over 0.5° × 0.5° (~50 km × 50 km) grid cells between ±35° latitude.

In our cloud-resolved WRF simulation IWP was calculated by integrating the

precipitation and nonprecipitation ice mass at all points within a column where radar

reflectivity > 18 dBZ and temperature < -10 °C (Petersen et al., 2005; Barthe et al.,

2010). However, the column area is scaled down to the smaller WRF processor area

(~18 km × 19 km) and the lightning flash density within the processor is converted to

flash rate (flashes min^{-1}). While this scheme is linear, the y-intercept is negative.

Therefore, a negative flash rate is generated when the IWP < 5.10×10^{-3} kg m^{-2}. The

model-simulated hydrometeors included in the IWP storm parameter calculation are

cloud ice, snow, and graupel/hail. Barthe et al. (2010) found that this FRPS scheme is

sensitive to the radar reflectivity threshold used to evaluate the IWP. In their cloud-

resolved simulation they adjusted for the overprediction in anvil reflectivity by increasing

the reflectivity limit, so IWP is integrated over a smaller region. This caused IWP to

increase for their simulated storm.

2.3.5 Upward cloud ice flux

Developed from data over a similar area (±38° latitude) as the IWP scheme, the upward

cloud ice flux (ICEFLUX; kg$_{ice}$ m$_{cloud}^{-2}$ s^{-1}) scheme defines a linear relationship using

suspended ice data from the ERA-Interim global atmospheric reanalysis provided by the

European Centre for Medium-Range Weather Forecasting (ECMWF) and lightning flash

density data observed by LIS on 2.5° × 2.5° (~270 km × 250 km) grid cells (Finney et al.,

2014). In our model the calculated flash density (flashes m$_{grid\ cell}^{-2}$ s^{-1}) was converted to

flash rate (flashes min^{-1}) by accounting for the model domain's horizontal resolution.

Our analysis represents the first time this scheme is tested at cloud-resolved resolution.

Finney et al. (2014) suggest ICEFLUX be evaluated at 440 hPa, since it is the cloud top

pressure criterion for deep convective clouds specified by the International Satellite

Cloud Climatology Project (ISCCP) (Rossow et al., 1996). Finney et al. (2014) also

assessed this scheme at 440±100 hPa to test its sensitivity to pressure. They found lower

correlations at higher pressures and similar correlations at lower pressures, confirming

that 440 hPa was a good choice.

2.3.6 McCaul lightning threat methods

Lightning threat methods developed by McCaul et al. (2009, 2011) forecast flash rate

density (flashes km^{-2} 5-min^{-1}) using either graupel flux at -15 °C or the gridded vertically

integrated ice (VII). The graupel flux is a product of the upward vertical velocity (m s^{-1})

and graupel mixing ratio (g kg^{-1}), while the VII focuses on the graupel, snow, and cloud

ice mixing ratios (kg kg^{-1}) within the grid column. Seven convective events observed

over northern Alabama were analyzed with WRF at cloud-resolved scales. Over the

lifetime of each event, the maximum LMA flash origin density per 5-min and maximum

model-simulated storm parameter were identified within the domain and used to create

linear relationships between lightning and ice hydrometeors. The slope of each line was

then used to calibrate their respective equation. The graupel flux and VII methods

capture the temporal variability and areal coverage of lightning activity, respectively,

with a weighted summation of the two methods (0.95 graupel flux and 0.05 VII)

providing the best prediction of flash rate density (McCaul et al., 2009). The weighted

summation is referred to as the blended lightning threat (LTG3). Initially, the resulting

flash rate densities determined by graupel flux and VII were only used when they

exceeded a threshold of 0.01 and 0.40 flashes km^{-2} 5-min^{-1}, respectively. However, additional techniques were developed to acknowledge specific concerns. These include (1) increasing the graupel flux method threshold (1.5 flashes km^{-2} 5-min^{-1}) to address winter stratiform weather, (2) forcing VII to have the same peak flash rate density as graupel flux to avoid deviation of individual lightning threat methods during high flash rate events, and (3) assigning a flash rate density threshold to the blended method for a more accurate depiction of areal coverage (McCaul et al., 2011; Eugene McCaul, personal communication, January 13, 2017). Our case study will only focus on the LTG3 method and will also represent the first time it is evaluated using the Morrison two-moment microphysics and Yonsei University (YSU) planetary boundary layer (PBL) schemes.

2.3.7 Newly-developed FRPSs from DC3

Observations from the DC3 field campaign were included in the creation of new total lightning-storm parameter relationships. Total lightning flash data collected by LMA and radar data within the northeast Colorado and northern Alabama DC3 study regions allowed for the development of additional FRPSs by Colorado State University (CSU) and the University of Alabama in Huntsville (UAH), respectively (Basarab et al., 2015; Carey et al., 2015). Data used in FRPS development for these regions were from the DC3 period as well as other years. Our study will evaluate the performance of these newly-developed schemes for the first time in a model at cloud-resolved resolution.

2.3.7.1 Colorado FRPSs

Nine of the 11 isolated storms (i.e., single cell and supercell with varying severity) used by Basarab et al. (2015) in developing new FRPSs were from DC3, while the other two

events were from summer 2013. All events were objectively identified using a cell-tracking algorithm (Fuchs et al., 2015). The average and maximum total flash rates associated with the observed convection dataset are 53.9 flashes min^{-1} and 287.8 flashes min^{-1}, respectively. In addition to LMA data, the polarimetric radar data were gridded at 0.5 km^3 resolution and fuzzy logic algorithms (Dolan et al., 2013) were applied to the radar data to identify the dominant hydrometeor type per grid. Basarab et al. (2015) used the Colorado convective events dataset to modify previously developed FRPSs from the literature (e.g., PIM; kg). These schemes were not properly tuned to capture the higher flash rate Colorado storms and were also developed using a different hydrometeor identification algorithm.

In addition, graupel echo volume (CSU GEV; km^3) and 35 dBZ echo volume (CSU 35EV; km^3), which are similar to PIM and have previously shown strong correlations to lightning (Carey and Rutledge, 1996; Wiens et al., 2005; Liu et al., 2012), were also used to develop FRPSs for Colorado storms. To calculate the storm parameters, data points were restricted to the mixed-phase region of convective clouds (i.e., -5 °C > temperature > -40 °C and reflectivity > 35 dBZ). The linear relationships between total lightning and the CSU PIM, GEV, and 35EV resulted in a better fit to the data than the prior existing schemes in the literature. The CSU 35EV was the most successful storm parameter for estimating total lightning flash rates in Colorado. Basarab et al. (2015) also suggest this scheme may be robust enough to be used in different environments and regions based on its exceptional performance when used to examine thousands of isolated convective events from four areas (i.e., Colorado, Oklahoma, northern Alabama, and Washington, D.C.). This scheme performed best when the

environment had low normalized convective available potential energy (NCAPE

< 0.1 m s^{-2}), moderate warm cloud depth (1-2 km), and moderate vertical wind shear

(10-20 m s^{-1}).

2.3.7.2 Northern Alabama FRPSs

Carey et al. (2015) developed FRPSs using 32 convective cells observed over northern

Alabama, which ranged in storm type and severity (i.e., multicell, supercell and one

quasi-linear convective system). Five of the events occurred during DC3. Unlike the

CSU approach, which used a cell-tracking algorithm to identify and track isolated

convective cells (Fuchs et al., 2015), UAH (Carey et al., 2015) used both objective and

subjective approaches for tracking. The manual approach was necessary for the multicell

events observed during DC3 to avoid any influence from nearby storms. Based on the

LMA data, this dataset had an average total flash rate of 12.5 flashes min^{-1} and a

maximum of 102 flashes min^{-1}. Polarimetric and Doppler radar data were also available

and fuzzy logic algorithms were utilized to determine the dominant hydrometeor types

(Vivekanandan et al., 1999). Both datasets were gridded at 1 km resolution in the

horizontal and vertical. Of the 17 storm parameters Carey et al. (2015) tested for the

northern Alabama region, the linear relationships between total lightning (flashes min^{-1})

and graupel echo volume between -10 °C > temperature > -40 °C (UAH GEV10; km^3),

graupel echo volume between -5 °C > temperature > -40 °C (UAH GEV5; km^3), and

updraft volume between -10 °C > temperature > -40 °C and vertical velocities > 5 m s^{-1}

(UAH UV; km^3) appeared to work best based on the normalized median and mean bias

errors. Based on these storm parameters, three additional FRPSs were developed for

supercell events (UAH GEV10S, GEV5S, and UVS).

2.3.7.3 Tailored FRPS for 29-30 May 2012 convective event

Since the objective of our study was to evaluate FRPSs in a simulation of an Oklahoma thunderstorm observed during DC3, it was desirable to include a scheme based on data from this region. According to Basarab et al. (2015), the 35EV was the most robust storm parameter used in their analysis for estimating lightning flash rates based on how well it performed when tested using thousands of isolated storms in multiple regions of the continental United States. Therefore, CSU developed a version of this scheme using data from the Weather Surveillance Radar-1988 Doppler (WSR-88D) at Oklahoma City (KTLX) and the central Oklahoma LMA during the 29-30 May 2012 event. The observed 35EV (km^3) and total lightning flash rates (flashes min^{-1}) resulted in a linear relationship based on convection located north of Oklahoma City (35.49 °N) in the Oklahoma domain. This Oklahoma 35EV (OK 35EV) scheme applied the same mixed-phase region temperature criteria as the CSU 35EV scheme (-5 °C > temperature > -40 °C). A similar relationship was found in two cells within a mesoscale convective system (MCS) observed in Oklahoma during the Thunderstorm Electrification and Lightning Experiment (TELEX) in 2004, where lightning initiation typically occurred within the 35 dBZ reflectivity contour in the presence of graupel (Lund et al., 2009).

2.4 Previous FRPS evaluation with cloud-resolved models

Barthe et al. (2010) simulated an isolated severe storm observed during STERAO-A and an airmass thunderstorm over northern Alabama using WRF. An evaluation of six FRPSs using model output suggests the flash rates and trends are best represented by w_{max} and CTH for the severe and airmass storms, respectively. Their research differs from previous work because it was the first time flash rate-storm parameter relationships

developed from field experiment observations were tested in a cloud-resolved model. Cummings et al. (2013) used the WRF Aqueous Chemistry (WRF-AqChem; Barth et al., 2007) model to run a cloud-resolved simulation of a deep convective storm that occurred during the Stratospheric-Climate Links with Emphasis on the Upper Troposphere and Lower Stratosphere (SCOUT-O3)/Aerosol and Chemical Transport in Tropical Convection (ACTIVE) field campaigns near Darwin, Australia. The performance of FRPSs in tropical island convection was assessed for the first time by Cummings et al. (2013) and initial results suggested w_{max} and CTH were good predictors of the observed flash trend at the cloud-resolved scale. Since models do not perfectly replicate the features of an observed storm, a better representation of the observed flashes is produced using the regression between the observed and model-simulated storm parameters to adjust the FRPSs (Barthe et al., 2010) or by scaling the model-simulated flash rates. In my case study reported here, I scale the over or underprediction of specific aspects of a storm parameter (e.g., graupel, snow) within a FRPS.

CHAPTER 3: INFLUENCE OF DEEP CONVECTION ON ATMOSPHERIC CHEMISTRY

A thunderstorm may affect the chemical composition of the environment in several ways. Precipitation cleanses the atmosphere by washing out soluble pollutants, such as nitric acid (HNO_3), and depositing them on the ground. Updrafts lift polluted air from the surface to higher altitudes, where it can disperse within the upper troposphere. However, downdrafts transport cleaner air from the free troposphere or lower stratosphere to the boundary layer. Production and destruction of trace gases, such as NO_x and O_3, occurs during an active thunderstorm or downwind following the convective event. Lightning produces NO_x, which in large enough quantities may lead to O_3 loss within a storm cloud. As the NO_x is diluted in the upper tropospheric storm outflow, it leads to efficient photochemical O_3 production downwind of a storm.

3.1 Lightning-generated nitrogen oxides

A lightning flash is brief, but hot (~30,000 K). The high temperature partly dissociates molecular oxygen (O_2) and nitrogen (N_2) in and near the flash, which allows oxygen and nitrogen atoms to react and produce NO. The lightning channel quickly cools as it mixes with colder, ambient air over the course of a few seconds. During the cooling process the lightning-heated air reaches a "freeze-in" temperature, roughly 3,000 K (Hill et al, 1980; Schumann and Huntrieser, 2007), where the reactions which would normally create and destroy NO are no longer in chemical equilibrium. This leads to a large fraction of the initially generated NO to be saved (Chameides et al., 1977; Hill et al, 1980; Huntrieser et al., 1998; Rakov and Uman, 2003).

The lifetime of NO_x varies as a function of altitude, with lifetimes on the order of a day or less near the earth's surface to lifetimes as long as several days to a week in the upper troposphere (Ridley et al., 1996; Jaeglé et al., 1998; Huntrieser et al., 1998; Martin et al., 2007). The variation is mainly due to two mechanisms involving the production of HNO_3. The reaction between NO_2 and OH is temperature dependent, so the reaction rate slows as the temperature decreases in altitude between the surface and the tropopause. Nitrogen dioxide is also involved in the production of N_2O_5. However, the heterogeneous production of HNO_3 slows because the reaction between N_2O_5 and water occurs on aerosols, which there are fewer of in the upper troposphere. There is also a greater tendency for NO_x to exist as NO (Jaeglé et al., 1998) in the upper troposphere due to other temperature dependent reactions that slow with altitude, such as those between NO and O_3 and between NO and HO_2.

Unfortunately, direct measurements of LNO_x production are not possible, although cloud-resolving models and observations from satellites and aircraft have helped to slightly reduce the uncertainty. The best approximation for the contribution of lightning to the global NO_x budget is 5 ± 3 Tg (N) yr^{-1} (Schumann and Huntrieser, 2007). The main areas of uncertainty include the production of NO per IC and CG flashes, the amount of NO produced per unit flash length, and the vertical profile of LNO_x mass (Ott et al., 2010). The 5 Tg (N) yr^{-1} translates to approximately 250 moles NO_x $flash^{-1}$ or 3.5 kg (N) $flash^{-1}$. The conversion was completed in the literature survey (Schumann and Huntrieser, 2007) using the mass of nitrogen (14 g (N) $mole^{-1}$) and the assumption that every second roughly 44 flashes occur across the globe (Christian et al., 2003).

Analyses investigating types and lengths of lightning flashes indicate the amount of NO produced per meter flash channel length is less in IC versus CG flashes and that longer flash lengths produce more LNO_x (Barthe and Barth, 2008). However, other cloud-resolved modeling constrained by aircraft observations (DeCaria et al., 2000, 2005) suggests that on average IC and CG flashes make similar amounts of NO per flash. For a "typical" thunderstorm the accepted LNO_x production range is 33-660 moles NO flash^{-1}, with an average production rate of 250 moles NO flash^{-1} (Schumann and Huntrieser, 2007). Previous model analyses of midlatitude thunderstorms suggest 200-500 moles NO flash^{-1} is a reasonable estimate (DeCaria et al., 2000, 2005; Fehr et al., 2004; Ott et al., 2007) of the mean production rate. Simulations of five convective events taken from the midlatitudes and subtropics yielded a mean value of 500 moles NO flash^{-1} (Ott et al., 2010). A simulation of a "Hector" thunderstorm over the Tiwi Islands of northwestern Australia indicated a NO production scenario of 500 moles flash^{-1} was also appropriate for this tropical island convection; however, 600 moles NO flash^{-1} was not an unreasonable upper limit (Cummings et al., 2013). Although the LNO_x production from each of these analyses falls within the range of a "typical" thunderstorm, the variation indicates uncertainty still exists. In addition, Ott et al. (2010) suggest the amount of LNO_x per unit flash length ranges from 1.7 to 22×10^{-3} moles NO m^{-1} due to the influence of peak current and ambient pressure. Ideally, researchers would like to decrease the uncertainty range of the global LNO_x budget to ±1 Tg (N) yr^{-1} or 20%, but understand the difficulty in doing so (Schumann and Huntrieser, 2007).

3.2 LNO$_x$ parameterization schemes

When simulating the generation, distribution, and transport of LNO$_x$ within a convective

cloud, several conditions must be defined. These include the number of total flashes, the

fractional flash channel vertical distribution, and the number of moles NO per flash.

Depending on the type of convective parameterization that is chosen, these selections

may need to be partitioned into CG and IC lightning flashes. The dependence of LNO$_x$

production on pressure must also be accounted for when calculating the vertical profile of

the NO$_x$ contribution from the fractional lightning channel (DeCaria et al., 2005) and

LNO$_x$ mass (Ott et al., 2010) distributions. Several approaches for incorporating LNO$_x$ in

the horizontal within the cloud also exist. The options for vertical and horizontal LNO$_x$

distributions are described below.

3.2.1 Vertical distribution of lightning flash channel lengths and NO$_x$

A LNO$_x$ vertical distribution may be specified for either cloud-resolved or parameterized

convection. The default distributions offered in WRF follow DeCaria et al. (2005) and

Ott et al. (2010). However, observed lightning flash channel data can replace these

vertical profiles in case study simulations, as discussed in Section 3.2.1.3.

3.2.1.1 Cloud-resolved convection

When the vertical distributions of lightning flash channel lengths were first developed,

observations from lightning mapping systems indicated that thunderstorm flash channels

generally peaked at one or two layers (MacGorman and Rust, 1998). Based on these

early data, DeCaria et al. (2000) suggested the vertical profiles for CG and IC lightning

were best represented as unimodal and bimodal Gaussian distributions, respectively.

Therefore, the lightning channels in cloud-resolved convection are set to maximize at

specified lower (CG and IC flashes) and upper (IC flashes) temperature levels, which correspond to a thunderstorm's two main charge regions (Ott et al., 2010). For midlatitude storms, the channels are set to -15 °C and -45 °C, which is roughly 6 km and 10.5 km, respectively. The main negative charge region is typically located at -15 °C in the lower portion of the convective cloud (DeCaria et al., 2005). The upper temperature limit may be modified higher or lower based on cloud top height (Pickering et al., 2009; Ott et al., 2010). For instance, the upper mode isotherm was adjusted to a colder temperature (-60 °C or ~12.7 km) for a cloud-resolved simulation of a "Hector" thunderstorm (Cummings et al., 2013), which is typically very tall. Not only is the tropopause higher in the tropics, but the mean IC flash altitude was also higher than the assumption for midlatitude thunderstorms during the period when the simulated storm was observed. Adjustments in the upper temperature level may also be necessary to achieve better agreement between the altitude of aircraft-observed and model-simulated NO_x mixing ratios (Ott et al., 2010).

3.2.1.2 Parameterized convection

At regional and global scales, LNO_x production can be parameterized through the use of output from cloud-resolved simulations of observed convective events (DeCaria et al., 2000). Pickering et al. (1998) and Ott et al. (2010) simulated various types of thunderstorms (e.g., isolated and MCS) from across the globe (i.e., the central United States, south Florida, Germany, western Pacific, the region between Australia and New Guinea, the Atlantic off West Africa, and Brazil) using 2D and 3D cloud-scale chemical transport models. The resulting vertical profiles represent a combination of the CG and IC LNO_x mass influenced by both production and convective transport. Pickering et al.

(1998) suggested the average LNO_x vertical distributions were C-shaped with peaks in the upper troposphere and in the boundary layer, while Ott et al. (2010) showed the profiles resembled a backward C-shape with a single peak in the middle to upper troposphere. The updated vertical distributions are considered more realistic because a 3D model is used to distribute LNO_x based on the VHF sources generated by observed CG and IC flashes, instead of using a 2D model to distribute the CG and IC LNO_x between the -15 °C isotherm and the surface and cloud top, respectively. Therefore the single-mode Gaussian distributions defined by Ott et al. (2010) for midlatitude continental, subtropical, and tropical continental and marine environments are typically used for parameterized convection in larger scale models, such as GEOS-Chem, the NASA Global Modeling Initiative (GMI; Allen et al., 2010), and the GEOS-5 Chemistry and Climate Model (GEOS-CCM, Liaskos et al., 2015).

3.2.1.3 Observations

Observed vertical distributions of flash channel lengths may be constructed for specific convective events and used to replace the default Gaussian distributions for CG and IC lightning in thunderstorms at cloud-resolved scales (DeCaria et al., 2000). Within the coverage of a LMA network, a CG flash dataset (e.g., NLDN) is used to help identify and partition the LMA total lightning into CG and IC flashes. A method, such as the 3D convex hull volume (Bruning and Thomas, 2015), can then be used to derive the fraction of lightning channel lengths in the vertical. A vertical distribution may not be the same throughout a thunderstorm's life cycle and it may also vary by region and between storms (DeCaria et al., 2000). With the installation of LMA networks across the United States, a

climatology of flash channel length vertical profiles could be used to update the default distributions or possibly provide location dependent options.

Another approach to calculating LNO_x production is with the Lightning Nitrogen Oxides Model (LNOM) by Koshak et al. (2014). This model does not take into consideration any mixing of the LNO_x within the atmosphere. It only provides vertical profiles of 10-meter flash channel segments (channel length) and LNO_x production. The flash channel segment data come from LMA observations and the LNO_x production per meter of channel length come from laboratory data and theoretical assumptions. Unlike the most recent research, which suggests average LNO_x production for IC and CG flashes may be equal, Koshak (2014) indicates that on average a CG flash (604.3 moles) in northern Alabama may produce 16.6 times more LNO_x than an IC flash (36.4 moles).

3.2.2 Horizontal distribution of LNO_x

Once a vertical distribution of the fraction of total LNO_x in each layer is selected, the LNO_x can be placed uniformly within each horizontal layer of the convective cloud given specified thresholds of reflectivity or hydrometeor mass mixing ratios. To determine the amount of NO that is incorporated into the horizontal area of the convection, the number of lightning flashes within the column, the frequency of lightning flash channel lengths, and the NO production scenario are each considered. Early studies limited the CG LNO_x to radar reflectivities > 20 dBZ between the surface and -15 °C isotherm, while IC LNO_x was restricted to every layer within the cloud boundary from the -15 °C isotherm to cloud top (Pickering et al., 1998; DeCaria et al., 2000). In the 3D models used by DeCaria et al. (2005) and Ott et al. (2010), all the LNO_x was injected within the 20 dBZ contour. This method represents a situation where the LNO_x is immediately dispersed within the

identified portion of the cloud. More recently, Mecikalski and Carey (2017) and Fuchs and Rutledge (2017, in press) have investigated the partitioning of lightning source and flash data by altitude and radar reflectivity for convective events observed in different regions of the United States. Both studies provide insight into how the radar reflectivity threshold for the horizontal placement of LNO_x in this bulk approach may be modified for specific regions, storm types, and flash types.

A filament approach was also investigated, which tries to replicate the branching of a lightning flash within a predetermined area downwind of the maximum updraft (Ott et al., 2007; Barthe and Barth, 2008; Ott et al., 2010). This area represents the average horizontal flash extent and within each layer above this region the LNO_x is randomly distributed among a specific number of points that are defined by the magnitude of the vertical distribution in that layer. This approach attempts to provide a more realistic representation of the LNO_x production and transport by focusing on a smaller area of the cloud where a flash occurs. However, Ott et al. (2010) found this method resulted in a similar NO production per flash as simulations using the bulk approach and indicated that different analysis techniques and model set ups may have a greater influence on estimates of NO production.

3.3 Effects on other trace gases

Compared with the boundary layer, the lifetime of NO_x is about 5-10 times longer in the upper troposphere, where the dominance of lightning as a global NO_x source plays a key role in the production of O_3. Because of its ability to absorb and emit longwave terrestrial radiation, O_3 is considered a significant greenhouse gas (Lacis et al., 1990). For O_3 production in the upper troposphere, time is required for photochemical reactions

to occur in the outflow following a convective event (Pickering et al., 1990; 1996; DeCaria et al., 2005; Choi et al., 2009; Apel et al., 2015). Whether NO_x is generated by lightning or lofted with other surface pollutants (e.g., carbon monoxide (CO) and hydrocarbons) into the convective cloud by updrafts, tropospheric O_3 production occurs via photochemical oxidation reactions involving CO and hydrocarbons:

$$CO + OH \rightarrow CO_2 + H \tag{R1}$$

$$H + O_2 + M \rightarrow HO_2 + M \tag{R2}$$

$$HO_2 + NO \rightarrow NO_2 + OH \tag{R3}$$

$$NO_2 + h\nu \rightarrow NO + O \quad\quad (\lambda < 420 \text{ nm}) \tag{R4}$$

$$O + O_2 + M \rightarrow O_3 + M \tag{R5}$$

net: $CO + 2\ O_2 \rightarrow CO_2 + O_3$

$$RH + OH \rightarrow R + H_2O \tag{R6}$$

$$R + O_2 + M \rightarrow RO_2 + M \tag{R7}$$

$$RO_2 + NO \rightarrow NO_2 + RO \tag{R8}$$

$$RO + O_2 \rightarrow R'CHO + HO_2 \tag{R9}$$

$$HO_2 + NO \rightarrow NO_2 + OH \tag{R3}$$

$$2\ (NO_2 + h\nu \rightarrow NO + O) \quad\quad (\lambda < 420 \text{ nm}) \tag{R4}$$

$$2\ (O + O_2 + M \rightarrow O_3 + M) \tag{R5}$$

net: $RH + 4\ O_2 \rightarrow R'CHO + H_2O + 2\ O_3$
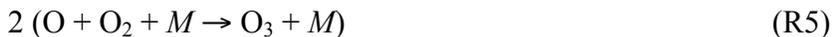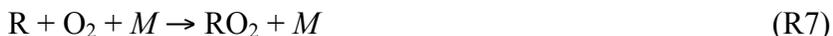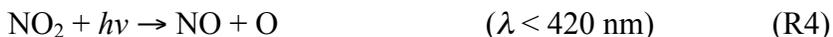
where RH is a hydrocarbon (e.g., CH_4), R is an organic group, RO_2 is an organic peroxy radical formed by hydrocarbon oxidation, and *M* represents a third body.

Ozone concentrations tend not to increase in the short-term within thunderstorms (DeCaria et al., 2005). However, in the 24-hours following a convective event LNO_x leads to enhanced O_3 production in thunderstorm outflow (DeCaria et al., 2005; Ott et al., 2007). The concentration of NO_x in the anvil dilutes as air flows downwind into the upper troposphere. This allows for O_3 production and enhancement, as NO_x catalyzes O_3 more efficiently on a per molecule basis when concentrations are diluted (Pickering et al., 1990). DeCaria et al. (2005) computed an O_3 enhancement of 10 parts per billion volume (ppbv) day^{-1} at 10.5 km in convective outflow, while Ott et al. (2007) found O_3 decreased at the same altitude, but increased 5 ppbv day^{-1} at 5.5 km. A similar enhancement from lightning (up to 16 ppbv) was found in the upper troposphere during summer 2004 over the Gulf Coast, southeast United States, and western North Atlantic (Martini et al., 2011).

Yuan et al. (2012) used observations and model-simulations to investigate enhanced O_3 production in the upper troposphere due to increases in lightning and LNO_x production associated with rises in aerosol loading from a volcanic eruption in 2005 and increased anthropogenic emissions since 1850. The pre-industrial environment was relatively clean compared to today's; therefore, an increase in aerosols would make the impact on lightning activity, O_3, and its radiative forcing more pronounced than in today's environment. Today, however, other processes, such as biomass burning and manmade emissions, which also produce O_3, mask the aerosol-lightning-ozone link, so the influence on O_3 radiative forcing due to lightning is not as strong. This change in lightning flashes is not accounted for in past climate modeling, indicating the aerosol-

lightning-ozone connection needs to be included to properly understand the changes in climate over time. It is also suggested that areas with higher pollution and larger flash rates may produce less O_3 than regions with pristine air and moderate flash rates (Ott et al., 2007) due to reduced O_3 production efficiency under high-NO_x conditions. Due to a rule set by the Environmental Protection Agency (EPA), called the NO_x State Implementation Plan (SIP), the eastern United States has observed substantial decreases in anthropogenic NO_x emissions over the last decade. With this reduction in power plant emissions it has been shown that LNO_x has a more pronounced influence on upper tropospheric O_3 production and its radiative impact than anthropogenic NO_x emissions (Choi et al., 2009; Martini et al., 2011).

A single NO molecule produced by lightning can also generate three OH molecules by photochemical oxidation, creating an enhancement in OH concentrations:

$$HO_2 + NO \rightarrow NO_2 + OH \tag{R3}$$

$$NO_2 + hv \rightarrow NO + O \qquad (\lambda < 420 \text{ nm}) \tag{R4}$$

$$O + O_2 + M \rightarrow O_3 + M \tag{R5}$$

$$O_3 + hv \rightarrow O_2 + O(^1D) \qquad (\lambda < 320 \text{ nm}) \tag{R10}$$

$$O(^1D) + H_2O \rightarrow 2 \text{ OH} \tag{R11}$$

where $O(^1D)$ is the O atom in an excited singlet state. This reaction series is significant because it illustrates the direct affect NO_x has on OH and shows how NO_x is indirectly linked to changes in climate forcing by CH_4 through control of CH_4 lifetime by OH.

CHAPTER 4: DEEP CONVECTIVE CLOUDS AND CHEMISTRY FIELD EXPERIMENT

4.1 Background

The May-June 2012 DC3 field campaign provided a multi-faceted approach to study varying types of convection (e.g., midlatitude airmass, multicell, and supercell thunderstorms), their convective transport of trace gases (e.g., anthropogenic, biogenic, and wildfire emissions), and associated lightning occurrence and NO_x production. Field experiments prior to DC3 had not investigated the influence of the environment and convection on the composition and chemistry of the upper troposphere with such a plethora of ground-based and airborne measurements of thunderstorms, the environment prior to and during convection, and the outflow downwind 12-48 hours post-convection.

The operations center was located in Salina, Kansas, which offered reasonable flight times for research aircraft to arrive at any of the three pre-determined sampling regions in northeast Colorado, central Oklahoma to west Texas, and northern Alabama. The three domains were selected based on the available instrumentation and type of convection associated with the region.

The three aircraft involved in the field campaign were the National Center for Atmospheric Research (NCAR) Gulfstream V (GV), National Aeronautics and Space Administration (NASA) DC-8, and the German DLR Falcon. The aircraft provided meteorological and chemical (i.e., trace gases and aerosols) observations of the storm inflow and outflow, in addition to background environmental conditions prior to storm development. Generally, the DC-8 focused on storm inflow, while the GV concentrated on the high-altitude outflow; however, both aircraft did sample higher and lower

altitudes, respectively, during a research flight. The Falcon also concentrated on high-altitude anvil outflow and often flew closer to the convective cores than the other aircraft.

During the campaign, meteorological and chemical tracer (e.g., LNO_x and boundary layer) forecasts were provided daily to aid decision makers in selecting where research flights would occur. On downwind flight days, forward (i.e., Flexible Particle (FLEXPART) dispersion model) and backward (Hybrid Single-Particle Lagrangian Integrated Trajectory (HYSPLIT) model) trajectories of the upper level air were analyzed to forecast the outflow plume location sampled the previous afternoon/evening. By the conclusion of the campaign, 26 intensive operational periods (IOPs) had occurred. Additional details regarding the DC3 field campaign may be found in Barth et al. (2015).

4.2 Forecast model preparation

During the DC3 experiment, the WRF model version 3.3.1 was run by NCAR at a 3-km horizontal resolution and initialized based on the 15-km Data Assimilation Research Testbed (DART) ensemble run. The model set-up included the following schemes: Morrison two-moment microphysics, Mellor-Yamada-Janjic (MYJ) PBL, Noah land surface model (LSM), the Rapid Radiative Transfer Model for General Circulation Models (GCMs) (RRTMG; Iacono et al., 2008), and no cumulus parameterization. While the WRF-Chem was not used, LNO_x was included as a tracer in the WRF model and the UV FRPS (Deierling and Petersen, 2008) provided the flashes required for the LNO_x parameterization scheme.

In order to select the FRPS to be used in the operational forecasting for DC3, I performed comparative analyses for two case study periods (i.e., 10-11 June 2010 and the DC3 test flight period from 1-15 May 2011) between flash rate observations and model

output from cloud-resolved WRF simulations using the w_{max}, CTH, and UV schemes. Both periods used the WRF model version 3.2.1 at a 3-km horizontal resolution with the Thompson microphysics and MYJ PBL schemes. Simulated total lightning flashes were determined for the convection during each case study period and compared against the total flashes estimated from the observed NLDN CG flashes using Eqn. 1 (see Chapter 2). Comparisons included: (1) the cumulative number of total flashes over the lifetime of each storm, (2) temporal correlations per 3-hour interval, and (3) spatial correlations per model processor region. The temporal and spatial correlations were used to determine how well the model simulated the timing and location of the convection.

Based on the four convective events (i.e., quasi-stationary, MCS, cold frontal system and single cell) examined during the 10-11 June 2010 case study (Cummings et al., 2012), flash rates were generally overestimated by the UV scheme and underestimated by the w_{max} and CTH schemes (Table 3); however, estimates based on CTH were reasonable for events with strong forcing (i.e., quasi-stationary systems and MCS). The temporal correlation per 3-hour interval varied by storm type and FRPS (0.41-0.93), but each scheme showed the strongest correlation (> 0.75) for the MCS (Table 4). The spatial correlation per model processor region also varied by storm type and FRPS (0.26-0.69; Table 5). Generally, the FRPSs performed equally in terms of spatial correlation for storms with stronger forcing.

Table 3. Number of observed and model-simulated total flashes for four convective case studies during 10-11 June 2010. The observed total flashes are an estimate based on the NLDN CG flashes and Equation 1.

Storm	Storm Type	Observed Flashes	Flash Rate Parameterization Scheme Model-Simulated Flashes		
			w_{max}	UV	CTH
1	Quasi-Stationary System	256,535	50,054	724,316	196,135
2	MCS	130,502	14,903	820,471	109,731
3	Cold Front	222,011	74,768	506,909	73,519
4	Single Cell	11,548	146	4,184	2,409

Table 4. Temporal correlation between the observed and model-simulated total lightning flashes for four convective case studies during 10-11 June 2010. The strongest correlation for each storm type is identified in bold font.

Storm	Storm Type	Flash Rate Parameterization Scheme		
		w_{max}	UV	CTH
1	Quasi-Stationary System	0.41	0.58	**0.65**
2	MCS	0.91	**0.93**	0.76
3	Cold Front	0.52	**0.74**	0.47
4[+]	Single Cell	---	---	---

[+] indicates storm 4 only contained two data points

Table 5. Spatial correlation between the observed and model-simulated total lightning flashes for four convective case studies during 10-11 June 2010. The strongest correlation for each storm type is identified in bold font.

Storm	Storm Type	Flash Rate Parameterization Scheme		
		w_{max}	UV	CTH
1	Quasi-Stationary System	0.55	0.62	**0.67**
2	MCS	**0.69**	0.52	0.47
3	Cold Front	0.51	**0.63**	0.54
4	Single Cell	0.26	0.26	0.29

The 10 convective events analyzed from the May 2011 DC3 test flights were associated with a short wave trough, dryline, or cold front. Each forecast run, whether it occurred the day of or the day before each selected storm, generally underestimated the observed flashes over the storm's lifetime using all three FRPSs. An example of the results for four storms is provided in Table 6. A comparison of the radar reflectivity for each of the 10 storms indicated a lack of sufficient storm intensity, which translated to substantial underestimates in the simulated flash rates. The simulated reflectivity generally forecasted shorter periods of intense convection and for about half of the storms the high reflectivities (> 50 dBZ) covered a smaller area than the observed reflectivity. Also, the forecast storms often missed the observed peak reflectivities, especially when the peak exceeded 65 dBZ. The UV scheme required the smallest scaling factor to match the observed flash rates for forecast runs 24 hours prior to and on the day the storm occurred. Temporal correlations between observed and model-simulated flashes per 3-hour interval varied by each storm and within each storm type (Table 7). Generally, the spatial correlation per processor region is weak between the observed and model-simulated flashes (Table 8). A visual analysis of the observed and model-simulated flash rates per model processor indicated the UV scheme did well capturing both the number of total flashes and their location. An example of one of the 10 convective events based on the 18 UTC run the day prior to the convection is shown in Figure 4. For forecasting 24 hours in advance, the UV scheme equally over- and underestimated the flash rates for a given convective event and provided a flash rate estimate that is closer to the observations than the other two FRPSs. Similar results were generated when model output from the day of the convection was used to predict flash rates.

Table 6. Number of observed and model-simulated total flashes for four convective case studies observed during the DC3 test flight on 3 May 2011. The observed total flashes are an estimate based on the NLDN CG flashes and Equation 1. The model output is based on the 18 UTC run on 2 May 2011, which is the day prior to the convective event.

Storm	Storm Type	Observed Flashes	Flash Rate Parameterization Scheme Model-Simulated Flashes		
			W_{max}	UV	CTH
6	Shortwave trough	4,087	330	11,631	1,194
8	Shortwave trough	101,567	2,468	7,175	2,023
12	Shortwave trough	30,211	299	13,020	2,214
13	Shortwave trough	437,836	1,537	10,166	2,634

Table 7. Temporal correlation between the observed and model-simulated total lightning flashes for four convective case studies observed during the DC3 test flight on 3 May 2011. The strongest correlation for each storm type is identified in bold font. The model output is based on the 18 UTC run on 2 May 2011, which is the day prior to the convective event.

Storm	Storm Type	Flash Rate Parameterization Scheme		
		W_{max}	UV	CTH
6	Shortwave trough	0.70	**0.93**	0.92
8	Shortwave trough	0.36	0.32	**0.57**
12	Shortwave trough	**0.59**	0.37	0.26
13	Shortwave trough	**0.88**	0.83	0.81

Table 8. Spatial correlation between the observed and model-simulated total lightning flashes for four convective case studies observed during the DC3 test flight on 3 May 2011. The model output is based on the 18 UTC run on 2 May 2011, which is the day prior to the convective event.

Storm	Storm Type	Flash Rate Parameterization Scheme		
		W_{max}	UV	CTH
6	Shortwave trough	0.92	0.46	0.25
8	Shortwave trough	-0.02	0.13	0.30
12	Shortwave trough	0.35	0.32	0.29
13	Shortwave trough	0.16	0.02	0.19

Since the final DC3 model configuration used the Morrison two-moment versus Thompson microphysics scheme, an additional case study period evaluated flash rate performance using three storms that occurred during 19-20 May 2011. The WRF model output indicated the Morrison two-moment microphysics scheme developed more intense convection than the Thompson scheme and produced 1.4-2.4 times as many flashes. Similar to previous case study, the UV scheme required the smallest scaling factors to match the adjusted NLDN flashes (Eqn. 1). Based on the results from the three separate case studies, I recommended the UV FRPS be used to forecast flash rates during DC3.

(a) NLDN observations

(b) UV scheme

(c) w_{max} scheme
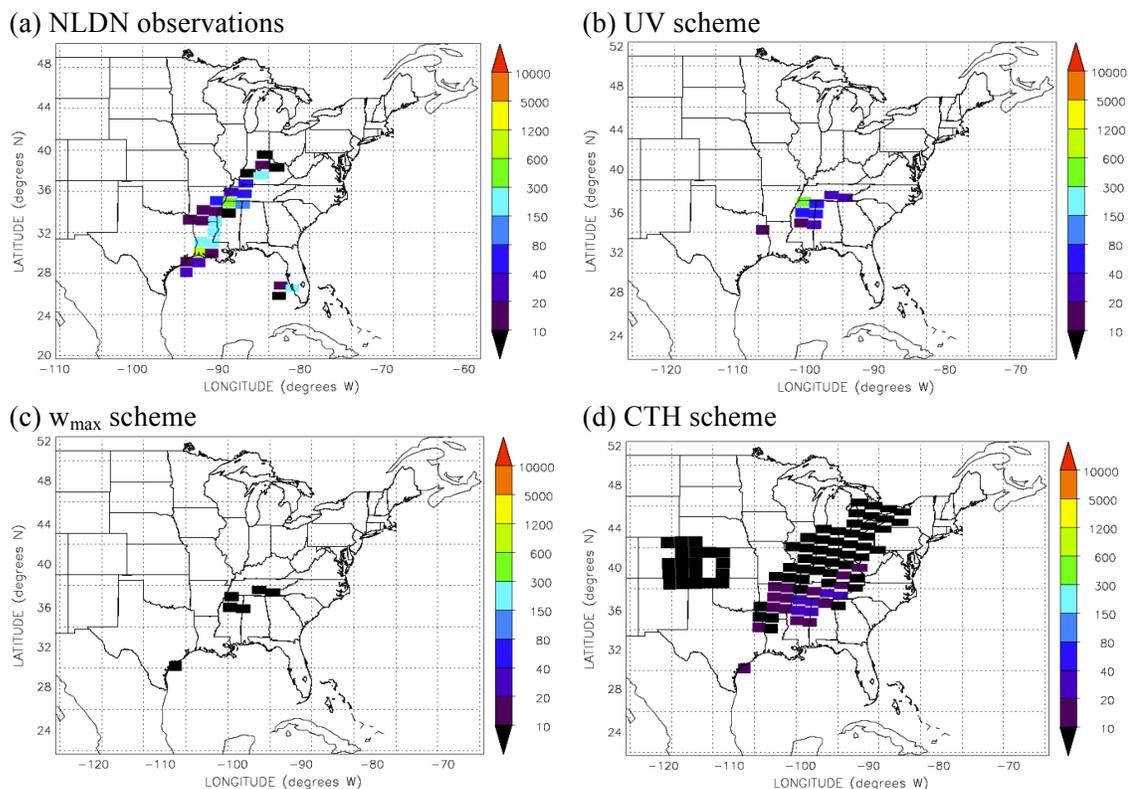
(d) CTH scheme

Figure 4. Total lightning flashes per model processor region based on (a) adjusted NLDN flashes, (b) UV scheme, (c) w_{max} scheme, and (d) CTH scheme on at 03 UTC on 3 May 2011 during the DC3 test flights. The model output is based on the 18 UTC run on 2 May 2011, which is the day prior to the convective event.

46

4.3 Tracking active convection

Following the completion of the DC3 field campaign, I developed 3-hour moving spatial masks that tracked the active convection sampled by ground stations and the DC3 aircraft during 16 of the 26 IOPs. Generally, IOPs were excluded if they focused on (1) active convection not sampled by both the GV and DC8 aircraft, (2) aged convective outflow, or (3) boundary layer emission measurements under clear sky conditions. The bounding boxes were used by Bruning (2014a, 2014b) to generate LMA total flash statistics for the thunderstorm complexes within the 2D detection range of an LMA network. This data is publicly accessible in the Earth Observing Laboratory (EOL) DC3 field catalog and provides a high level statistical summary on the LMA sources, as well as flash initiation, footprint, extent, and energy.

4.4 The 29-30 May 2012 Oklahoma severe supercell system

On the morning of 29 May 2012 conditions were very unstable and favorable for convective development within the Oklahoma domain. The 12 UTC sounding from Norman, Oklahoma, indicated the wind profile generally had a westerly component with veering from the surface to 600 hPa. A dryline was located across the Texas panhandle and a cold front stretched across the Ohio River Valley from northeast-to-southwest, with the southern portion pushing northward as a warm front over Oklahoma and Kansas. By 21:10 UTC the front was quasi-stationary and two isolated cells developed to its south along the Kansas-Oklahoma border and ahead of the dryline. Over the next several hours both storms formed mid-level mesocyclones (DiGangi et al., 2016) and evolved into a line of supercells. The line continued in an east-southeast direction as new cells formed

behind it and underneath the anvil. The severe supercell system evolved into a multicell MCS by 03:00 UTC on 30 May and moved through central Oklahoma within the hour.

Meteorological data collected by ground-based instrumentation in the Oklahoma domain include radar data from the NSSL WSR-88D or Next Generation Radar (NEXRAD) located near Norman, Oklahoma, and the NSSL's NOAA X-band polarimetric (NOXP) and C-band Shared Mobile Atmospheric Research and Teaching (SMART) radars. Lightning data are provided by ground-based facilities via the central Oklahoma LMA network and NLDN. The total lightning flash detection efficiency provided by the 11 stations in this LMA network is > 90% at a 200 km radius (Chmielewski and Bruning, 2016). The convection developed between the northern edges of the LMA network's 2D and 3D lightning detection coverage (Figure 5). As the storm system progressed east-southeastward, it stayed within the 2D coverage of the network for the majority of its life (21:10-04:19 UTC) and was generally within the 3D coverage area between 23:40-03:00 UTC when the flashes were within roughly a 100 km radius. The NLDN CG flash detection efficiency is 90-95% over the continental United States (Cummins and Murphy, 2009).
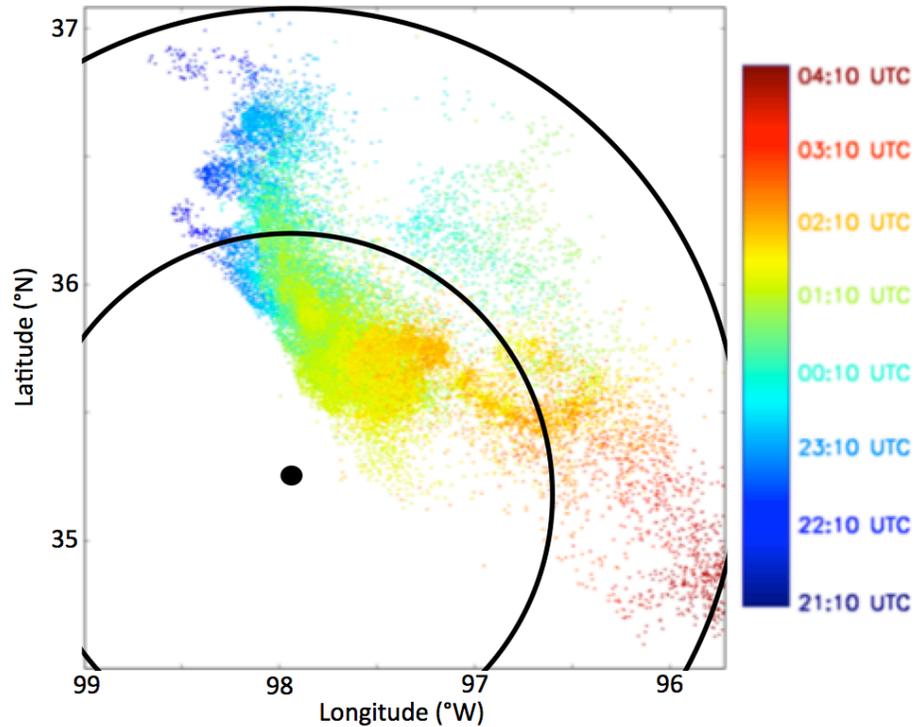
Figure 5. Total lightning flashes observed by central OK LMA network from 21:10 UTC on 29 May to 04:20 UTC on 30 May 2012. The 3D and 2D lightning detection coverage is represented by the 100 km and 200 km radius from the center of the network, respectively. The network center is located at approximately 35.279 °N, 97.918 °W.

The observed total lightning flash rate time series was generated from a grid of LMA data with 1-min temporal and 1-km spatial resolution. Figure 6 shows that the maximum flash rate observed by the LMA occurred at 01:37 UTC (312 flashes min^{-1}). The CG flash rate time series was produced from the observed NLDN flash data with weak positive CG flashes (peak current < +15 kA) filtered out. The peak CG flash rate (94 flashes min^{-1}; Figure 6) occurred roughly 15 minutes later (01:51 UTC). Approximately 8,679 CG and 31,633 total flashes were observed over the lifetime of the convection with an average total flash rate of 75.5 flashes min^{-1}. Roughly 15,060 total flashes occurred during the 5-hour period simulated in our case study (20:00-01:00 UTC observed time), with an average total flash rate of 68.5 total flashes min^{-1}. The 1-min

data from both networks were binned into 10-min intervals (Figure 7) to match the output

from the WRF model. The total flash rate time series shows several distinct peaks as the

flash rate increased from 21:30 UTC to the maximum (~2,600 flashes 10-min^{-1}) at 01:40

UTC. These peaks occured at 22:00 UTC, 22:50 UTC, 23:50 UTC, and 01:00 UTC with

roughly 100, 300, 800, and 2,200 total flashes 10-min^{-1}, respectively. Following the

primary peak, the observed flash rate decreased at a faster rate than it increased. The 29-

30 May 2012 convection contained high flash rate supercells with small flash extents

(Barth et al., 2015). DiGangi et al. (2016) also showed the Kingfisher storm, which was

within the southern portion of the convection analyzed in this case study, had an

abundance of small flashes, especially during its mature phase, when flash rates were

> 100 flashes min^{-1}.

The 10-minute time evolving intracloud to cloud-to-ground (IC:CG) flash ratios

were calculated over the life of the storm using the observed NLDN CG and LMA total

lightning flash data (Figure 8). The LMA data was partitioned into IC and CG flashes by

matching the timing and location of the NLDN CG and LMA total flash data. The mean

time varying IC:CG ratio over the storm lifetime is 2.73±2.51, while the mean for the 5-

hour simulation period is slightly higher (3.93±2.22).

During this mission the DC8 focused on storm inflow and outflow, while the GV

concentrated on high-altitude outflow. The 1-sec DC8 and GV aircraft data is averaged

over 5 sec and 4 sec, respectively, to correspond with the 1 km × 1 km horizontal

resolution of the model data. NO_x measurements were not available for the Falcon for

this research flight. The NSSL Mobile GPS Advanced Upper-Air Sounding System

(MGAUS) provided upper air data in the vicinity of the storm. Three mobile soundings

were deployed at 20:29 UTC (35.667 °N, 98.341 °W) and 22:55 UTC (35.854 °N,

98.066 °W) on 29 May and 00:21 UTC (35.595 °N, 97.859 °W) on 30 May (Ziegler,

2013b). The 22:55 UTC sounding lost data as the radiosonde passed through the anvil

and is spliced with data from the 20:29 UTC sounding above 435 hPa, since the upper air

profile likely changes more slowly in the upper versus lower troposphere (Conrad

Ziegler, personal communication, April 18, 2017). Visible satellite imagery from the

Geostationary Operational Environmental Satellite-13 (GOES-13) was used to estimate

the anvil area of the observed storm system from 21:10-01:00 UTC, prior to reduction in

sunlight and the quality of the visible images.
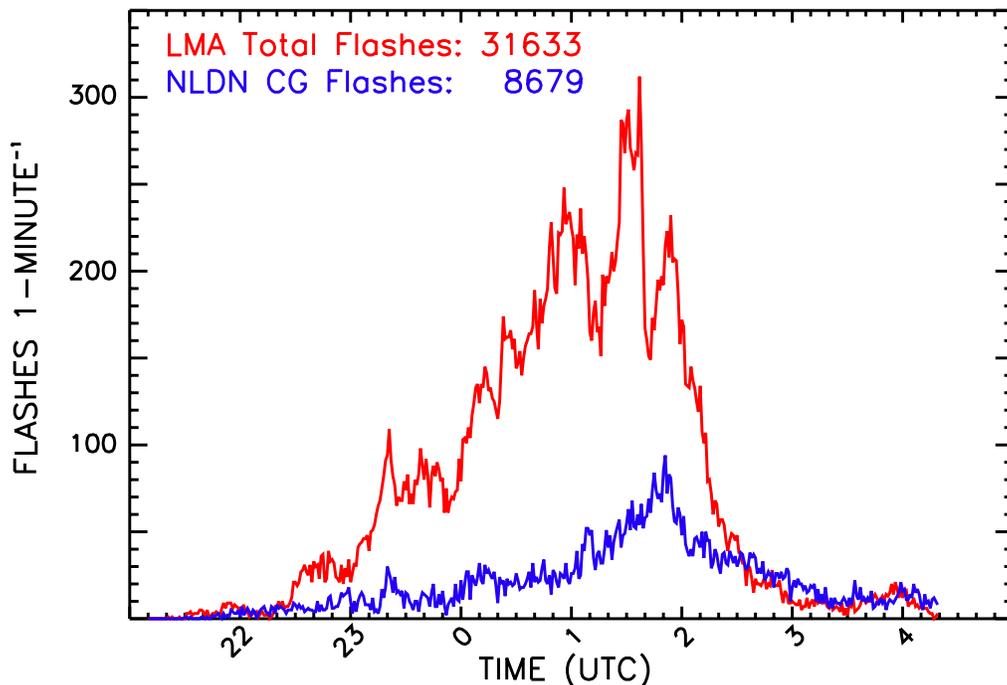
Figure 6. The Oklahoma LMA total and NLDN CG lightning flash data per 1-minute
provided for the lifetime of the observed 29-30 May 2012 severe supercell system
(21:10-04:19 UTC).
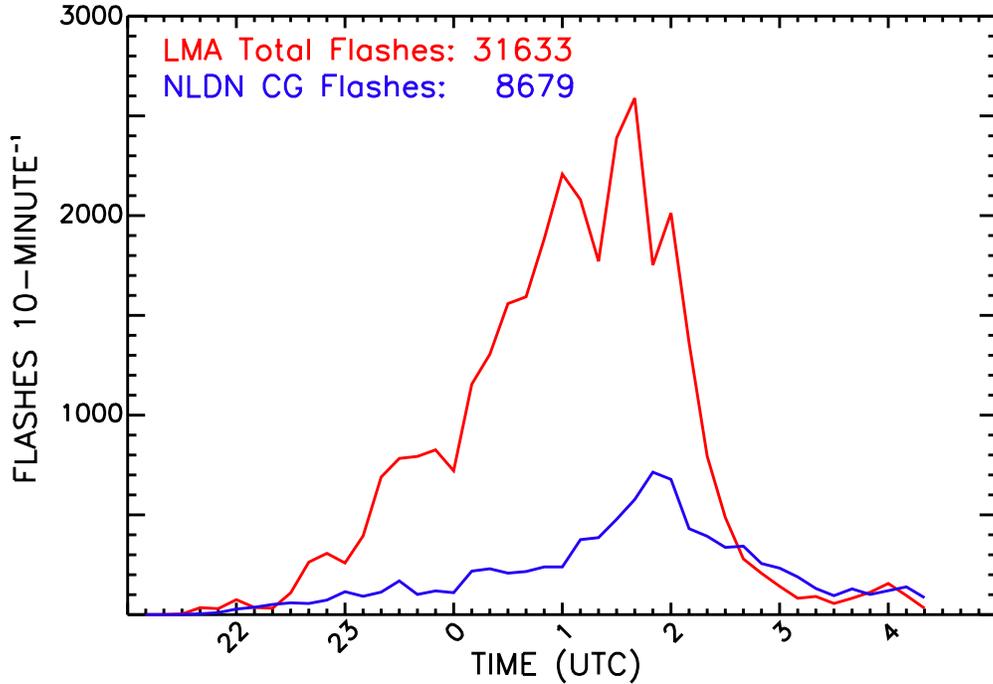
Figure 7. The Oklahoma LMA total and NLDN CG lightning flash data per 10-minutes provided over the lifetime of the observed 29-30 May 2012 severe supercell system (21:10-04:19 UTC).
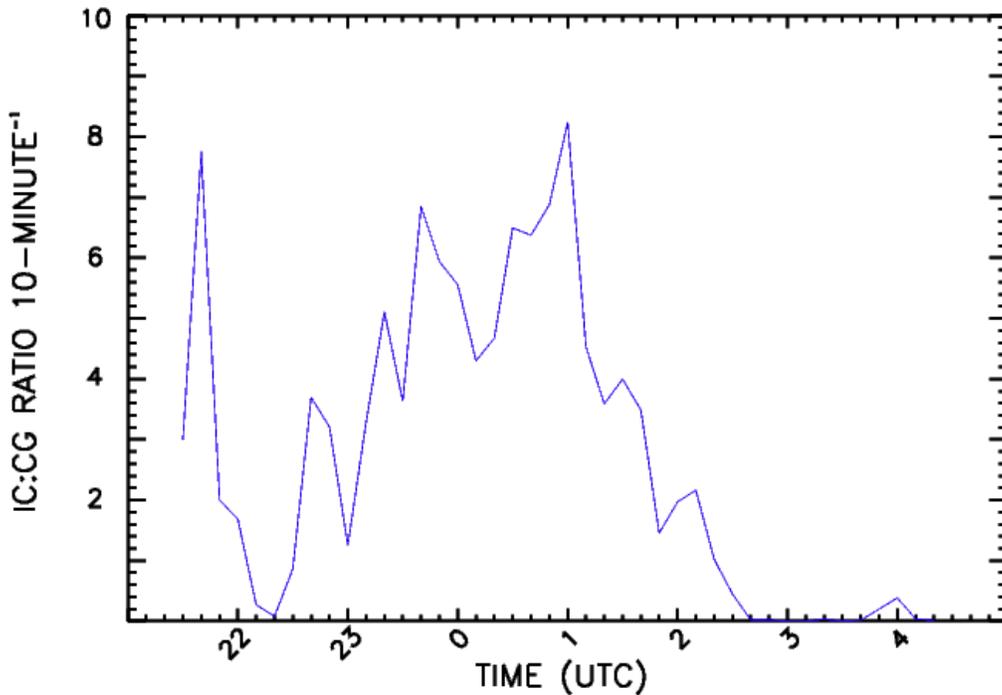
Figure 8. The IC:CG ratios per 10-minutes provided over the lifetime of the observed 29-30 May 2012 severe supercell system (21:10-04:19 UTC). The ratios are based on the Oklahoma LMA total lightning and NLDN CG flash data in Figure 7.

CHAPTER 5: WEATHER RESEARCH AND FORECASTING MODEL WITH CHEMISTRY

The WRF-Chem is a cloud-resolving model, which combines the mesoscale forecasting capabilities of the WRF model with chemistry modeling (Grell et al., 2005). The WRF-Chem allows for online simulations, which more accurately characterize the production and transport of trace gases and aerosols than offline simulations and guarantees consistency with the meteorological fields. It can be initialized and constrained by the larger-scale meteorological conditions provided by sources such as the Global Forecasting System (GFS). The model also allows the inclusion of feedback processes of the chemistry and aerosols on the meteorological fields, which is significant when determining the effects of chemistry on climate.

The physical and chemical processes represented in the WRF-Chem include transport, deposition, emission, chemical transformation, aerosol interactions, photolysis, and radiation (Grell et al., 2005). The LNO_x production may be estimated for both cloud-resolved and parameterized convection given the lightning flash rate time series, the horizontal and vertical distribution of lightning flashes, and the NO production per IC and CG flashes. Flash rates can either be predicted from storm parameters (see Section 2.3) or, to reduce uncertainty, prescribed directly from lightning observations (DeCaria et al., 2005; Ott et al., 2010; Cummings et al., 2013). Likewise, the flash type can be predicted (Price and Rind, 1993; Pickering et al., 1998; Fehr et al., 2004) or prescribed from observations (DeCaria et al., 2005; Ott et al., 2007, 2010; Cummings et al., 2013).

5.1 Model set-up

Bela et al. (2016) simulated the 29-30 May supercell system at cloud-resolved resolution using the WRF-Chem model, version 3.6.1. We use the same model conditions as Bela et al. (2016), but with some modifications, which are outlined below, to improve the model-observations agreement. The model domain contains $480 \times 420 \times 89$ grid points in the x, y, and z directions with 1-km horizontal resolution and variable vertical resolution from 50 m near the surface to 250 m at the top of the domain (50 hPa). The southwest corner of the domain is located at 33.8196 °N, -99.7726 °W and the northeast corner is located at 38.1354 °N, -95.0998 °W. The initial 8-hour simulation ran from 18:00 UTC on 29 May to 02:00 UTC on 30 May using 480 processors on the NCAR Yellowstone supercomputer. The simulation does not extend past 02:00 UTC because we are interested in the time period when lightning would be influencing the NO_x mixing ratios sampled by the DC3 aircraft in the anvil outflow (Cummings et al., 2017a). For subsequent simulations a restart file was used at 21:00 UTC to reduce computation time since the observed convection began just after 21:00 UTC. The simulation is integrated with a 3 sec time step, while the lightning parameterization is called every 6 sec.

The initial model configuration and physics and chemistry options are based on Bela et al. (2016) Meteorological initial and boundary conditions were provided by the 6-hour interval North American Mesoscale Analysis (NAM-ANL) at 12 km resolution. The constant initial and boundary chemistry conditions are reset at 21 UTC using a combination of data from the DC8 profile (i.e., for the boundary layer and free troposphere) and the Model for Ozone and Related chemical Tracers version 4 (MOZART; available from NCAR). Table 9 provides the final model physics and

chemistry options selected for this analysis. Detailed descriptions of some of the selected

schemes are provided below.

Table 9. WRF model physics and chemistry options selected for 29-30 May 2012
Oklahoma case study.

WRF Model Options	Name of Scheme
Microphysics	Morrison two-moment scheme
Planetary boundary layer	YSU scheme
Surface layer	MM5 similarity scheme
Land surface	Unified Noah LSM
Radiation (shortwave & longwave)	RRTMG
Cumulus parameterization	None
Convective damping	21:00-21:20 UTC (Li et al., 2017)
Lightning data assimilation	21:30-23:00 UTC (Fierro et al., 2012)
Lightning flash rate parameterization	• 18 FRPSs (Table 1) • IC:CG ratios based on LMA & NLDN observations
LNO_x vertical & horizontal distributions	• Observed CG & IC flash channel vertical distributions • Radar reflectivity $\geq$ 20 dBZ
Temperature of peak of LNO_x vertical distribution for lightning	• IC peak = - 45 °C • CG peak = - 40 °C
Moles NO emitted per flash	• IC = 82; CG = 82
Chemical mechanism	MOZCART (MOZART chemistry & GOCART aerosols)
Wet scavenging & ice retention	Assume zero retention for trace gases (Bela et al., 2016)

The Morrison two-moment microphysics scheme predicts the mass mixing ratio

for cloud droplets, and both mass and number mixing ratios for rain, cloud ice, snow, and

graupel/hail (Morrison et al., 2015). The dense precipitating ice options can influence the

storm structure, cold pool, and precipitation of deep convection due to differences in their

terminal fall speed and bulk density (Morrison and Milbrandt, 2011; Bryan and Morrison,

2012; Adams-Selin et al., 2013; van Weverberg, 2013). For severe continental deep

convection, such as the 29-30 May case study, we set the dense precipitating ice to have hail characteristics.

MOZART is an offline global chemical transport model, which is suited for the troposphere (Emmons et al., 2010). The output from MOZART is used for chemical initial and boundary conditions the WRF-Chem regional model. Several of the WRF-Chem online calculations include photolysis rates, dry deposition, and biogenic emissions. Several gas-phase chemistry mechanisms are available for use in WRF-Chem. I have selected the MOZART mechanism to be consistent with the incoming initial and boundary conditions. This chemical mechanism contains gas-phase species, bulk aerosol compounds, and photolysis and gas-phase reactions, in addition to an updated isoprene oxidation scheme and a separation of volatile organic compounds into three groups (i.e., alkanes, alkenes, and aromatics). The MOZART chemical scheme is connected to WRF-Chem via the Kinetic PreProcessor (KPP) and can be combined with the Georgia Tech/Goddard Chemistry Aerosol Radiation and Transport (GOCART) aerosol scheme (MOZCART). To simulate the observed trace gas mixing ratios in storm outflow, Bela et al. (2016) found an ice retention assumption of zero for all species (i.e., formaldehyde (CH_2O), hydrogen peroxide (H_2O_2), HNO_3, sulfur dioxide, and methyl hydrogen peroxide) provided the best agreement for CH_2O and H_2O_2 observations when used in combination with MOZART's simple wet scavenging scheme (i.e., Neu and Prather, 2012).

The GOCART model is generally a bulk aerosol scheme, which determines the total mass of each aerosol type, but does not provide particle size information, except for dust and sea salt (Chin et al., 2000). This scheme is considered numerically efficient and

56

allows for simulations with complex gas-phase and aqueous chemistry. GOCART is

connected with the radiation schemes in WRF-Chem, such that the direct effect of

aerosols can be considered. However, it is not connected with the cloud microphysics

schemes in the WRF-Chem version used for this case study. Therefore, the indirect

effects associated with clouds cannot be computed with this aerosol scheme. Additional

types of aerosol modules are also available in WRF-Chem (i.e., modal and sectional).

5.2 Convective damping and lightning data assimilation techniques

Methods can be used to guide the model when simulations do not reproduce the observed

convection in the correct space or time. I implemented these techniques in this cloud-

resolved simulation as a way to try to bring the hydrometeors in the WRF simulated

storm closer in the line with the proxy observations (Cummings et al., 2017a).

The convective damping technique clears convection from the model prior to the

observed convective initiation by reducing the model-simulated water vapor at each 3D

grid point where relative humidity exceeds a specific threshold (Li et al., 2017). In the

29-30 May case study, water vapor was constrained to be less than a relative humidity of

75% from 21:00-21:30 UTC (prior to the beginning of continuous observed lightning

flashes at 21:31 UTC) in order to decrease excessive buoyancy.

Fierro et al. (2012) developed a lightning data assimilation (LDA) technique to

guide the placement of water vapor, so buoyancy is generated at the proper times and

locations for convective development. Their equation is:

$$Q_v = AQ_{sat} + BQ_{sat} \tan(CX) \left[1 - \tanh\left(DQ_g^{2.2}\right)\right], \qquad (2)$$

where Q_v is the water vapor mixing ratio (g kg^{-1}), Q_{sat} is the water vapor saturated

mixing ratio (g kg^{-1}), Q_g is the graupel mixing ratio (g kg^{-1}), X is the flash rate, and

constant coefficients are represented by A, B, C, and D. For this case study, the

coefficient values are 0.93, 0.20, 0.01, and 0.25, respectively. Coefficient A controls the

minimum threshold for relative humidity within a grid column to ensure the relative

humidity stays above a predefined minimum value (93%). The default value for

coefficient A is 0.81, but can be increased for weakly electrified storms (Fierro et al.,

2012). While this case study is considered a high flash rate event, coefficient A was

varied between 0.81 and 0.95. A value of 0.93 provided a closer representation of the

observed storm when used in combination with the convective damping and other LDA

variables. Previous studies have added water vapor back into the column within the

mixed-phase graupel-rich region (0 °C to -20 °C) (Fierro et al., 2012), the lower

troposphere (< 700 mb) (Marchand and Fuelberg, 2014; Fierro et al., 2016), and between

the lifting condensation level (LCL) and w$_{max}$ height (Li et al., 2017). Our focus was on

improving the mixing ratio and vertical placement of the simulated hydrometeors (e.g.,

graupel), so water vapor was introduced between the LCL (16 °C) and the lower level of

the mixed-phase region (-5 °C). If this lower limit was extended to colder temperatures,

it is possible the water vapor may instantly deposit onto ice particles and not provide the

desired improvement.

The lightning stroke counts detected by the Earth Network Total Lightning

Networks (ENTLN) from 21:30-23:00 UTC (i.e., roughly the beginning of the continuous

lightning to the mature stage) were gridded using the same 1 km × 1km horizontal

resolution as the WRF and introduced into the model over the same time period. At

model grid points with more than one stroke, graupel mixing ratios < 3.0 g kg^{-1}, and ambient relative humidity < 95%, the LDA modifies the water vapor between -5 °C and 16 °C. The relative humidity is also constrained to be ≤ 103%.

5.3 Lightning flash rate parameterization in WRF-Chem

The w_{max} and CTH FRPSs are the only schemes currently available in the publicly accessible version of the WRF. I added the other 16 FRPSs provided in Table 1 for this case study. I also wrote the code for 11 of the 16 schemes (i.e., schemes developed after 2009) and made slight modifications to all 18 schemes (i.e., hydrometeor scaling). The equations for all 18 FRPSs (Table 1), except the ICEFLUX and LTG3 schemes, are calculated for bulk quantities in each computer processor within the model domain. Each processor is roughly 18 km × 19 km in area and will likely contain either complete or partial storm cores as the simulated storm moves through the domain. This approach could overestimate total lightning flashes for the linear schemes with positive y-intercepts, as well as non-linear schemes. Flash rates may also be underestimated by linear schemes with negative y-intercepts.

In addition, the linear FRPSs with non-zero y-intercepts are only used when the storm parameter calculated for the processor exceeds a specific minimum value. This prevents negative flash rates, which are not realistic, from occurring in the UV, IWP, and PIM schemes and positive flash rates from occurring when the IMFP value is zero.

The WRF provides several options for controlling the IC:CG ratio. One method uses the coarsely prescribed ratios based on the 1995-1999 NLDN/OTD climatologies from Boccippio et al. (2001). For this case study, this method assigns an IC:CG ratio of 3.55 to the central United States (90-105 °W). This ratio is similar to the climatological

mean IC:CG ratio calculated specifically for the Oklahoma domain (3.90±0.49), which is based on the Boccippio gridded data for May. I replaced the single climatological value for the central United States (3.55) by the actual observed 10-minute time evolving IC:CG ratios (Figure 8) only within the area of the associated 10-minute moving spatial mask that surrounds the storm system.

5.4 Lightning NO$_x$ parameterization in WRF-Chem

I replaced the default Gaussian vertical distributions for CG and IC lightning, which are appropriate for WRF-Chem thunderstorm simulations at cloud-resolved scales (DeCaria et al., 2000), with the observed vertical profiles constructed using the source data detected by the central Oklahoma LMA network during the 29-30 May convective event. The observed CG and IC vertical distributions at 1-min resolution showed the profile shape and the altitude of the peak in flash channel lengths varied over the lifetime of the convection; however, the mean profiles for both flash types were unimodal Gaussian distributions (Figure 9). The CG vertical profile maximizes at a considerably colder temperature (-40 °C or 9.5 km) than the default vertical distribution (-15 °C or 6 km). The observed and default IC vertical profiles both peak at -45 °C (10.5 km), but the observed profile does not have the lower second peak shown in the default distribution. The horizontal placement of the LNO$_x$ follows the bulk approach and is injected within the 20 dBZ reflectivity contour (DeCaria et al., 2005; Ott et al., 2010). The radar reflectivity threshold is not modified because the majority of the observed LMA sources are within the 20 dBZ contour (Figure 10).
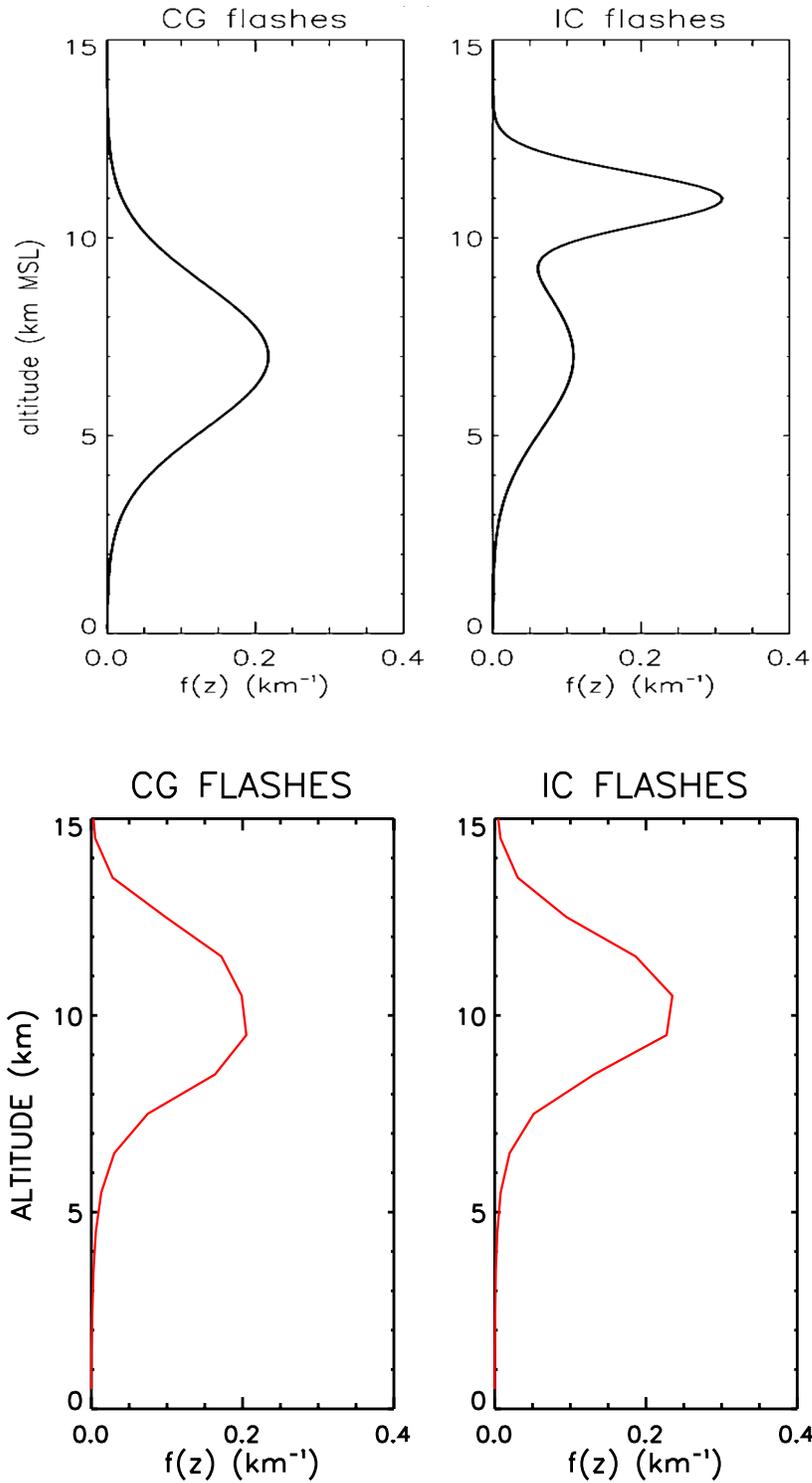
Figure 9. (Top) The default CG and IC vertical distributions of flash channel lengths by DeCaria et al. (2000). (Bottom) The mean CG and IC vertical distributions of flash channel lengths observed 29-30 May 2012 severe supercell system.

Prior analyses for the 29-30 May convective event suggested an LNO_x production scenario of 125 moles NO flash[-1] was appropriate (Bela et al., 2016; Cummings et al., 2016) given the default model parameters for the flash channel vertical profiles (DeCaria et al., 2000) and IC:CG ratio (Boccippio et al., 2001). However, I tested additional scenarios with the modified model to determine if a different amount of LNO_x or unequal LNO_x production per CG and IC flash provide a closer representation of the aircraft observed NO_x in the anvil outflow.
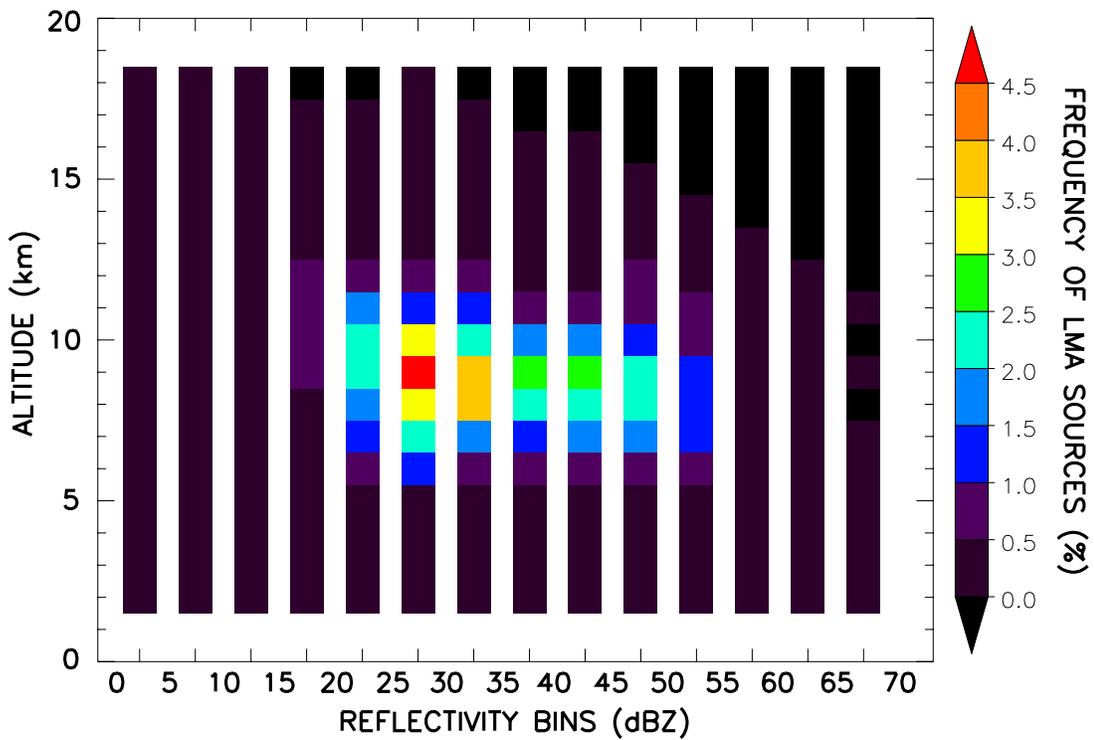
Figure 10. Percentage of VHF sources observed by the central Oklahoma LMA from the 29-30 May 2012 severe supercell system (21:10-04:19 UTC) by altitude and reflectivity.

CHAPTER 6: EVALUATION OF METEOROLOGICAL CONDITIONS AND LIGHTNING

Prior to inclusion of the convective damping and LDA techniques, the WRF represented the observed storm location, dimensions, and vertical motion reasonably well; however, the model-simulated anvil area was ~60-95% smaller than the observations during the first hour and roughly 20-50% smaller after that time. Thirteen of the 18 FRPSs also grossly overestimated (> 100%) the LMA flash rates observed in the 29-30 May severe supercell system. Every hydrometeor-based scheme overpredicted, which prompted an investigation of the model-simulated hydrometeor mixing ratios and their location within the convection.

The damping and LDA methods were tested with the intent of improving the location and mixing ratio of the hydrometeors in the model. By removing excess moisture from the atmosphere in locations with no observed convection and then guiding water vapor back into the atmosphere with the help of lightning observations, the maximum graupel mixing ratio decreased by ~2 g kg^{-1} and the height of the maximum appeared to lower by ~1 km. While these methods have provided the best results thus far for modifying the hydrometeors in this case study, the remaining differences between the proxy observations (Section 6.2) and WRF simulation are likely due to microphysics scheme assumptions. The simulation results in Section 6.1 are based on the model's final configuration, which includes damping and LDA (Table 9).

In addition to incorporating the damping and LDA, several other approaches were used to explore the overprediction. These included assigning thresholds to the frozen hydrometeors and scaling the model hydrometeors to proxy observations. Each approach

is described in Section 6.2. The NSSL two-moment microphysics scheme (Mansell et al., 2010) was also tested using the LDA assumptions of Bela et al. (2016) and the damping and LDA assumptions in this study; however, both simulations yielded a poorer representation of the storm system. The FRPS performance is evaluated in Section 6.3 using the final model configuration, as well as a set of criteria and hydrometeor scalings. A discussion about why the FRPSs succeeded and failed in replicating the observed flash rate trends follows in Section 6.4.

6.1 Meteorological conditions

The observed and model-simulated storms both initiated along the Kansas-Oklahoma border. The model-simulated storm initiated at 22:10 UTC, approximately an hour after the observed convection; however, as the simulated convection matures the offset is 30-50 minutes. Figure 11 shows the location of the observed (left column) and simulated (right column) cells at the observed and model times where the spatial agreement is best. Figures 11a and 11b show the location of the observed and simulated cells 40 minutes after their respective initiations. As the cells form a north-south line, both the observations (Figure 11e) and model (Figure 11f) indicate radar reflectivities of 60-65 dBZ in similar locations. To the east of the line new cells develop beneath the anvil, although the model-simulated cells (Figure 11h) are not as individualized as the observations (Figure 11g). While the observations show an orientation of the line toward the southeast, the WRF tilts the line toward the southwest by the end of the simulation. However, both the NEXRAD (Figure 11i) and WRF (Figure 11j) indicate that the southernmost cell in the main system is most dominant (the "Kingfisher storm").
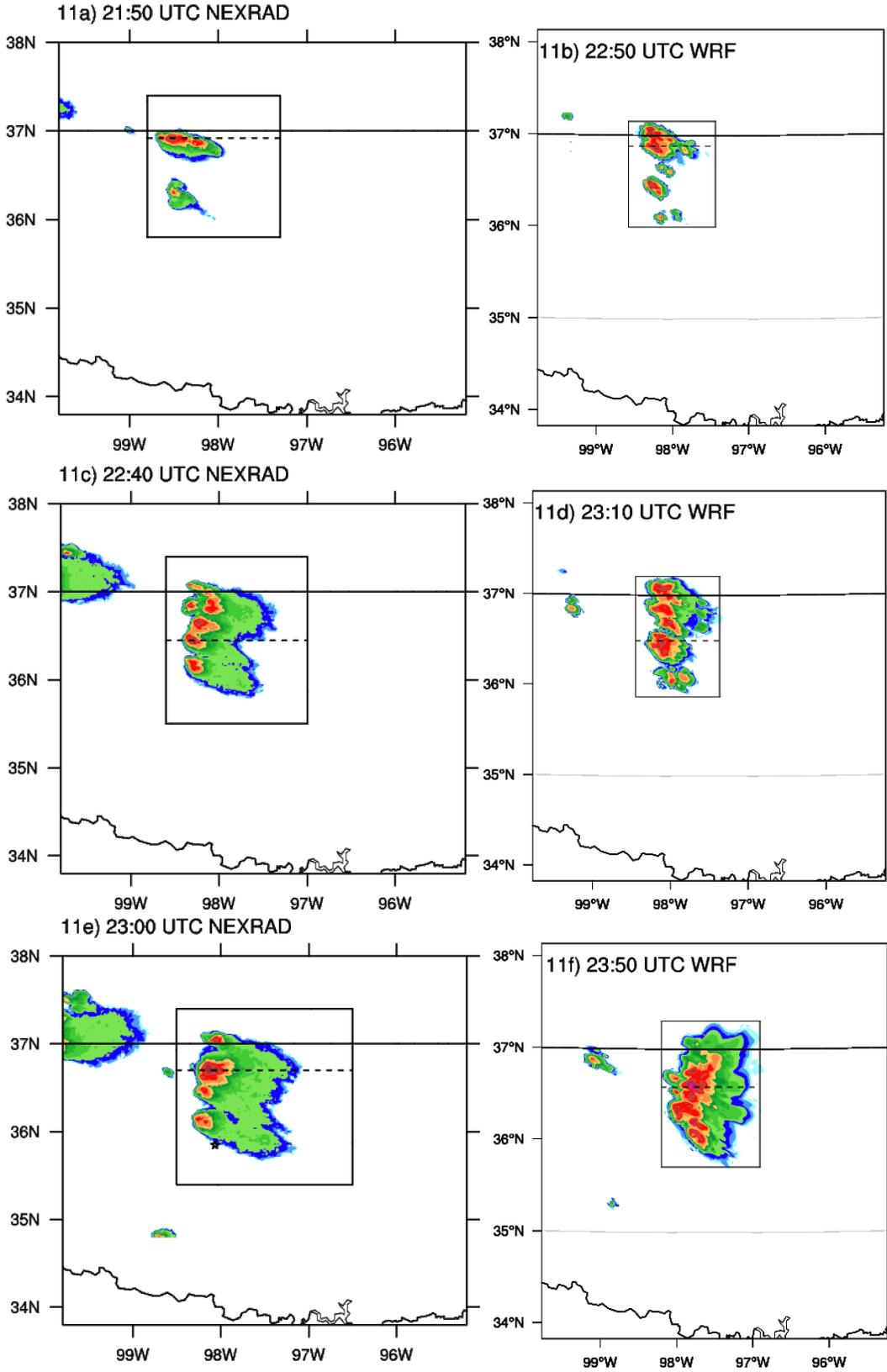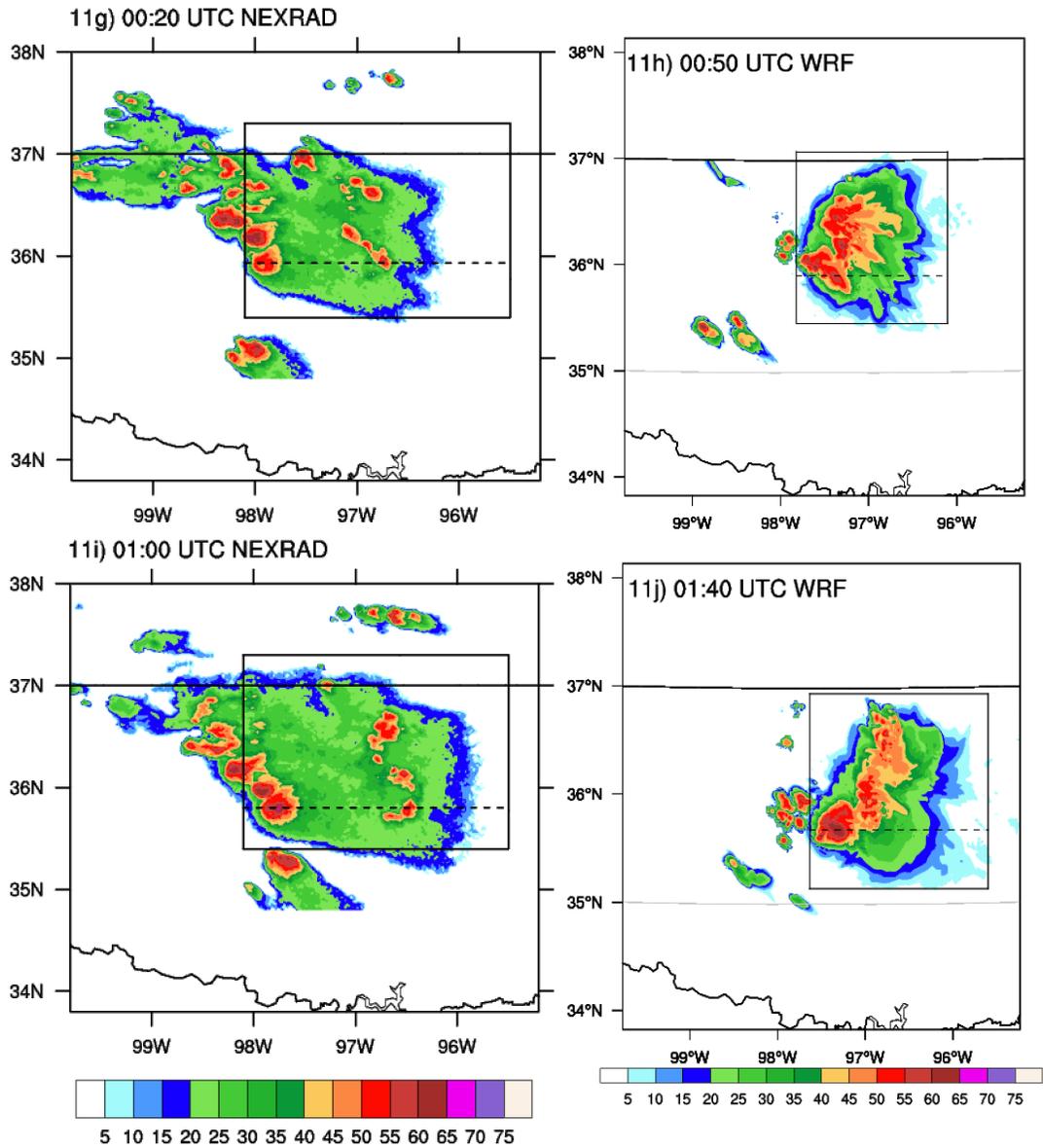
Figure 11. Composite radar reflectivity from the 29-30 May 2012 severe supercell system for the observed storm at (11a) 21:50 UTC, (11c) 22:40 UTC, (11e) 23:00 UTC, (11g) 00:20 UTC, and (11i) 01:00 UTC observed time, and the WRF model-simulated storm with damping and LDA techniques at (11b) 22:50 UTC, (11d) 23:10 UTC, (11f) 23:50 UTC, (11h) 00:50 UTC, and (11j) 01:40 UTC model time. Note, there is a 1-hour delay in the model-simulated storm initiation, but this offset is not maintained as the storm matures. The black box in each image highlights the portion of the convection that is the focus of the observed and modeled storm at the selected time. The black dashed line in a plot represents where a vertical cross section is located.

The WRF simulation captures several additional aspects of the severe supercell system: (1) the east-southeast progression of the line and the cells that form to its east and west, (2) the development of the "Kingfisher storm" and its merger with the northern cell, and (3) the initiation and northeast motion of the cell to the south that merges with the convective system. However, the convection to the northwest and southwest of the line of supercells is slightly delayed in the model. A comparison between the observed visible satellite imagery and the model-simulated total hydrometeors (i.e., cloud water, rain, snow, ice and hail) at 10.5 km altitude from 22:10-01:00 UTC model time suggests the model storm underestimates the anvil area by ~60-70% for the initial 30-40 minutes of development and is then within 10% until 01:00 UTC model time (Figure 12). The eastern edge of the anvil begins to move outside the model domain after 01:00 UTC; therefore, no further comparisons were made.
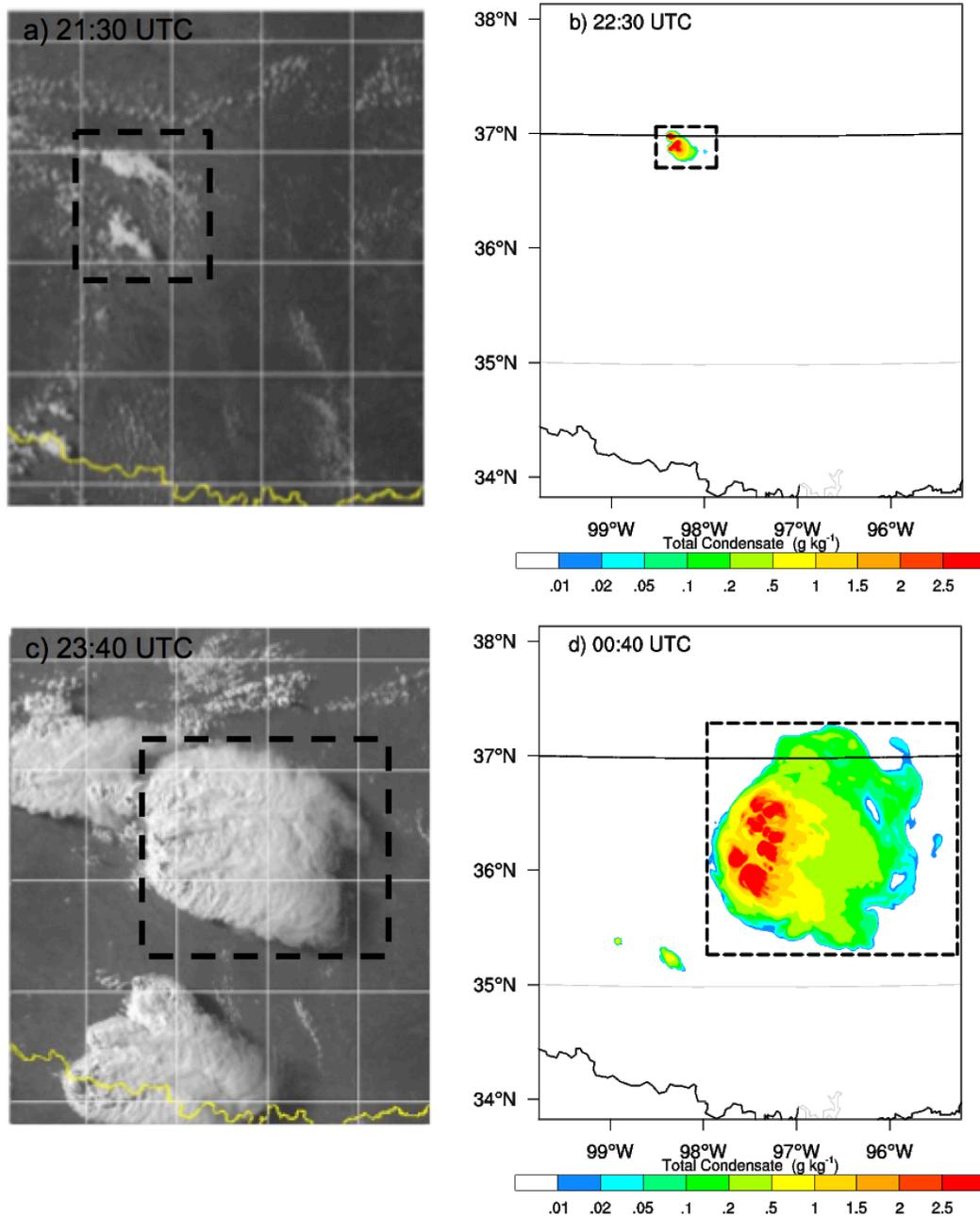
Figure 12. Comparison of the anvil area from the 29-30 May 2012 severe supercell system detected by GOES-13 at (a) 21:30 UTC and (c) 23:40 UTC observed time and by the WRF model-simulated total hydrometeors (g kg^{-1}) at 10.5 km altitude at (b) 22:30 UTC and (d) 00:40 UTC model time. The dashed black box in each image highlights the portion of the convection that is the focus of the observed and modeled storm at the selected time.

The model-simulated composite radar reflectivity suggested the size of the convective cores was similar to the storm observed by NEXRAD, both in the horizontal and vertical. Generally the convective regions (>30 dBZ) had dimensions of 20-40 km in the east-west and 20-30 km in the north-south directions for both the observed and model-simulated storms. However, the model has difficulty maintaining the individualized areas of higher reflectivity that are noted in the NEXRAD composite reflectivity. While the LDA was being applied, the convective cells in the simulated storm appeared more individualized, as in the observations. After the LDA stopped, it became more difficult to discern individual cells as the areas of simulated higher reflectivity appeared to merge. The maximum radar reflectivity simulated by the model (~69 dBZ) was within the range of the observations (65-70 dBZ). The 0 dBZ contour indicates the model-simulated radar top of the storm (~16 km) was within 10% of the observed radar top height (~17 km). Unlike the observations, radar reflectivities > 50 dBZ tend not to extend above roughly 6 km altitude in the model (Figure 13).
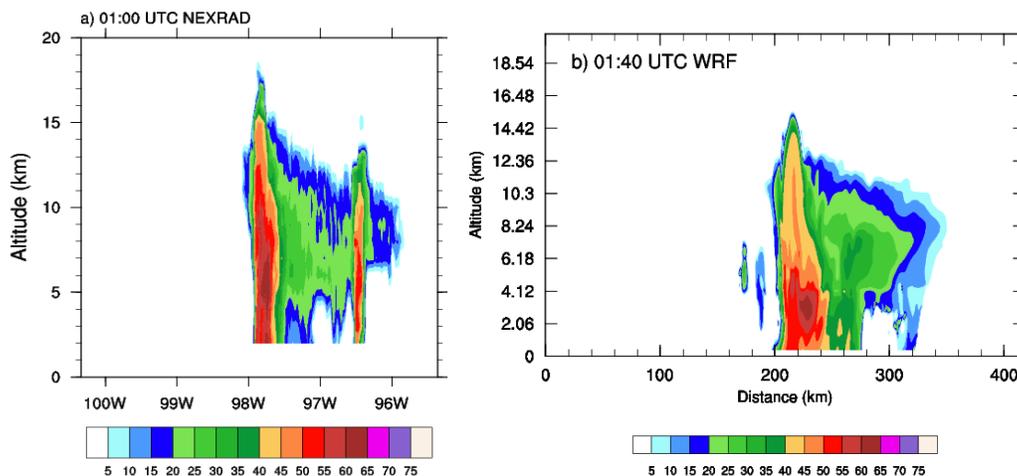
Figure 13. Vertical cross-section of composite radar reflectivity from the 29-30 May 2012 severe supercell system for the (a) observed storm at 01:00 UTC observed time and (b) WRF model storm with damping and LDA techniques at 01:40 UTC model time.

Since six FRPSs rely on radar reflectivity to compute storm parameters, the observed and model-simulated radar volumes are compared. During the first hour the observed 18 dBZ, 25 dBZ, and 35 dBZ echo volumes are underestimated by ~16%, overestimated by ~23%, and overestimated by ~500%, respectively. The simulated echo volumes overestimated the observations by ~10-35% over the next 1.5-2 hours and underestimated the observations by ~15-30% the last 1-1.5 hours. This suggests the model storm is initially too intense based on the large overestimation of the 35 dBZ volume, but becomes more similar to the observations as the storm matures.

The model-simulated convection generated a maximum vertical velocity (~62 m s^{-1}) within ~5% of the mobile radars observations (~65 m s^{-1}) (DiGangi et al., 2016). The observed and simulated maximum values both occurred in the southernmost cell of the system at the same time relative to storm initiation (23:30 UTC observed time and 00:30 UTC model time), but the maximum was located at 8-9.5 km altitude in the observations (Bela et al., 2016) and at ~10 km altitude in the simulation. The WRF model generates a storm in an environment with a mixed-layer convective available potential energy (MLCAPE) of 2553 J kg^{-1}. This is similar to the 22:55 UTC observed mobile sounding (2759 J kg^{-1}), although the simulated upper air profile is slightly drier in the boundary layer and more moist in the upper troposphere, particularly at ~240 hPa (Figure 14). Similar to the observed sounding, the simulated profile indicates veering in the lower troposphere with upper level winds with a westerly component, along with a surface-6 km bulk shear (25 m s^{-1}) that is comparable to the observations (24 m s^{-1}).
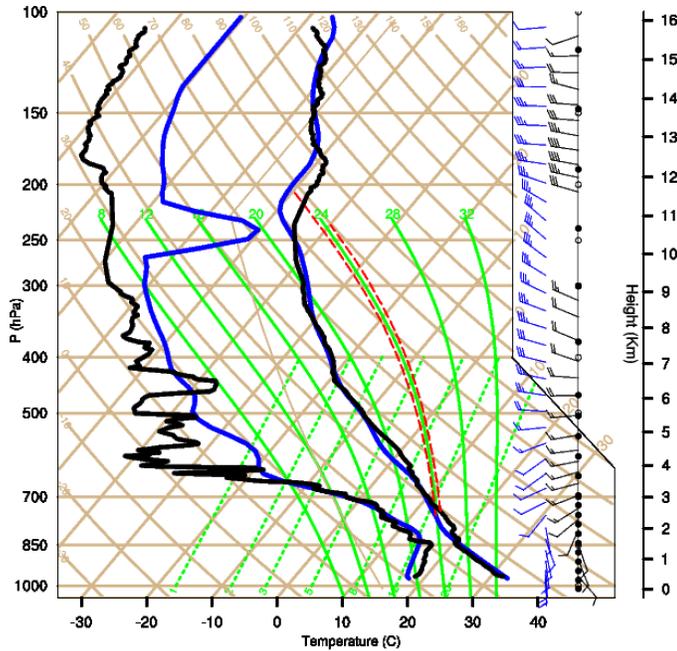
Figure 14. The observed (black) and model-simulated (blue) skew-t diagrams on 29-30 May 2012. The NSSL MGAUS was released from (35.854 °N, 98.066 °W) at 22:55 UTC. The WRF model-simulated upper air profile represents the one-hour offset in convection (23:50 UTC model time) at (35.86 °N, 97.70 °W). Wind speed is in m s^{-1}.

6.2 Hydrometeors

6.2.1 Proxy observations

Hydrometeors play a key role in the FRPSs that are tested in WRF, with 10 of the 18 schemes directly involving relationships between total lightning activity and hydrometeors and three schemes involving calculated radar reflectivity, which is dependent on the hydrometeors. Before the current damping and LDA techniques were applied, the model-simulated flash trends based on hydrometeors were overpredicting the observed total lightning. DiGangi (2014) investigated the hydrometeors in the Kingfisher storm for three specific times over a 40-minute period (00:00-00:40 UTC model time) using a diabatic Lagrangian analysis (DLA) approach. The DLA is constrained by the observed 4-dimensional radar winds and a simple cloud model (Ziegler, 2013a). Since the Kingfisher storm composed the southern portion of the severe convection analyzed in this case study, the DLA hydrometeor output are assumed to be a close approximation of

71

the actual hydrometeors. These proxy observations are provided at three to five altitude

levels ranging from 1.2 to 12.2 km for graupel/hail, 6.2 to 16.2 km for snow/ice, and 4.7

to 7.2 km for rain water and cloud water at each of three times. It is assumed that if WRF

closely captures the hydrometeors of the Kingfisher storm, then it is likely that the

northern section of the convective system will also be represented to the same degree.

Horizontal and vertical hydrometeor cross-sections through the WRF simulated

southern convection, prior to the current damping and LDA assumptions, were compared

against the DLA hydrometeor mixing ratios provided by DiGangi (2014). A comparison

of the maximum WRF and DLA hydrometeor concentrations averaged over all of the

available altitudes during the 40-minute period indicated that WRF overestimated the

maximum DLA graupel mixing ratios by roughly 25% and underestimated the snow/ice

by roughly 20%. Since WRF underestimates cloud water by less than 10%, it is

considered similar to the proxy observations below 7.2 km. Rain water, however, is

overestimated by ~70% below 7.2 km. Bela et al. (2016) compared the simulated

precipitation (rain and graupel) from their WRF-Chem run against the mean hourly

precipitation from the NCEP Stage IV analysis. The comparison suggested that although

there were differences in the precipitation distribution, the observed total precipitation

received at the surface was overestimated by < 20% in the northern convection from

23:40-00:40 UTC model time.

6.2.2 Ice hydrometeor thresholds

Initially the FRPSs requiring graupel and snow used mixing ratio thresholds of

1.0×10^{-12} g kg^{-1}. This was believed to be too low and a possible cause for the

overestimation by the hydrometeor-based FRPSs (not shown), as these thresholds would

potentially include grid cells outside the charging region (e.g., stratiform anvil precipitation region). The minimum graupel and snow mixing ratio thresholds were increased to 0.5 g kg^{-1} and 0.25 g kg^{-1}, respectively, to better represent the kinematic and microphysical processes related to charging in the convective core. Raising both thresholds helped to reduce the total flashes. For example, for the CSU GEV scheme, the estimated total flashes were reduced by ~20%. However, the LMA observations were still overestimated by the hydrometeor-based schemes.

Based on the results from Section 6.2.1, several attempts were made to reduce the graupel/hail and increase the snow within the convection by modifying the Morrison two-moment microphysics scheme. The threshold for converting snow to graupel/hail by riming was increased, which should decrease the amount of graupel/hail within the cloud (Hugh Morrison, personal communication, February 24, 2016). The results (not shown) indicate that increasing the snow threshold from 0.1 g kg^{-1} to 0.5 g kg^{-1} or 1.0 g kg^{-1} led to a 1-10% and 2-50% decrease in the model-simulated graupel/hail and snow/ice concentrations, respectively. Therefore, this modification did not significantly reduce the amount of graupel/hail present in the 29-30 May model-simulated storm and it also decreased the amount of snow when an increase was needed.

6.2.3 Scaling hydrometeor mixing ratios

The vertical cross sections of model hydrometeors from the WRF simulation with damping and LDA (Figure 15) also show the model-simulated graupel, snow, and ice do not extend over the same altitude ranges as indicated by the proxy observations. Rain water was not investigated in more detail because it was assumed to be precipitating and not contributing to the overestimation of the hydrometeor-based FRPSs. Therefore, a

closer inspection was taken of the WRF frozen hydrometeors' vertical distribution and compared with that from the DLA. The analysis suggests the graupel overestimation is primarily above 9 km altitude and the snow/ice underestimation mainly occurs between 11-13 km altitude. By focusing on these specific altitudes for the three times during the 40-minute period, instead of all altitudes, it was determined that WRF (1) overestimated graupel by roughly 55% above 9 km altitude and (2) overestimated snow/ice by 31% below 11 km altitude and underestimated snow/ice by 42% between 11-13 km altitude. Altitude-specific scaling factors for the hydrometeors were developed based on these percentage biases.

Figure 15 uses vertical cross sections through the approximate location of the Kingfisher storm in the southern portion of the WRF model-simulated convection to compare the graupel and snow/ice mixing ratios before and after the altitude specific scaling factors are applied to the hydrometeors in the WRF output. The results show the altitudes of maximum mixing ratio of the model-simulated graupel and snow/ice are more representative of the proxy observations after scaling is applied. For example, at 23:40 UTC observed time DiGangi (2014) indicated that above the freezing layer the maximum observed graupel/hail mixing ratio is ~9.0 g kg^{-1} between 8.2-8.7 km. Prior to scaling the WRF-simulated graupel/hail, the largest mixing ratios (9-10.8 g kg^{-1}) at the corresponding model time (00:20 UTC) are located between ~8.3-14.4 km (Figure 15a). After applying the scaling factors (Figure 15b) the maximum mixing ratios are similar (9-10.2 g kg^{-1}), but found over a smaller altitude range (~8.5-9 km) that is closer to the observed height. For the proxy observed snow/ice, the maximum mixing ratio (8-10 g kg^{-1}) is between 11.7-13.2 km (DiGangi, 2014). The maximum WRF-simulated

snow/ice mixing ratio increases from 3.1 g kg^{-1} between 11.3-12.5 km (Figure 15c) to

5.3 g kg^{-1} within a similar altitude range (11-13 km) after scaling (Figure 15d). While the

WRF-simulated snow/ice is still underestimating the proxy observations at this time and

vertical cross-section location, the horizontal distance covered by the simulated snow/ice

mixing ratios (1-5 g kg^{-1}) has slightly increased within this altitude layer.

With the application of the current damping and LDA assumptions, the location

and maximum mixing ratio of the model-simulated hydrometeors were adjusted closer to

the observations. These techniques did not correct the hydrometeors perfectly, so scaling

to the DLA proxy observations was required to improve the simulated hydrometeors for

our case study. However, some discrepancies still exist after scaling (i.e., graupel is

slightly overestimated and snow/ice is slightly underestimated). For use in the WRF

simulation, the altitude-specific scaling factors are only applied to the hydrometeors in

the FRPS code, not in the microphysics scheme.
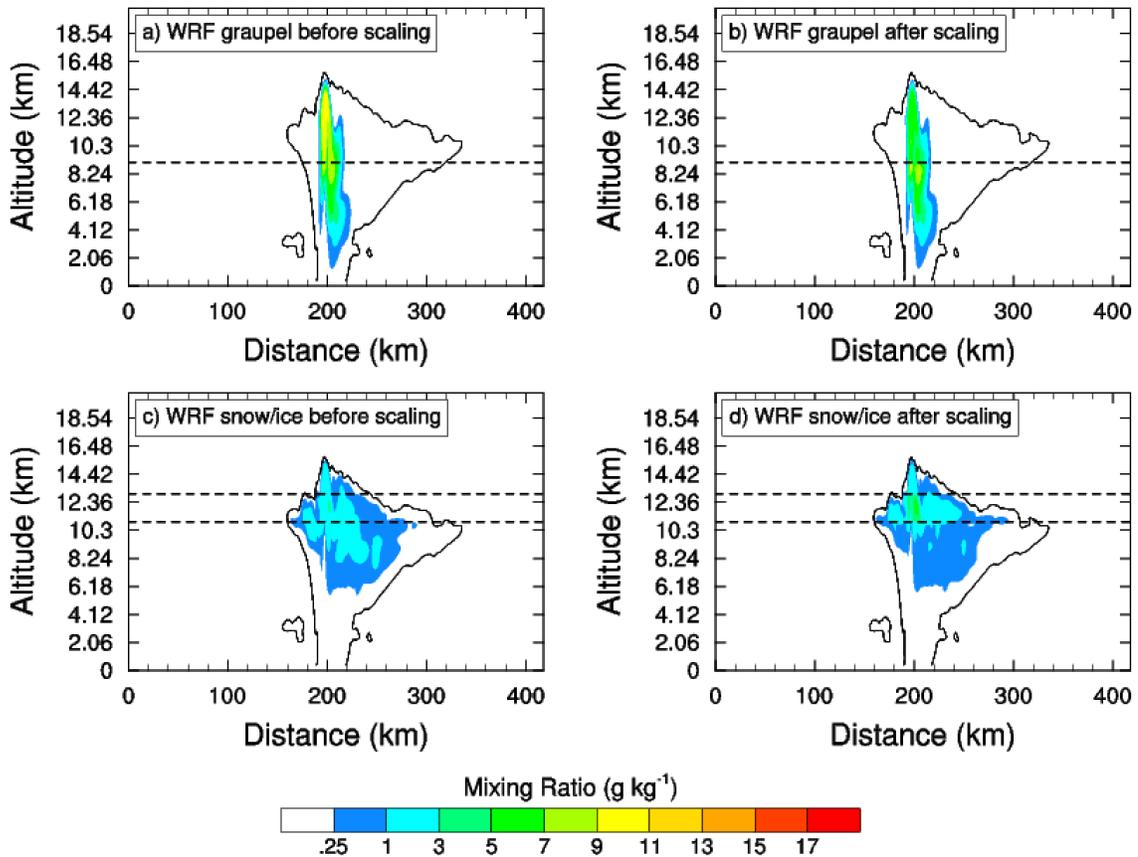
Figure 15. The WRF model-simulated graupel (top) and snow/ice (bottom) mixing ratios at 00:20 UTC model time before (a,c) and after (b,d) the altitude-specific scaling factors are applied to the hydrometeors in the FRPS code only. The solid black line represents the outline of the cloud, where total hydrometeors equal 0.01 g kg^{-1}. The dashed black lines indicate the specific altitudes where the scaling factors are applied. In the top figures, a graupel scaling factor is only applied above 9 km. In the bottom figures, a different snow/ice scaling factor is applied below 11 km and between 11-13 km.

6.3 Lightning Prediction

We examine the flash rate time series and total flashes predicted by the 18 FRPSs over the simulation period and compare them with the LMA observations. The lightning included in the analysis occurs within the bounding boxes that envelop and adjust to the simulated and observed convection every 10-minutes as the system matures. An example of the location of these boxes is provided in Figure 11. Figure 16 shows the observed and

model-simulated flash time series for the six schemes analyzed by Barthe et al. (2010).

These schemes are evaluated against the observations and each other starting at the

moment when reflectivity is first noted in the NEXRAD (21:10 UTC) and the model

(22:10 UTC). Since the storm simulation ends at 02:00 UTC model time, the primary

peak and downward trend in the flash rate time series cannot be compared with

observations for the final two hours of the storm system. As indicated by the reflectivity

analysis, the time evolution of the observed and model storms differ, which may affect

the flash rate comparisons. The number of total flash counts generated by each FRPS

before and after scaling the hydrometeors is provided in Table 10. This shows the

overestimation of the flash rates and total flashes persists for the five non-hydrometeor-

based schemes and 12 of the 13 hydrometeor-based schemes. The remainder of this

section presents the results from the WRF simulations with LDA, damping, and

hydrometeor scaling based on the proxy observations.
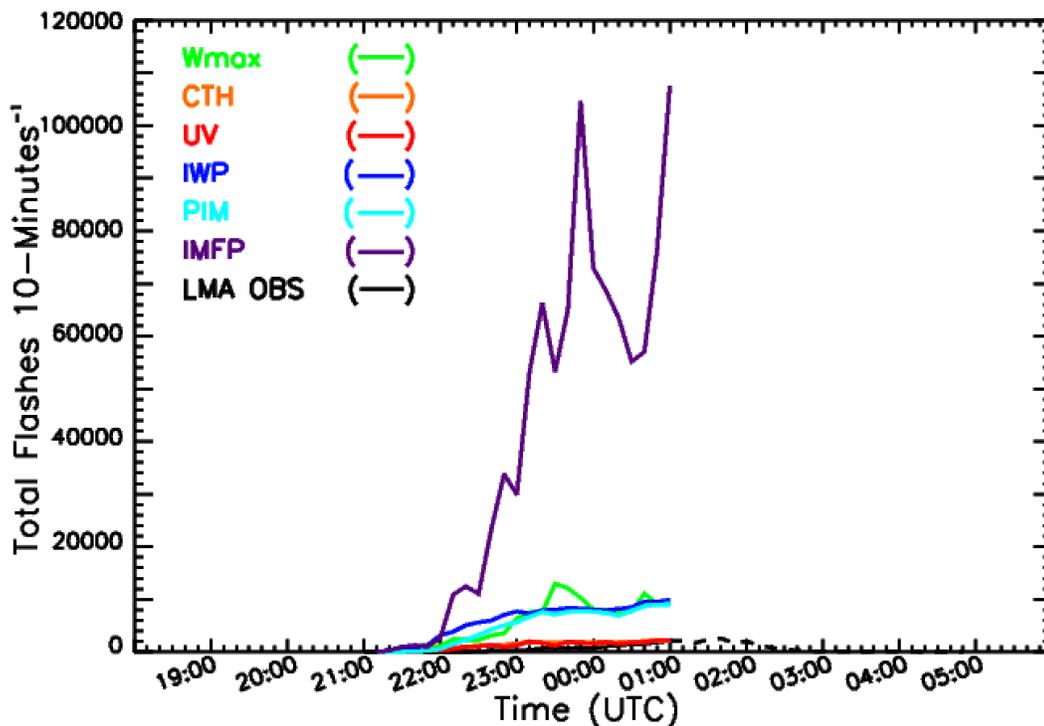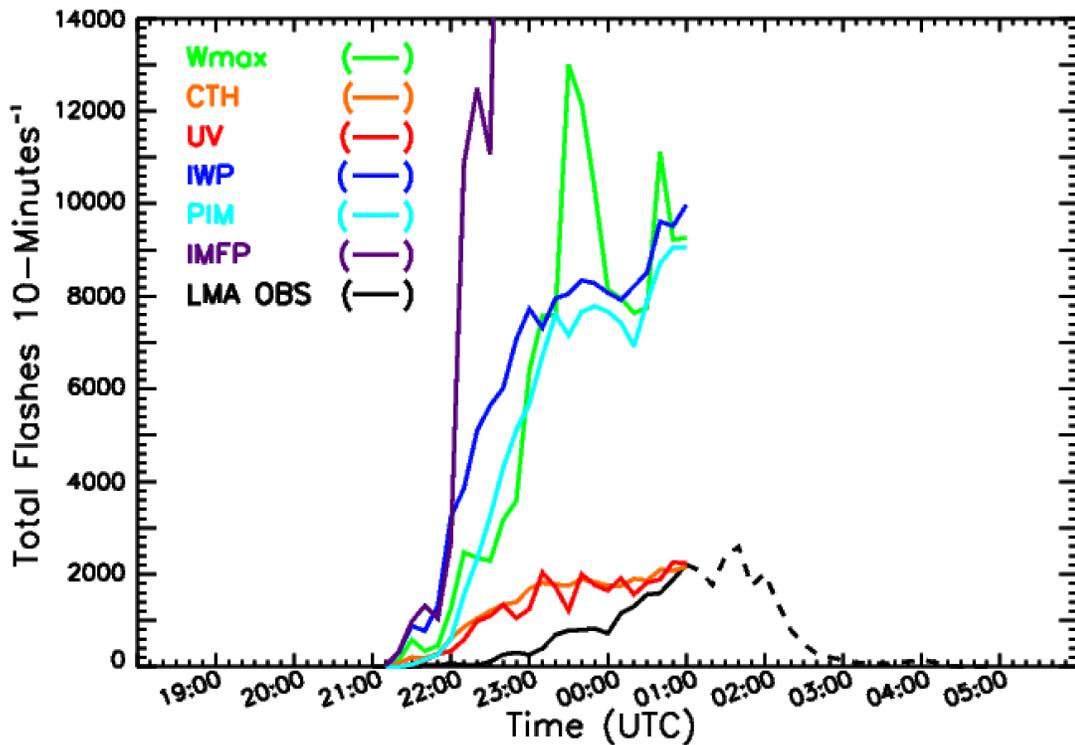
Figure 16. The total lightning flash rates per 10-minutes from the LMA (black) and the FRPSs based on relationships between total lightning activity and storm parameters from the literature. The top and bottom figures show the same data, except the y-axis on the top plot is expanded. The model-simulated lightning flash rates are based on a WRF run with damping/LDA techniques, and hydrometeor altitude specific scaling factors applied to the FRPS code only. The model-simulated lightning flash time series is adjusted 60 minutes earlier, so the observed (21:10 UTC) and model-simulated (22:10 UTC) storm initiation times coincide. The FRPSs represent the model-simulated trends from 22:10-02:00 UTC model time. The solid black line represents the observed lightning flashes from 21:10-01:00 UTC, which covers the same time period as the simulated flashes. The dashed black line represents the continuation of the observed time series after 01:00 UTC.

Table 10. Number of model-simulated total lightning flashes predicted from 22:10-02:00 UTC model time by the 18 flash rate parameterization schemes before and after the model-simulated hydrometeors are scaled within the schemes. Results are from simulations that include damping and LDA. The LMA observed 15,060 total lightning flashes from 21:10-01:00 UTC.

Flash Rate Parameterization Scheme	Model-Simulated Lightning Flashes		
	No Scaling	Scaling	Percent Change
w_{max}	134,870	134,791	-0.1%
CTH	31,264	31,547	+0.9%
UV	29,147	29,151	+0.0%
IWP	175,589	157,787 [+]	-10.1%
PIM	143,918	116,949	-18.7%
IMFP	1,087,677	971,504	-10.7%
CSU GEV	108,250	99,455	-8.1%
CSU 35EV	156,896	110,818	-29.4%
CSU PIM	192,513	116,908	-39.3%
UAH GEV10	102,534	99,853	-2.6%
UAH GEV5	95,302	93,138	-2.3%
UAH UV	16,096	16,089	-0.0%
UAH GEV10S	129,417	126,030	-2.6%
UAH GEV5S	126,109	123,246	-2.3%
UAH UVS	19,249	19,240	-0.0%
ICEFLUX	13,698	9,938 [*]	-27.5%
OK 35EV	24,783	23,488	-5.2%
LTG3	57,376	57,350	-0.1%

[+] When IWP is evaluated at 25 dBZ, the number of total lightning flashes is 143,743 (-18.1%).

[*] When ICEFLUX is evaluated at 390 hPa, the number of total lightning flashes is 14,419 (+5.3%).

Literature indicates that several FRPSs are sensitive to their application criteria. IWP involves a radar reflectivity threshold of 18 dBZ; however, if the model-simulated reflectivity produces higher values than observed, the threshold should be increased to better represent the IWP (Barthe et al., 2010). In a study by Mecikalski and Carey (2017) over northern Alabama for a supercellular system that produced 72,068 flashes, it was found that the peak of the LMA sources occurred between 7-9 km altitude and between

20-25 dBZ, although the majority of the sources from this system occurred between

4-13 km and between 15-55 dBZ. The LMA sources in our case study are generally

located between 6.5-11.5 km within the 20-55 dBZ reflectivity contours and maximize at

9.5 km between 25-30 dBZ (Figure 10). Therefore, the threshold used in the scheme is

increased to 25 dBZ to better represent the electrified portion of the storm and reduce the

overestimation. While this helps decrease the total flashes by 9% for this scheme (i.e.,

157,787 to 143,743 flashes), the overprediction is still a factor of 9.5, as indicated in

Table 10 and Figure 16.

Figures 17 through 19 show results from the 12 other FRPSs. Figure 17 focuses

on the three CSU-developed schemes (Basarab et al., 2015), the ICEFLUX scheme

(Finney et al., 2014), the LTG3 scheme (McCaul et al., 2009), and the scheme developed

with the 29-30 May data. Figure 18 displays results from the FRPSs developed by UAH

(Carey et al., 2015) and Figure 19 shows the flash rate time series for the six schemes that

provided the closest prediction of the number of flashes observed between 21:00-01:00

UTC observed time.
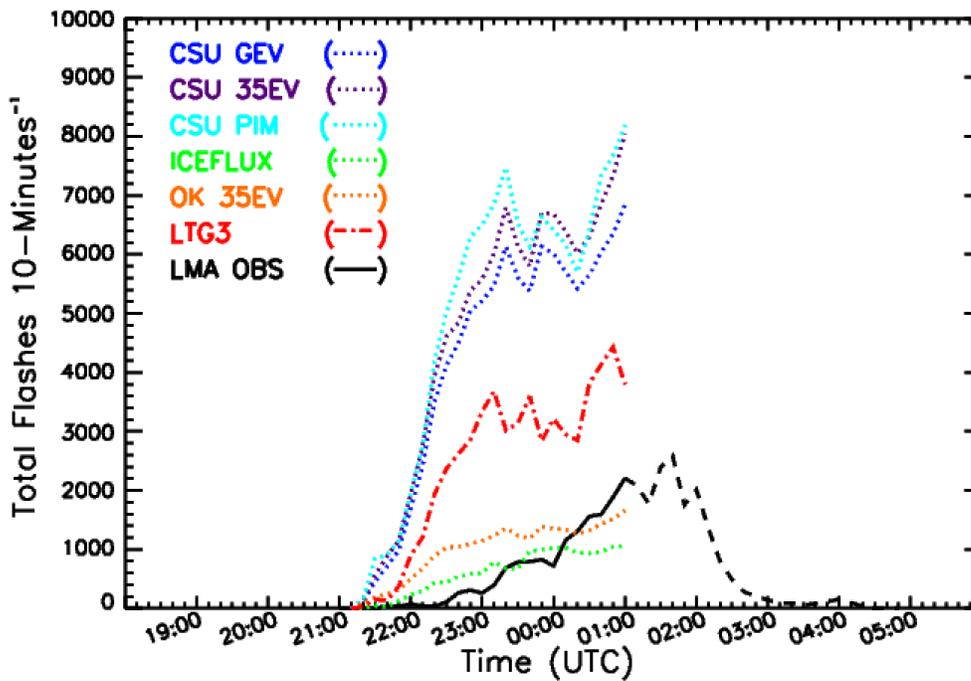
Figure 17. Same as Figure 16, except the FRPSs are based on relationships between total lightning activity and storm parameters developed by CSU (Basarab et al., 2015), Finney et al. (2014), and McCaul et al. (2009).
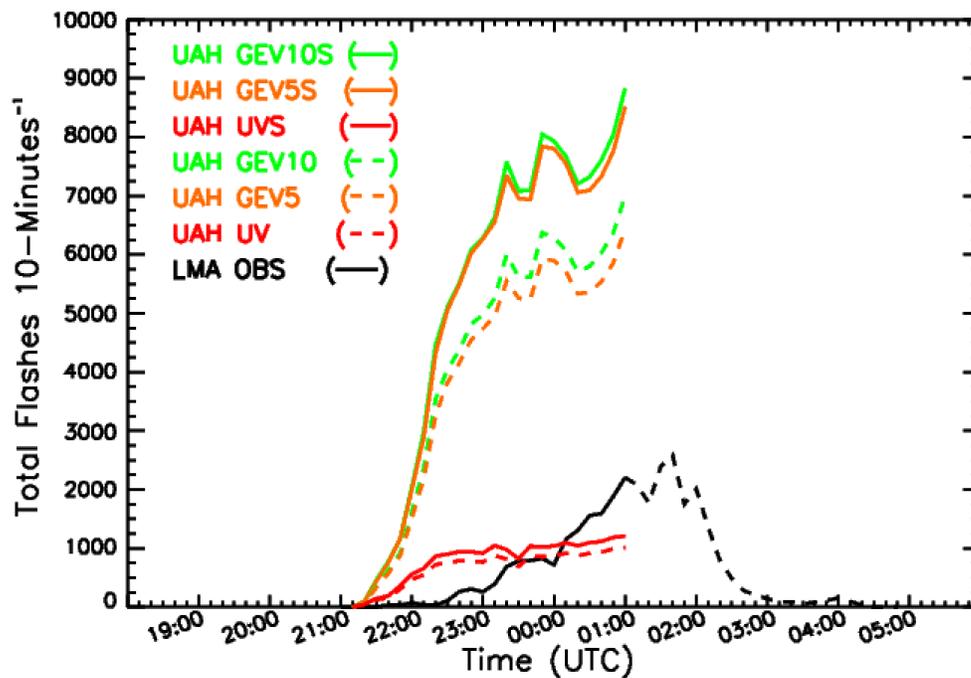
Figure 18. Same as Figure 16, except the FRPSs are based on relationships between total lightning activity and storm parameters developed by UAH (Carey et al., 2015).
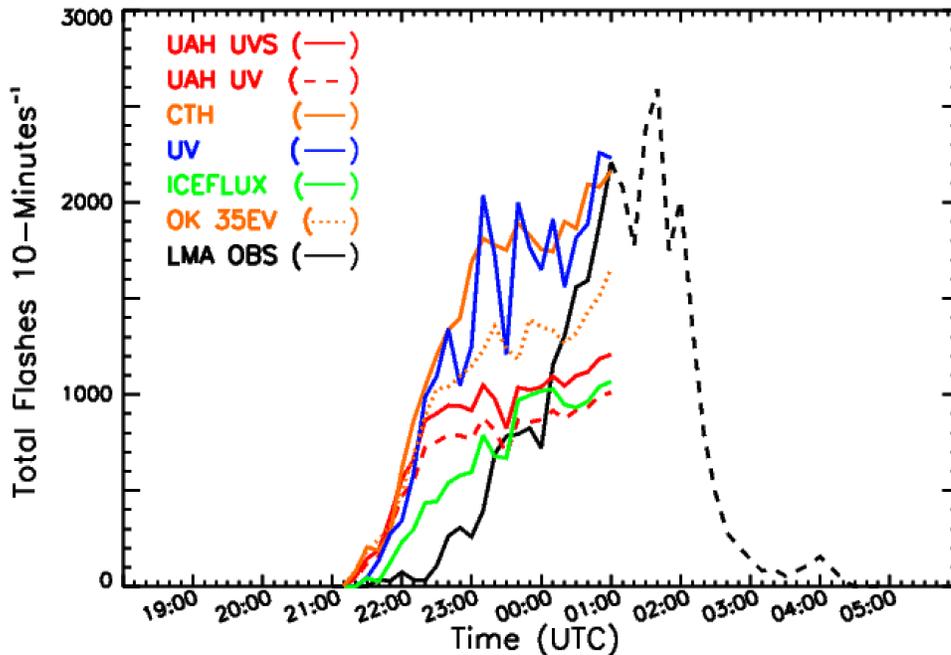
Figure 19. Same as Figure 16, except the FRPSs are based on relationships between total lightning activity and storm parameters with an overall total lightning flash count most similar to the central Oklahoma LMA observations.

ICEFLUX is sensitive to the pressure level the scheme is evaluated at (Finney et al., 2014), as well as which hydrometeors are classified as suspended ice crystals. Finney et al. (2014) developed this scheme using the specific cloud ice water content variable from the ERA-Interim reanalysis, which includes graupel, snow, and ice. To mimic this variable with WRF, the mixing ratios of the three hydrometeors were summed and only included graupel and snow if their fall speeds were less than the updraft velocity. Upon initial evaluation the results showed ICEFLUX overestimates the LMA total lightning flashes by roughly a factor of 4. However, if graupel is considered to be precipitating (i.e., not suspended), then ICEFLUX underestimates (9,938) the observations (15,060) (Table 10).

The 440 hPa pressure level used by ICEFLUX is the ISCCP cloud top pressure threshold for deep convective clouds (Rossow et al., 1996). However, 440 hPa is found at the very lowest location of cloud ice in our model-simulated storm. If we evaluate the scheme at 340 hPa, as tested by Finney et al. (2014), the underestimation becomes an overestimation (19,216). Therefore, a 100 hPa decrease in pressure (i.e., 440 hPa to 340 hPa) resulted in a 10,000 total flash increase. If the ICEFLUX pressure level is adjusted by 50 hPa (390 hPa) instead, then the total number of model-simulated flashes (14,419) is within ~4.5% of the observations (15,060), as shown in Figures 17 and 19.

On average the non-hydrometeor-based FRPSs overestimated the number of LMA total flashes by a factor of 3, while the hydrometeor-based schemes overpredicted by a factor of 10.7. IMFP has the largest difference between the model-simulated and observed total flashes (a factor of > 60). If the IMFP scheme is excluded, the observations are overestimated by a factor of 6.7 by the remaining hydrometeor-based schemes.

The total flash counts predicted by every FRPS increase earlier in the model-simulated storm than in the observed storm. The initial peak in the observed flashes (~100 flashes 10-min^{-1}; Figure 19) occurs 50 minutes after convective initiation, while seven of the 18 schemes (CTH, ICEFLUX, IMFP, IWP, CSU PIM, LTG3, and w_{max}) predict peaks of varying magnitudes (~50-1400 flashes 10-min^{-1}) roughly 20 minutes after the model storm develops.

An interesting feature that appears in most of the FRPS trends is a change in the steepness of the flash rate slope just after 22:00 UTC observed time (23:00 UTC model time). While the trends are generally steeper than the observations within the first few

hours of storm initiation, the model trend becomes slightly smaller after the first hour. In both UAH UV schemes, this change results in a slightly flatter slope than the other schemes that also exhibit this feature. The timing of this feature coincides with the end of the LDA and its modification of the water vapor in the atmosphere. For the w_{max}, IMFP, PIM, LTG3, and ICEFLUX schemes, this transition is not apparent in the trends. This suggests that the storm parameters used in these five FRPSs use variables and criteria thresholds that are not influenced by the LDA to the same degree as the other schemes.

The model-simulated flash rate time series for the IWP and PIM schemes have peaks that coincide with the observed peaks at 23:50 UTC and 01:00 UTC observed time (Figure 16). The four UAH GEV (Figure 18) and three CSU (GEV, 35EV, PIM) (Figure 17) schemes show multiple peaks between 23:00-00:00 UTC, instead of one like the observations and the IWP and PIM schemes; however, these schemes are similar because there is no prolonged increase in the flash rates during this time. The UV scheme hints at the presence of the peaks at 22:50 UTC and 23:50 UTC, although the trend is fluctuating at these times. The total lightning flashes per 10-min predicted by the CTH and UV schemes at 02:00 UTC model time is similar to the number of observed total flashes per 10-min at 01:00 UTC observed time. The LTG3 scheme is the only FRPS that clearly shows the presence of the observed peak at 01:00 UTC, although the UV scheme also hints at this feature. The two schemes that appear to replicate the timing and general shape of the observed peaks fairly well from 21:30-00:30 UTC, but not the magnitude, are those based on IMFP and w_{max}. ICEFLUX behaves similarly, but the peak at 22:50 UTC is not as distinct as it is in the observed, IMFP, and w_{max} flash rate trends, plus it

84

occurs ~30 minutes earlier. Generally, when the flash rate peaked in a scheme, the time offset from the observations was consistent with the storm evolution noted in the radar reflectivity.

Prior to this study a FRPS had not been developed for Oklahoma convection. Since 35EV was considered a robust storm parameter based on its performance in regions outside of Colorado, the FRPS was tailored for Oklahoma using observations from our 29-30 May case study. However, when the scheme was employed in WRF, the total number of observed lightning flashes was still overestimated (~56%; Table 10). Figures 17 and 19 also show the detailed features of the observed flash rate trend are missing, which is likely due to the high-bias in storm intensity during convective initiation. This is noticed by the large overestimation of the 35 dBZ echo volume (~500%) in the initial cells that develop at the start of the simulations both with and without LDA. After roughly 1-hr, the overprediction by the 35 dBZ echo volume becomes smaller (~30%) before turning into a slight underestimation (~15%). The increased intensity during the developing stage of the storm system may help explain why the predicted flash rates for this scheme, and others, lack some of the details seen in the observed flash rate trend (i.e., the observed peak at 22:50 UTC).

An additional technique used the mean bias between the observed and model-simulated flash data per 10-min to evaluate the performance of the FRPSs. The schemes were ranked based on their root mean square error after the mean bias between the observed and simulated flashes was removed (i.e., centered root mean square error) and based on their mean bias (Table 11). For this case study, both calculations identified the same six FRPSs (i.e., ICEFLUX, OK 35EV, UV schemes and CTH) in Table 11 as being

the best at predicting flash rate fluctuations and total flashes over the life of the convection, and selected the same lowest ranked scheme (i.e., IMFP).

In terms of biases and the total flashes predicted over the simulation, the best performing FRPSs (Figure 19) include ICEFLUX (which very slightly underestimates the LMA total lightning flashes), the three UV schemes developed by Deierling et al. (2008) and UAH (Carey et al., 2015) (i.e., all convection types and supercell-only in northern Alabama), the OK 35EV scheme, and the CTH scheme. Of all the schemes not involving hydrometeors, the UAH UV scheme performed the best. Overall, ICEFLUX is the FRPS that best represents the total number of lightning flashes and their fluctuations. The individual 10-min flash rates from this scheme were also the closest to the observed rates for almost the entire simulation. Figure 20 displays the location of each model-simulated total lightning flash generated by the ICEFLUX scheme as the system tracked southeast. This track is similar to the observed flashes in Figure 5 and both the observed and simulated flashes appear to cover a similar area from 21:10-01:00 UTC. While the observed convection shows a higher density of flashes along its southwest side, the simulated storm system shows more flashes located on its northeast side. Three distinct paths are also visible in Figure 20, which is likely due to the larger areas of higher reflectivity that are present later in the simulated storm's lifecycle.

Table 11. Centered root mean square error of the model-simulated total lightning flashes per 10-min (left) and mean bias in the model-simulated total lightning flashes per 10-min (right) predicted from 22:10-02:00 UTC model time. The LMA flashes used in the calculation are from 21:10-01:00 UTC observed time.

Flash Rate Parameterization Scheme	Centered Root Mean Square Error (flashes)	Flash Rate Parameterization Scheme	Mean Bias (flashes)
ICEFLUX	411	ICEFLUX	-27
OK 35EV	426	UAH UV	43
UV	458	UAH UVS	174
CTH	460	OK 35EV	351
UAH UVS	484	UV	587
UAH UV	500	CTH	687
LTG3	1,019	LTG3	1,762
UAH GEV5	1,731	UAH GEV5	3,253
CSU GEV	1,835	CSU GEV	3,516
UAH GEV10	1,881	UAH GEV10	3,533
CSU 35EV	2,061	CSU 35EV	3,990
CSU PIM	2,208	CSU PIM	4,244
UAH GEV5S	2,418	PIM	4,245
UAH GEV10S	2,483	UAH GEV5S	4,508
IWP	2,750	UAH GEV10S	4,624
PIM	2,846	w_{max}	4,989
w_{max}	3,728	IWP	5,362
IMFP	33,494	IMFP	39,852
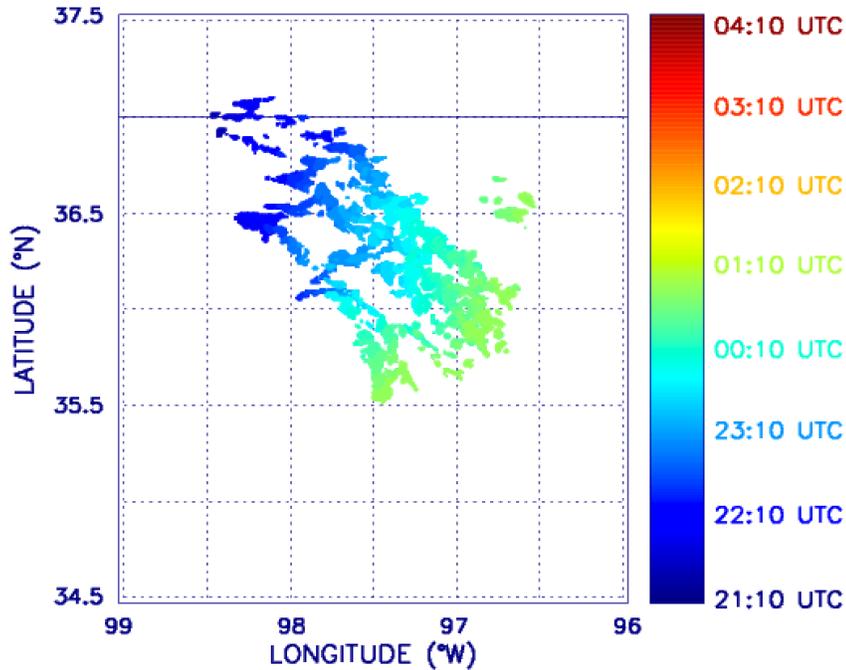
Figure 20. Location of the model-simulated total lightning flashes (≥ 0.5 total flash) predicted by the ICEFLUX FRPS. For comparison with the LMA total lightning, the convective initiation of the model-simulated storm (22:10 UTC) is adjusted 60 minutes earlier to coincide with the start of the NEXRAD observed storm (21:10 UTC). The time scale is color coded from 21:10 UTC on 29 May to 04:10 UTC on 30 May 2012.

However, when the model-simulated flash rates are not adjusted an hour earlier to coincide with the start time of the observed storm, then the initial trend in the model flash rate time series appears to better represent the increasing trend and variation in the LMA observations. This suggests the rapid intensification of the model storm may offset the delay in convective initiation. Figure 21 shows how the top six FRPSs, previously discussed, compare against the LMA observations with the modification to timing. The FRPS performance was also evaluated in terms of bias using the observed and model flashes from 22:10-01:00 UTC observed time. Table 12 indicates the same six FRPS, as previously suggested by the 1-hour offset, as being the best at predicting flash rate fluctuations and total flashes over the ~3-hour interval. However, the order of schemes is

slightly different, with the OK 35EV scheme having the smallest mean bias with respect to the number of flashes observed during the ~3-hour period. This scheme, which was developed using data from the 29-30 May convective event, appears to represent the observed flashes from 22:10-01:00 UTC slightly better than when the model flashes were adjusted an hour earlier (Figure 19). Very little difference was noted in the centered root mean square error among the top four schemes (OK 35EV, CTH, ICEFLUX, and UV). From a LNO$_x$ chemistry perspective, it is important to properly simulate the total number of flashes, in addition to their variation. For this reason, the ICEFLUX scheme was selected as the most appropriate scheme given the delay in the model storm's initiation and the fact that it best predicted the total number of flashes from 21:10-01:00 UTC when the aircraft were sampling the convective outflow (i.e., trace gas measurements).
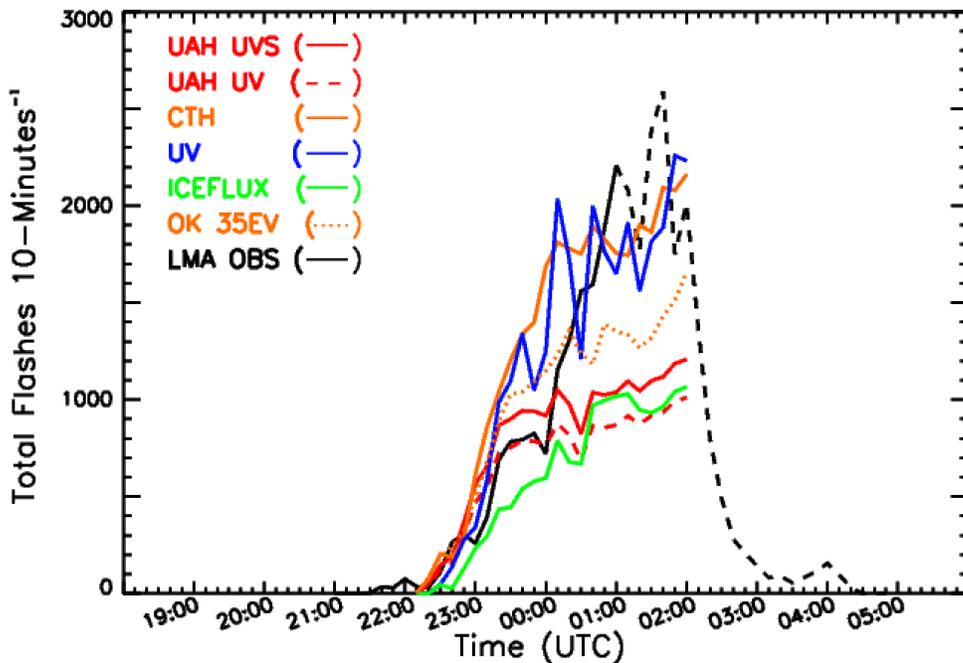
Figure 21. Same as Figure 19, except the model-simulated flashes are not adjusted 60 minutes earlier to coincide with the observed storm initiation at 21:10 UTC. The FRPSs represent the model-simulated trends from 22:10-02:00 UTC model time.

Table 12. Centered root mean square error of the model-simulated total lightning flashes per 10-min (left) and mean bias in the model-simulated total lightning flashes per 10-min (right) predicted from 22:10-01:00 UTC model time. The LMA flashes used in the calculation are from 22:10-01:00 UTC observed time.

Flash Rate Parameterization Scheme	Centered Root Mean Square Error (flashes)	Flash Rate Parameterization Scheme	Mean Bias (flashes)
OK 35EV	327	OK 35EV	3
CTH	337	UAH UVS	-135
ICEFLUX	344	UV	143
UV	350	UAH UV	-248
UAH UVS	423	CTH	266
UAH UV	449	ICEFLUX	-360
LTG3	904	LTG3	1,137
UAH GEV5	1,615	UAH GEV5	2,443
CSU GEV	1,748	UAH GEV10	2,664
UAH GEV10	1,758	CSU GEV	2,696
CSU 35EV	1,931	PIM	2,943
CSU PIM	2,165	CSU 35EV	3,054
UAH GEV5S	2,315	CSU PIM	3,362
UAH GEV10S	2,365	UAH GEV5S	3,501
PIM	2,579	UAH GEV10S	3,580
IWP	2,586	w_{max}	3,717
w_{max}	3,733	IWP	4,171
IMFP	31,166	IMFP	29,365

6.4 Flash rate parameterization scheme discussion

The 29-30 May 2012 severe supercell system was reproduced fairly well by WRF regarding its area, height, and vertical motion, as well as the instability of the storm environment. However, the majority of the FRPSs overpredicted the total flashes even after adjusting the model-simulated hydrometeors to bring them closer to the proxy observations. Here we explore why the FRPSs succeeded and failed in reproducing features in the observed flash rate trends, as well as how the results compare against the performance of FRPSs in other cloud-resolved simulations.

6.4.1 Ice-phase hydrometeors

Hydrometeors from observed radar data are determined by a very different method than those derived from model output. Thirteen of the 18 FRPSs involve relationships between total lightning activity and hydrometeors themselves or via radar reflectivity. Fuzzy logic algorithms were used to derive hydrometeor types from polarimetric radar for eight of these 13 (i.e., PIM, IMFP, CSU PIM and GEV, and four UAH GEV). The fuzzy logic algorithms developed by Dolan et al. (2013) and Vivekanandan et al. (1999) contain 10 and 14 hydrometeor categories, respectively, while the microphysics schemes available in WRF have about half that number available. Both bulk and bin microphysics parameterization scheme options are provided in WRF. The bulk schemes, in addition to many of the bin schemes, separate ice particles into predefined categories (e.g., cloud ice, snow, graupel, and hail) and the particle size distributions vary slightly between schemes. The disadvantage of having multiple ice categories is that this distinct separation is not natural. Instead there should be a gradual transition between the different ice types (Morrison and Grabowski, 2008; Morrison et al., 2015).

The differences between how observed and model-simulated hydrometeors are defined and determined could explain why the observed lightning is overestimated. For our case study we defined dense precipitating ice as hail in the Morrison two-moment microphysics scheme as this is more appropriate for continental deep convection. This means hail was used when a FRPS indicated the use of graupel. The CSU GEV schemes (Basarab et al., 2015) include both low- and high-density graupel categories, while the UAH GEV (Carey et al., 2015) calculations only used grid boxes where the graupel/small hail category dominated. The difference in the number of hydrometeor categories and

how specific hydrometeors are applied highlights a potential issue when calculating

hydrometeor-based storm parameters.

The PIM and IMFP FRPSs (Deierling, 2006; Deierling et al., 2008) were

developed using thunderstorms in Colorado, Kansas, and northern Alabama. The

observed 1-min LMA data from our 29-30 May case study were used to back calculate

the PIM and IMFP parameters from their respective FRPS equations. The calculation

indicated that we should expect the PIM and IMFP values to be within the range with

which these schemes were developed based on the High Plains and Alabama convection.

However, when the flash rates are calculated online in WRF, the IMFP and PIM greatly

overestimate the observed total lightning flashes. While IMFP produced the greatest

overprediction of the 18 FRPSs, as indicated by the large bias in total flashes and

fluctuations (Table 11), this scheme does reproduce flash rate trends similar to the 29-30

May observations. Barthe et al. (2010) also found that IMFP was able to recreate the

trends of the observed total lightning flash rate time series, especially for a severe versus

airmass thunderstorm, but was unable to reproduce the magnitude and produced the

largest overestimation of the schemes tested. The severe storm simulated by Barthe et al.

(2010) also produced similar features in the flash rate time series predicted by PIM and

overestimated their magnitudes, which is similar to our severe system. The uncertainty

with IMFP and PIM may also be related to assumptions made within a microphysics

scheme, which may generate errors when calculating ice mass (Barthe et al., 2010).

IMFP and PIM are plausible schemes because they are based on storm characteristics

involved with cloud electrification; however, they appear to be very dependent on the

proper prediction of variables within model-simulated storms.

FRPSs may instead benefit from total lightning activity and storm parameter relationships that avoid using specific ice hydrometeors (e.g., graupel). The transition between ice types is not gradual in microphysics schemes that offer multiple ice-phase categories, such as the Morrison two-moment. This characteristic may not be appropriate when trying to generate lightning with a FRPS that involves specific ice categories. A solution may be to use a scheme based on a single ice-phase category, such as the predicted particle properties (P3) scheme (Morrison et al., 2015). This scheme predicts mass and number mixing ratios of rain and cloud water, as well as four ice mixing ratio variables (i.e., total ice mass, rime ice mass, rime volume, and total number). One of the advantages of the P3 scheme is its ability to allow for smooth transitions as ice particles grow. A final version of this scheme was not available to test at the time of this analysis.

6.4.2 Development and application environments for FRPSs

The three FRPSs (CSU PIM, 35EV, and GEV) developed using isolated Colorado thunderstorms (Basarab et al., 2015) overestimated the total number of LMA flashes in the 29-30 May simulated storms. Generally, Colorado storms have higher flash rates than Oklahoma thunderstorms, which is likely due to the shallower warm cloud depths of Colorado convection (Fuchs et al., 2015). The CSU 35EV scheme was considered the most robust of the three schemes because it performed well in other areas (i.e., Oklahoma, northern Alabama, and Washington, D.C.), but the 29-30 May Oklahoma storms had deep warm cloud depth (2.5 km) and developed in an environment with extreme NCAPE (0.37 m s^{-2}) and high vertical wind shear (24 m s^{-1}). According to Basarab et al. (2015), this convective environment does not lend itself to a successful application of the CSU 35EV scheme because the observed storm developed in an

environment that did not maximize the performance of the FRPS. In addition, the cell-tracking algorithm used by CSU identified a cell as convective if the areas covered by two reflectivity thresholds (i.e., 35 dBZ and 45 dBZ) each exceeded a specified threshold (Basarab et al., 2015; Fuchs et al., 2015). In our cloud-resolved application of the CSU FRPSs, it was assumed the 35 dBZ criteria with no area threshold would be sufficient to differentiate between convective and stratiform regions in the model-simulated storms. However, it is possible the simulated storm region > 35 dBZ included non-convective areas, especially since the model cells were not as individualized as the observations.

The four UAH GEV schemes that are based on northern Alabama thunderstorms (Carey et al., 2015) all overestimated the observed 29-30 May Oklahoma total flash rates. However, the UAH UV scheme, which is applied between -10 °C and -40 °C where $w > 5$ m s^{-1}, only overestimated the observed flashes by 6.7%. This was the best performing non-hydrometeor scheme. This suggests that using a FRPS based on the criteria relevant to cloud electrification (i.e., temperature and vertical velocity) may be most appropriate for predicting flash rates if the model has difficulty simulating the hydrometeors. When supercell-only versions of the schemes are used, the overprediction is roughly 30% larger than when the versions using all convection types are considered, even though the May 29-30 system consisted of supercells.

The three CSU schemes and the four UAH GEV schemes represent linear relationships with total lightning activity. However, the flash rates observed over the lifetime of our 29-30 May Oklahoma case study (max=312 flashes min^{-1}; mean=75.5 flashes min^{-1}) are higher than the flash rates observed in the northern Alabama (max=102 flashes min^{-1}; mean=12.5 flashes min^{-1}) and Colorado

94

(max=287.8 flashes min^{-1}; mean=53.9 flashes min^{-1}) thunderstorm datasets, which were used to develop their respective FRPSs. This suggests the coefficients associated with these schemes may not be appropriate for the Oklahoma region or our 29-30 May event. For example, Basarab (2015) evaluated the same Alabama thunderstorm (18 May 2012) as Carey et al. (2014) using similar FRPSs (e.g., GEV). The schemes developed using Colorado storms had different coefficients than those based on Alabama convection and therefore did not predict the observed flash rates and trends as well. This suggests that FRPSs may not be applicable for use on storms outside of the region used to develop the scheme.

The LTG3 scheme developed by McCaul et al. (2009) has only been implemented in models with horizontal resolutions of 2-4 km and with microphysics and PBL schemes other than the combination that our case study employed. While the flash rates do not increase as quickly after convective initiation as some of the other FRPSs predict, the trend does become steeper after roughly 40 minutes and overestimates the observations by a factor of 3.8. It is possible that using the LTG3 scheme at a 1 km horizontal resolution with 89 vertical levels is too fine and is resolving additional storm features as the system matures. The production of stronger vertical velocities than would occur at 2-4 km resolution is one possibility, which would lead to an overestimation of flashes; however, the maximum updraft speed generated during the simulation is within 5% of the observations, although located at a slightly higher altitude. It is also possible our combination of the Morrison two-moment microphysics and YSU PBL schemes, which has not been previously used to evaluate LTG3, requires this FRPS to be recalibrated. Initial tests of the Morrison two-moment microphysics and MYJ PBL schemes have

indicated that graupel production is overly strong (Eugene McCaul, personal communication, January 13, 2017).

6.4.3 Non-linear FRPSs

The majority of the FRPSs are built using data from individual storms. This includes CTH and w_{max}, which were designed to represent a storm with one maximum value; however, these non-linear FRPS equations are applied per model processor in WRF. While the non-linear schemes (i.e., CTH and wmax) are generally applied in the manner they were intended (i.e., storm height is similar to the width of the processor), CTH roughly doubles the LMA observations and w_{max} overpredicts by a factor of 4 larger than CTH. For our case study, each processor covering the model domain is roughly 18 km × 19 km in area, which is slightly smaller than the horizontal dimension of the 29-30 May observed and simulated supercells. The width of the processors is only ~13-19% larger than the maximum model-simulated storm height (~16 km). Even if a storm were smaller than a processor, the cell would eventually span multiple tiles unless it remained stationary and near the processor's center. This means additional total lightning flashes are generated by the non-linear schemes when the cell spans more than one processor.

The w_{max} FRPS was built using two non-linear schemes (Price and Rind, 1992), where the slightly non-linear relation between w_{max} and CTH is incorporated into the fifth-power relationship between CTH and flash rate. While the non-linearity of w_{max} may not pose a problem when it is applied to a single area that envelops the convection of interest, any errors may be exacerbated when the non-linear scheme is applied to a cell spanning multiple processors. Barthe et al. (2010) suggested w_{max} works better for severe

than for weak thunderstorms; however, they point out that w_{max} is dependent on the simulation's horizontal resolution.

Barthe et al. (2010) simulated lightning flash rates for a severe storm and an airmass thunderstorm using WRF output. The results suggested that when an adjustment factor was applied to the storm parameter, CTH performed better for the airmass thunderstorm, while w_{max} predicted the flash rate well for the severe storm. Wong et al. (2013) also discussed the need for a "calibration factor" due to the resolution dependency of the Price and Rind (1992) CTH scheme. Allen and Pickering (2002) did not favor the CTH scheme because the fifth-power in the FRPS equation causes the scheme to be very sensitive to any biases in the CTH of model-simulated continental convection. Giannaros et al. (2016) also suggest CTH is a poor proxy for the intensity of convection and lightning activity and that tuning is almost always necessary when implementing parameterizations similar to Price and Rind (1992). In a study by Giannaros et al. (2015), when a masking filter was used in conjunction with CTH and a convective parameterization in WRF, more realistic lightning predictions were possible for 10 different convective events observed in Greece. The masking filter only applied the CTH scheme when specific total ice content, w_{max}, and CAPE thresholds were met.

Further investigation of the sensitivity of the non-linear, and linear, schemes to the number of model processors and resolution would require additional model runs at coarser resolutions. Initial analysis with the instantaneous model output every 10 min indicates a negligible change in the flash counts generated by the linear FRPSs without a y-intercept as resolution is increased to 2 km and 4 km; however, the UV FRPS, which is a linear scheme with a negative y-intercept, indicates a factor of 5 and factor of 60

decrease in the simulated flash counts as the resolution is modified. Barthe et al. (2010) found the flash rates predicted by a FRPS (i.e., w_{max}, CTH, UV, IWP PIM, and IMFP) were similar for a severe storm at model resolutions of 500 m, 1 km, and 2 km, and for an airmass thunderstorm at 1 km and 3 km resolution.

6.4.4 Vertical velocity

The four FRPSs that produced flash counts within a factor of 2 of the observations were based on UV (Deierling, 2006; Deierling et al., 2008; Carey et al., 2015) and ICEFLUX (Finney et al., 2014). Unlike the other FRPSs, the UV schemes have a specific vertical velocity criterion applied within the mixed-phased region. Other schemes are more complex, since they require additional criteria within the mixed-phase region, such as reflectivity and/or hydrometeors (see Table 2). Using a vertical motion threshold may help the model focus on the charged portion of the convective cloud, since updrafts play an important role in supplying water vapor for particle growth, ice particle collisions, and charge separation. In the model simulations prior to and with the current damping and LDA methods, all of the UV schemes were considered to be among the best performing schemes. Of the non-hydrometeor-based schemes, the UAH UV scheme represented the number of total flashes and almost the entire flash rate time series fairly well.

While the ICEFLUX scheme is more complex because it involves several frozen hydrometeors and their fall speeds, it is only evaluating these criteria at a specific pressure level. This scheme is related to the IMFP because it focuses on the intensity of the flux of nonprecipitation ice particles, not just the mass. The ICEFLUX scheme does the best at reproducing the total number of lightning flashes for our 29-30 May case. It also generates a similar trend as the observations; however, the increase of the flash rate

is steeper than the initial observations, which causes the more detailed shape of the observed peaks to not be well replicated. This scheme is also similar to the upward convective mass flux scheme, which Allen and Pickering (2002) determined was able to generate flash rates fairly well at most locations. Based on its performance in our case study and its inclusion of both vertical motion and ice particles, which are equally important for cloud electrification, we suggest the ICEFLUX scheme has promise for future use at cloud-resolved scales.

CHAPTER 7: LIGHTNING-GENERATED NITROGEN OXIDES PRODUCTION

One of the objectives of this work is to estimate the mean LNO_x production per flash in

an observed DC3 storm using a combination of a cloud-resolved WRF-Chem simulation

and observations. Ten WRF-Chem simulations were evaluated using the FRPS based on

ICEFLUX. The simulations included one run with no lightning chemistry and nine runs

with different LNO_x production scenarios. Prior WRF-Chem cloud-resolved simulations

of the 29-30 May case study used the default model parameters for the fractional CG and

IC flash channel vertical profiles (DeCaria et al., 2000) and the IC:CG ratio (Boccippio et

al., 2001) with the w_{max} FRPS with a 0.106 adjustment factor (Bela et al., 2016) and the

UAH UVS scheme with no adjustment factor (Cummings et al., 2016). Both analyses

tentatively suggested an LNO_x production scenario of 125 moles flash^{-1}. However,

observations of the vertical distributions of CG and IC flash channels and of the IC:CG

ratio are available for the 29-30 May storm. I modified the model to allow use of these

data. Therefore, the current analysis first tests the performance of the use of these

observations through four different combinations of the default and observed vertical

distributions of lightning flash channel lengths and IC:CG ratios.

The five subsequent simulations were used to determine if the LNO_x production

needed adjustment based on comparisons with the DC3 aircraft observations. These

WRF-Chem runs only used the observed flash channel length vertical distributions and

time evolving observed IC:CG ratios. The previously suggested 500 moles per CG and

IC flash (Ott et al., 2010) scenario was tested, along with the 604 moles per CG flash and

38 moles per IC flash from the Koshak (2014) LNOM scenario. The LNOM scenario

yields a mean 151 moles flash^{-1} using the 29-30 May observed mean IC:CG ratio of about four. Pollack et al. (2016) concluded 107 moles flash^{-1} was appropriate for the 29-30 May case using a volume-based method to analyze DC3 aircraft measurements, and this scenario was tested in the model. A comparison of the model with 107 moles flash^{-1} and aircraft NO$_x$ mixing ratios suggested the LNO$_x$ production scenario should be adjusted to 82 moles flash^{-1} to achieve a best match with observations. When the LNOM scenario (Koshak, 2014) is adjusted to use 82 moles flash^{-1} as its mean value, but maintain the same ratio of NO production per CG flash and per IC flash, it suggests CG=328 moles flash^{-1} and IC=21 moles flash^{-1}.

Section 7.1 discusses the differences in the mixing ratios of the tracer species in the anvil outflow for the various simulations. Section 7.2 examines the variation in the anvil outflow NO$_x$ mixing ratios among the nine different LNO$_x$ production scenarios, with a focus on the scenario that best represents the aircraft observations. The relationships between lightning characteristics and LNO$_x$ production is discussed in Section 7.3 and the variation in simulated flash rate time series among the LNO$_x$ production scenarios is investigated in Section 7.4.

7.1 Tracer species

The anvil outflow was sampled by the DC8 between 10.72-11.21 km from 23:48:30-23:58:30 UTC and by the GV between 11.71-12.20 km from 23:59:30-00:23:30 UTC. Each altitude interval corresponds to two model layers. The GV and DC8 anvil outflow sampling periods, defined by Fried et al. (2016), were divided into 10-min intervals to correspond with the 10-min model output. Data points must be within anvil cloud outflow (total hydrometeors > 0.01 g kg^{-1}) and within tropospheric air (O$_3$:CO ratio

< 1.25; Hudman et al., 2007) to be included. Since the observed and simulated anvil clouds were of similar area, outflow sampling boxes of comparable size were identified in the model-simulated convection. The box locations were adjusted in the horizontal plane to represent a similar distance from the center of the observed high composite reflectivity, as well as a region with similar features as the observed convection. The only exception was the DC8 outflow box from 23:50-00:00 UTC. The southwest portion of the flight track was located between 10.97-11.21 km and the northern half was between 10.72-10.97 km. In this lower layer the model-simulated wind speed was slightly weaker and the LNO_x plume was thicker than observed; therefore, this layer was shifted farther east in the model than the observations. Increasing the distance of the lower layer from the model-simulated convective core during this time interval placed the northern portion of the outflow box in a region of the anvil that is more representative of the observed anvil environment.

A direct comparison of the aircraft observed and model-simulated CO and O_3 mixing ratios within the same layers indicate the convective transport from the boundary layer is slightly underestimated in the model (Figure 22a and 22b). One model layer (i.e., 0.25 km) beneath each layer the aircraft flew at (i.e., 10.48-10.72 km, 10.72-10.97 km, 11.46-11.71 km, and 11.71-11.95 km) provides a better match to the observations (Figure 22c and 22d). Using these layers as a correction for the underestimated vertical transport, the overall mean model-simulated mixing ratios from these four model layers are within 1% and 3% of the aircraft observed CO (118.7 ppbv) and O_3 (86.1 ppbv), respectively (Table 13). This is true for each of the WRF-Chem simulations run with and without lightning chemistry.

102
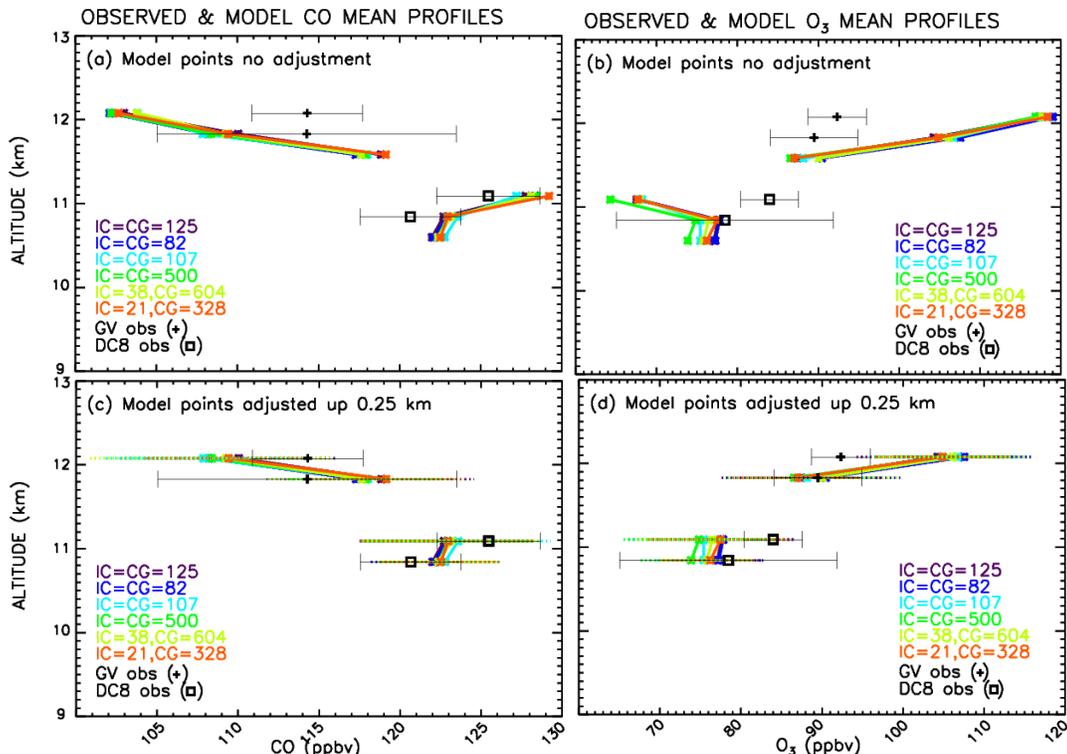
Figure 22. Aircraft observed and model-simulated mean (a) CO and (b) O_3 mixing ratios within the same layers. Model-simulated mean (c) CO and (d) O_3 mixing ratios moved up 0.25 km. The ±1 standard deviation is represented by solid black lines for the observations and dotted color lines for the model.

Horizontal cross-sections of the model-simulated convection suggest that lower CO and higher O_3 mixing ratios are transported downward around the rear anvil (Figures 23 and 24). During DC3 research aircraft encountered O_3-rich stratospheric air wrapped around the cloud edge of the MCS observed on 30 May 2012 (Pan et al., 2014; Huntrieser et al., 2016). Pan et al. (2014) also simulated this "ram's horn" shape using the WRF model at cloud-resolved resolution. In addition, Li et al. (2017, in review) simulated the vertical flux divergence in three additional DC3 convective events using WRF-Chem at different spatial scales, including our 29-30 May case study, and captured a similar O_3 enhancement 2-3 km below the tropopause.

Vertical cross-sections show model-simulated boundary layer CO (> 130 ppbv) and O_3 (< 65 ppbv) are present in the convective updrafts (Figures 23 and 24). A layer of

higher CO mixing ratios (> 120 ppbv) also exists at ~10.5 km, as well as within the

anvils. Minima in O_3 mixing ratios are visible in the anvil for over several hours in the 5-

hour simulation. Above 10.8 km within the convective system, the mean O_3 mixing ratio

decreased by greater than 40 ppbv where the initial O_3 mixing ratios exceeded 100 ppbv.

A comparison of the decrease in O_3 with and without lightning chemistry indicates that

titration by lightning NO_x only accounts for roughly a 2 ppbv decrease at most. This

suggests the upward transport of lower O_3 mixing ratio boundary layer air into the cloud

is responsible for almost all of the decrease in O_3 at anvil levels.

Table 13. The mean trace gas mixing ratios over the four model layers the aircraft flew within (10.72-10.97 km, 10.97-11.21 km, 11.71-11.95 km, and 11.95-12.20 km). CO and O_3 model values taken over (10.48-10.72 km, 10.72-10.97 km, 11.46-11.71 km, and 11.71-11.95 km). The asterisk indicates the observed LNO_x is an estimation based on mean aircraft observed total NO_x and the mean model-simulated background NO_x based on 82 moles fl^{-1}. Unless noted otherwise, each LNO_x production scenario used the observed flash channel vertical distribution and IC:CG ratio.

	Aircraft Observed Mean Mixing Ratios			
	CO (ppbv)	O₃ (ppbv)	NOₓ (ppbv)	LNOₓ (ppbv)
	118.7±4.7	86.1±6.6	1.4±0.6	1.2 *
LNOₓ Production Scenario	**Model-Simulated Mean Mixing Ratios**			
	CO (ppbv)	O₃ (ppbv)	NOₓ (ppbv)	LNOₓ (ppbv)
IC=CG=0	118.3±5.5	85.8±8.7	0.6±0.0	0
IC=CG=125; DeCaria vertical; Boccippio IC:CG	118.5±4.9	86.8±7.8	1.2±0.4	1.1±0.4
IC=CG=125; DeCaria vertical; Observed IC:CG	118.7±4.6	86.4±7.4	1.2±0.4	1.1±0.4
IC=CG=125; Observed vertical; Boccippio IC:CG	117.8±4.9	87.8±8.1	2.0±0.7	1.9±1.3
IC=CG=125	118.4±5.1	86.6±8.5	1.9±0.6	1.8±0.6
IC=CG=500	117.9±4.6	85.0±8.0	7.3±2.4	7.1±2.4
IC=CG=107	118.1±5.0	86.4±7.9	1.7±0.5	1.5±0.5
IC=CG=82	117.6±5.0	88.3±8.1	1.3±0.4	1.2±0.4
IC=38; CG=604	118.1±5.4	87.1±8.3	2.6±0.7	2.4±0.7
IC=21; CG=328	118.5±4.7	86.4±7.7	1.5±0.4	1.4±0.5
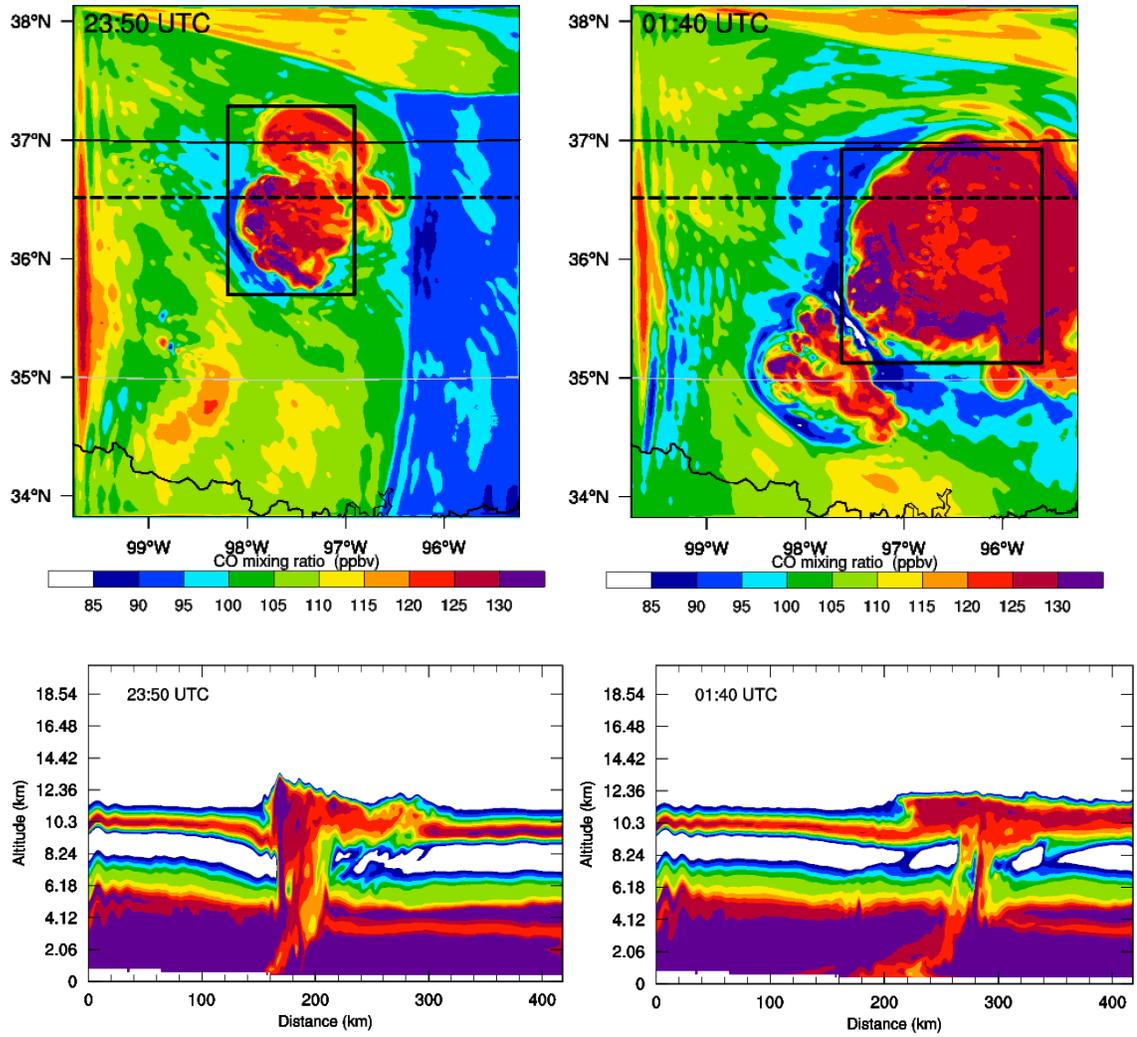
Figure 23. Horizontal and vertical cross sections of model-simulated CO at (left) 23:50 UTC model time and (right) 01:40 UTC model time. Units in ppbv.
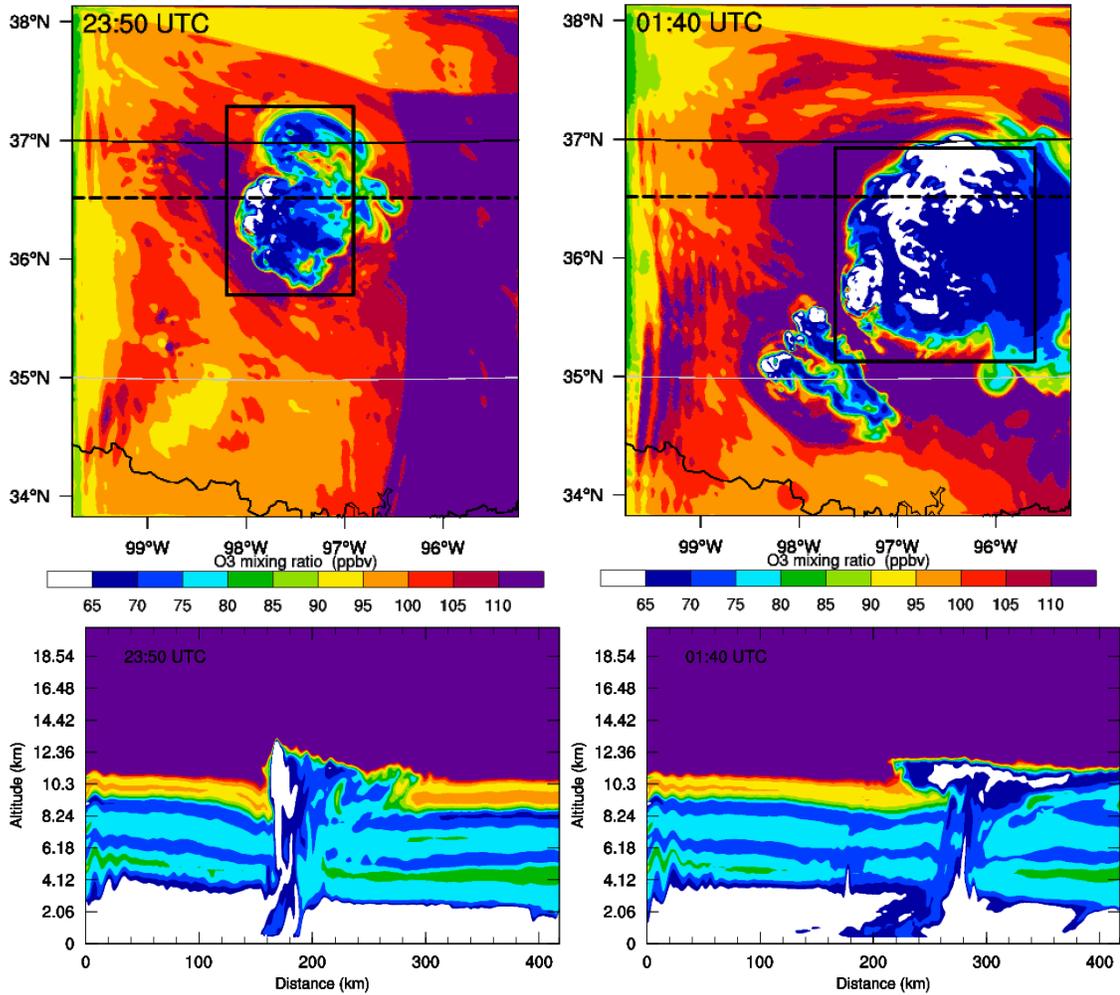
Figure 24. Horizontal and vertical cross sections of model-simulated O_3 at (left) 23:50 UTC model time and (right) 01:40 UTC model time. Units in ppbv.

7.2 Nitrogen oxides

7.2.1 NO_x and LNO_x mixing ratios

Since NOx is being injected into middle to upper troposphere, it is not influenced by convective transport to the same degree as CO and O_3. For the 29-30 May event the peak in CG and IC flash channel lengths and LNO_x occurs at 9.5 km and 10.5 km, respectively. In addition, LNO_x is inserted into the model following a bulk approach (not

a filament approach), so it is not realistic to expect the model to capture the proper

mixing ratios at specific locations. Therefore, the NO_x and LNO_x mixing ratios were

only compared within the model layers where the aircraft flew (Figure 25) on the basis of

means and standard deviations.
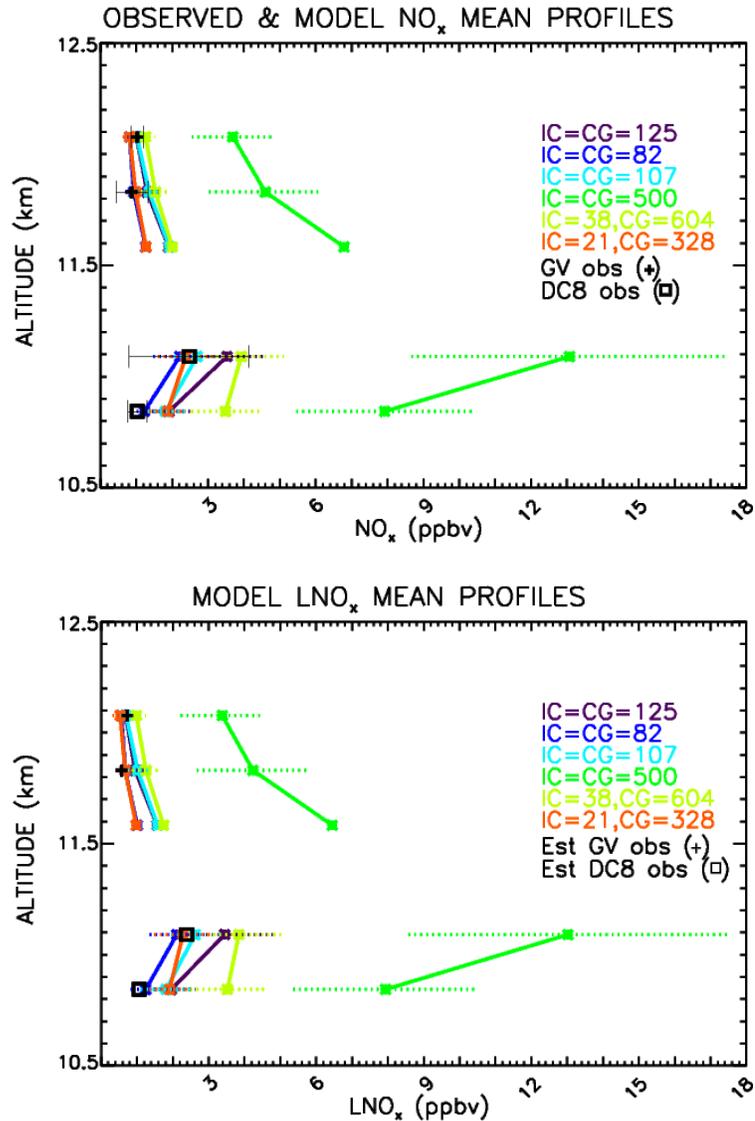
Figure 25. Aircraft observed and model-simulated mean (top) NO_x and (bottom) LNO_x mixing ratios within the same layers. The ±1 standard deviation is represented by solid black lines for the observed NO_x and dotted color lines for the model NO_x and LNO_x.

With lightning chemistry turned off, the overall mean NO_x from the four model layers (0.6 ppbv) underestimates the aircraft observed NO_x (1.4 ppbv) by ~55% over the same altitude intervals (Table 13). Depending on which LNO_x production scenario is assumed, the mean model-simulated NO_x mixing ratio bias varies anywhere from roughly -11% to +438%. An LNO_x production scenario of 82 moles per CG and IC flashes best represents the aircraft observations in the anvil outflow for the 29-30 May supercell storm system. Based on the overall mean from the four model layers, the model-simulated NO_x mixing ratio (1.3 ppbv) is within 5% of the aircraft observation. This scenario is much smaller than the mean value suggested by Ott et al. (2010) for midlatitude and subtropical storms (500 moles fl^{-1}). It is within the range of the LNO_x volume-based estimate Pollack et al. (2016) determined for this case study (107 ± 24 moles fl^{-1}); however, Pollack et al. (2016) believe this estimate may be biased low. The storm volume associated with thunderstorms outside of the aircraft's sampling region was not accounted for in the calculation, while the additional LNO_x they produced was likely transported downwind and observed by the aircraft. Schumann and Huntrieser (2007) suggest the best estimate of the LNO_x production is a mean 250 moles fl^{-1} (33-660 mole fl^{-1}) based on their review of theories, laboratory studies, field data, cloud-resolved modeling, and reviews from 1976-2007.

Both scenarios that incorporate the default model parameters for the fractional CG and IC flash channel vertical profiles (DeCaria et al., 2000) underestimate the aircraft observed NO_x by < 20%; however, these profiles emit LNO_x lower in the troposphere and are not representative of the observations. The default CG LNO_x peaks 3.5 km below the

observed peak for this storm system, while the default IC LNO_x has a secondary peak that maximizes at 6 km (Figure 9).

The two LNOM-based scenarios where the LNO_x production per CG flash was substantially greater than that for an IC flash both overestimated the observed NO_x. The scenario based on the LNOM estimate by Koshak et al. (2014) overestimated by ~88%, which is likely due to the mean 151 moles fl^{-1} being too large. The LNOM scenario that was adjusted to use a mean of 82 moles fl^{-1} was within 12% of the aircraft observed NO_x averaged over all four layers; however, the largest overestimate is within the 10.72-10.97 km layer (~80%), while the mean model-simulated NO_x within the other three model layers ranged from -20% to +11%. This results in a poorer simulation than the scenario that uses 82 moles per CG and IC flash in which each of the four layers are within ~20% of the observations and the model NO_x averaged over these layers underestimates the observations by ~4%. This suggests the partitioning of CG and IC LNO_x based on the LNOM scenario may not be as appropriate as equal LNO_x between CG and IC flashes, or the original LNOM estimate (Koshak et al., 2014), which is based on northern Alabama convection, may not be scaled for application in thunderstorms in other regions.

All further analyses and discussions will be based on the LNO_x production scenario of 82 moles NO per CG and IC flashes, unless otherwise noted. Since the aircraft cannot directly measure LNO_x in the anvil outflow, the observed LNO_x is estimated by taking the difference between the total NO_x observed by the aircraft and the model-simulated background NO_x. Table 13 shows that for this scenario the overall mean model-simulated LNO_x within the four model layers is within 5% of the estimation

109

of the mean observed LNO_x (1.2 ppbv). The results in Table 13 also suggest that there is

loss of NO_x due to chemistry (i.e., formation of HNO_3 and organic nitrates). The

summation of the mean total NO_x from the WRF-Chem simulation with no lightning

chemistry (0.6 ppbv) and the average model-simulated LNO_x (1.2 ppbv) within the anvil

outflow is greater than the mean total NO_x from the run with lightning chemistry

(1.3 ppbv).

In the model simulation, NO_x and LNO_x maxima were collocated with the O_3

minimum in the upper portion of the convective core (> ~7 km), as well as the anvil.

Here the mixing ratios for NO_x and LNO_x exceeded 2 ppbv. While the vertical cross-

sections suggest boundary layer NO_x is transported into the upper region of the

convective cells, the model-simulated LNO_x appears to make up ~88% of the NO_x within

the anvil. A comparison of the mean O_3 mixing ratios between the background profile

and the in-cloud profiles with and without LNO_x indicated O_3 decreased by at least

40 ppbv above 10.8 km altitude by the end of the simulation at 02:00 UTC model time.

The difference between the two in-cloud mean O_3 profiles showed the O_3 mixing ratios

were 1-2 ppbv lower in the WRF-Chem simulation with lightning chemistry. This

suggests almost all decreases in O_3 were due to the upward transport of boundary layer

air into the storm system and only a 1-2 ppbv O_3 loss was due to titration by NO.

7.2.2 LNO_x columns

The NO contribution from lightning is also analyzed from a remote sensing perspective

by determining the partial lightning NO_2 columns from the tropopause to 400 hPa, which

would be analogous to what a UV-Vis satellite spectrometer (such as the Ozone

Monitoring Instrument; OMI) would observe. In addition, the column amounts of LNO

and LNO_x are also computed. During this convective event, the tropopause was observed near 200 hPa by sounding and aircraft. Using the area of OMI's nadir footprint (13×24 km^2), the model-simulated partial LNO_x columns were calculated using the model NO_x output without and with (82 moles NO per flash) lightning chemistry. The model-simulated partial lightning NO, NO_2, and NO_x columns are shown in Figure 26. The maximum partial LNO_x column between 22:10-02:00 UTC model time was 8.2×10^{15} molecules cm^{-2} at 00:50 UTC while the free troposphere away from the convection provided a mean background of 0.031×10^{15} molecules cm^{-2}. Prior to 02:00 UTC, the peak partial lightning NO column was 5.3×10^{15} molecules cm^{-2} at 01:00 UTC and the peak partial NO_2 column due to lightning was 7.3×10^{15} molecules cm^{-2} at 01:50 UTC. The partial NO_2 column is slightly less than, but similar in magnitude to the peak determined by Ott et al. (2010) for their cloud-resolved simulation of the 21 July 1998 thunderstorm (9.0×10^{15} molecules cm^{-2}) observed during the European Lightning Nitrogen Oxides Project (EULINOX). The mean NO_2 background for the 29-30 May Oklahoma storm ranges from 0.022×10^{15} to 0.047×10^{15} molecules cm^{-2} from 00:00-02:00 UTC model time, which is an order of magnitude less than the mean backgrounds of the five subtropical and midlatitude thunderstorms simulated by Ott et al. (2010).

Figure 27 shows a time series of the summation of the moles within the partial columns over the convective core and anvil from 00:00-02:00 UTC. The simulated anvil begins to exit the model domain at 01:00 UTC model time. The downward trend in moles NO due to lightning is likely related to sunset, which occurred at 01:38 UTC observed time on 29 May. This means the NO_2 photolysis shuts off and the NO_2 component of NO_x increases, since NO is no longer being produced via this reaction.
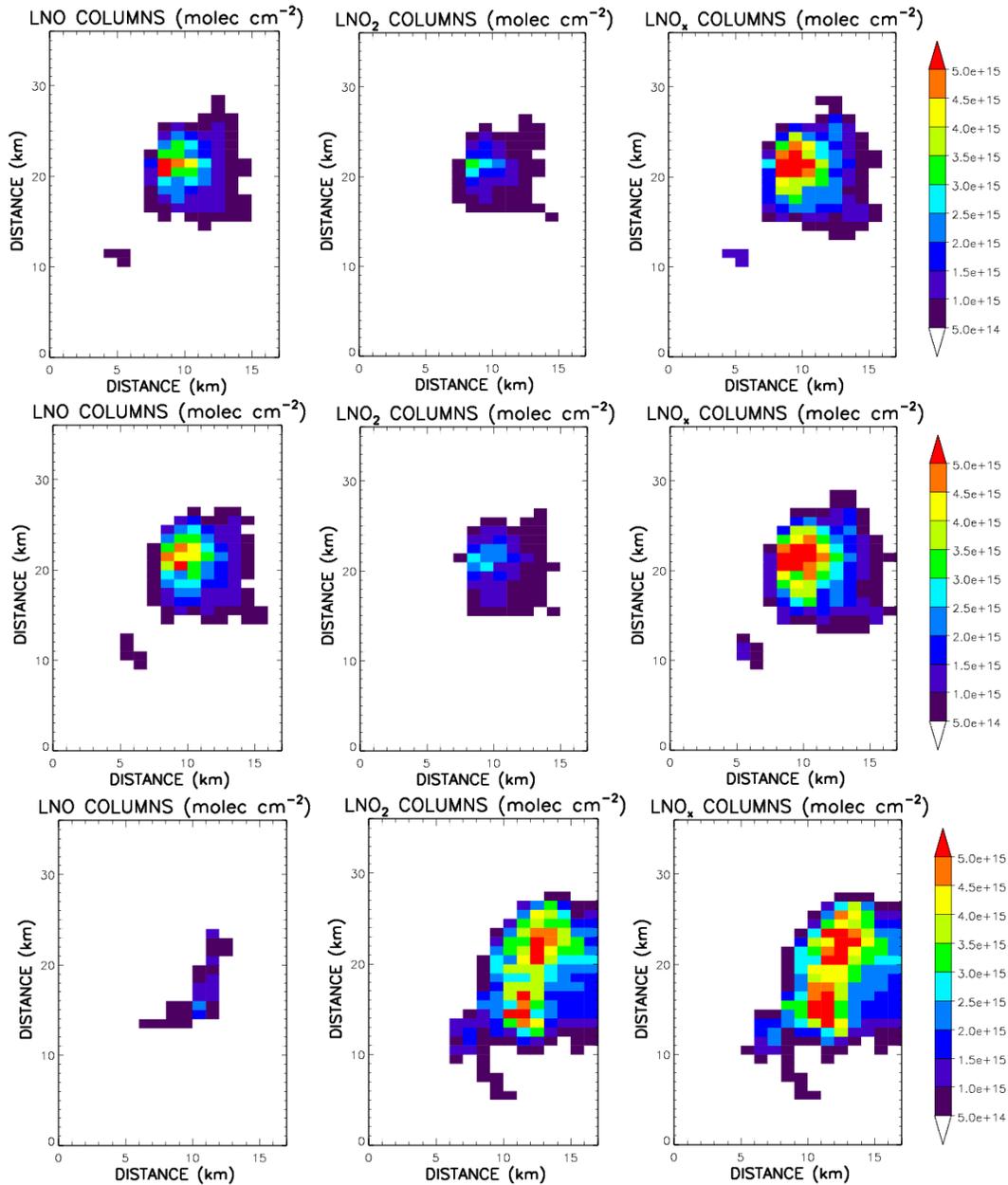
Figure 26. Model-simulated partial lightning NO, NO$_2$, and NO$_x$ columns from tropopause (200 mb) to 400 mb at 00:50 UTC (top row), 01:00 UTC (middle row), and 01:50 UTC (bottom row). Each grid cell represents a 13 km × 24 km area.
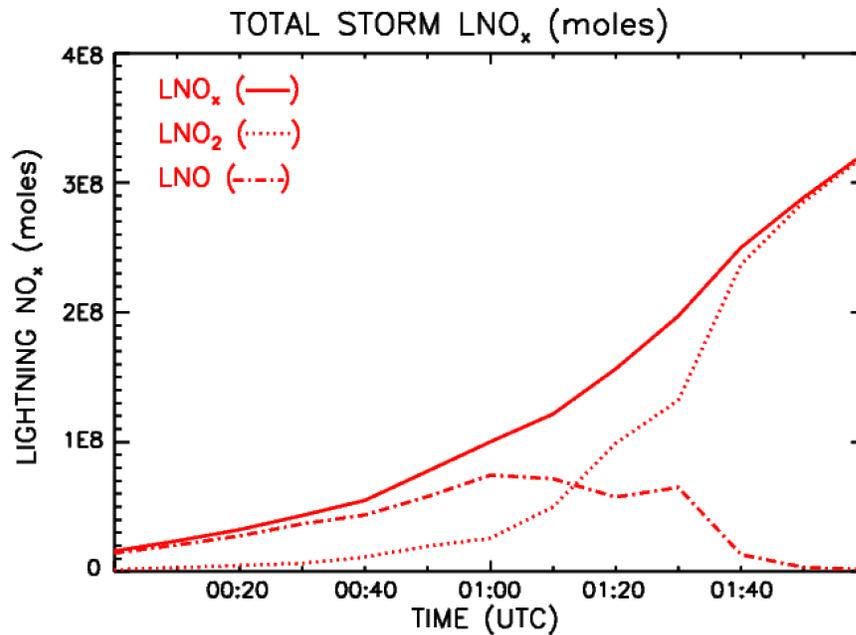
Figure 27. Time series of the total model-simulated partial lightning NO, NO_2, and NO_x columns between the tropopause (200 mb) and 400 mb within the convective core and anvil from 00:00-02:00 UTC model time. Units are in moles.

7.3 Relationships between flash rate, flash extent, flash energy and LNO_x production

One of the objectives of this work is to determine if the LNO_x production per flash can be related to characteristics of the lightning itself or to other storm features such as the wind profile. The 29-30 May severe supercell system, which includes the Kingfisher storm (DiGangi et al., 2016), is considered a high flash rate event. High flash rate storms have shorter lengths per flash (Bruning and MacGorman, 2013; Bruning and Thomas, 2015; Mecikalski et al., 2015), which may result in a smaller amount of NO_x produced per flash. While this hypothesis regarding LNO_x production variability focuses on cloud electrification characteristics, an alternative hypothesis concerning LNO_x production considers vertical wind shear, which is defined as the difference in the wind vectors between the anvil outflow and steering level (~700 hPa). This hypothesis suggests NO_x production increases as lightning flashes are elongated with increasing vertical wind

shear (Huntrieser et al., 2008, 2009, 2011). The vertical wind shears observed between the anvil outflow and the steering level (~700 hPa) during the Tropical Convection, Cirrus and Nitrogen Oxides Experiment (TROCCINOX; Huntrieser et al., 2008), SCOUT-O3/ACTIVE (Huntrieser et al., 2009), and African Monsoon Multidisciplinary Analysis (AMMA; Huntrieser et al., 2011) campaigns ranged from 2.8-20.0 m s^{-1} with a mean of 10.4 m s^{-1}. The estimated LNO$_x$ production per flash in these tropical and subtropical regions ranged from 67-391 moles flash^{-1} with a mean of 161 moles flash^{-1}. During DC3 the mean wind speed was 35.8 m s^{-1} in the anvil outflow while the GV and DC3 were making anvil transects between 10.9-12.2 km from 23:48-00:23 UTC. The 00:00 UTC observed sounding showed steering flow was 17.4 m s^{-1} from the west-southwest (~250°). The observed mean vertical wind shear on 30 May was 23.8 m s^{-1} at west-northwest (~285°), which is roughly two times stronger than the convection observed in the tropics and subtropics. This suggests the wind shear hypothesis is not true for the 29-30 May convection given the stronger vertical wind shear and small LNO$_x$ production per flash (82 moles flash^{-1}).

Total lightning flashes associated with the convection are within the 2D detection capability of the central OK LMA (200 km) for the majority of the system's life cycle (21:10-04:20 UTC). However, the 3D features of the system are detectable from ~23:40-03:00 UTC, when the convection is within ~100 km of the network (Figure 5). The LMA data, averaged in 10-min intervals, was used to calculate the Pearson correlation coefficient and assess the relationship between total flash rate and specific lightning characteristics within the 3D coverage. During this time period the mean flash extent and mean energy per flash were ~6.5 km and ~76 J s^2 kg^{-1}, respectively, with a mean flash

rate of 133 total flashes per 10-min. There was a moderate negative correlation between mean flash rate and mean flash extent (r = -0.69, n = 21, p = 0.01; Figure 28) and between mean flash rate and mean energy per flash (r = -70, n = 21, p = 0.01; Figure 29). This means there is a 1% chance that either relationship would exist if the variables were not related and implies the correlations were not due to chance. This also suggests that while the convection was within the 3D coverage that 48% of the variability in mean flash extent and 49% of the variability in mean energy per flash are explained by mean flash rate.

While the relationships appear to continue as very weakly negative (r = -0.20 to r = -0.30) after 03:00 UTC, the data suggests that within the first 2.5 hours after convective initiation (21:10 to 23:40 UTC) both relationships are instead moderate positive (roughly r = +0.70); however, during these two periods there is much uncertainty with these results, since the lightning is mainly outside of the 3D region. A more accurate determination of the flash detection efficiency and location errors on this day could be made using a closer inspection of the active LMA stations along with the open-source simulation tools by Chmielewski and Bruning (2016). However, the moderate negative correlations during the period of 3D data suggest an estimate of flash rate can yield rough approximation of extent and energy per flash.
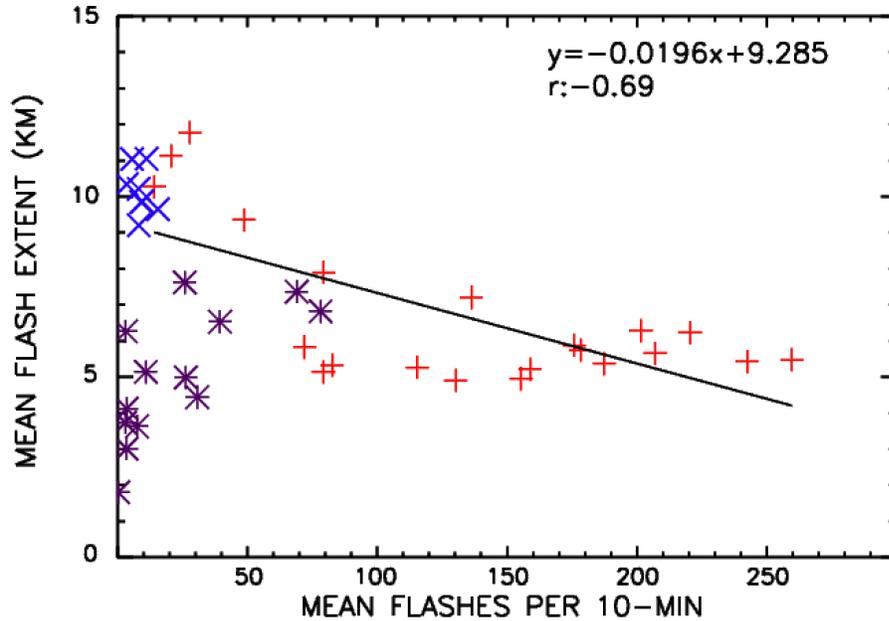
Figure 28. Correlation between the observed 10-min mean flash rate and mean flash extent within the 3D coverage of the central OK LMA network (23:40-03:00 UTC). The red plus represents the data points within the 3D coverage. The purple asterisk represents the data points prior to the 3D coverage (21:30-23:30 UTC). The blue cross represents the data points after the 3D coverage (03:10-04:20 UTC).
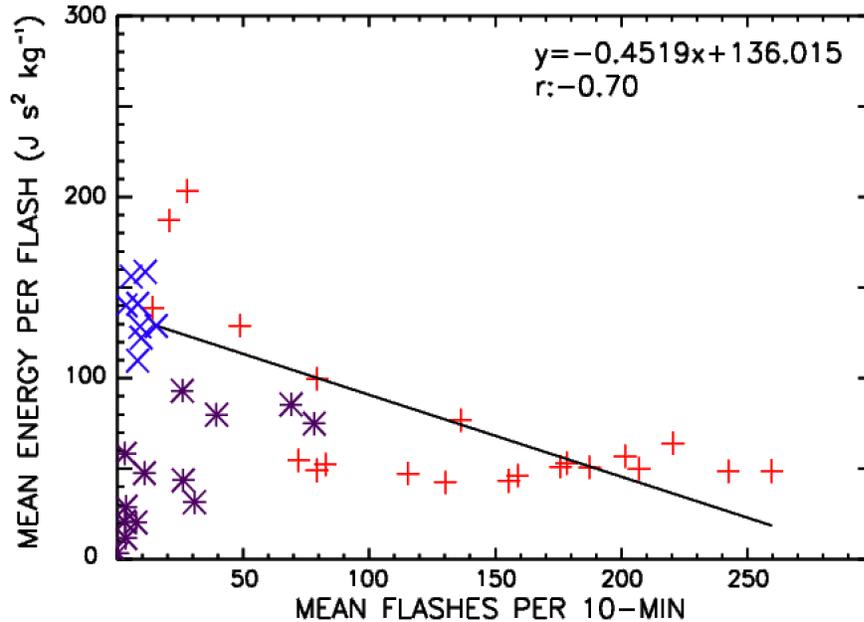
Figure 29. Same as Figure 28, except the correlation is between the observed 10-min mean flash rate and mean energy per flash.

116

Using data provided by Pollack et al. (2016) from six DC3 events, I further

investigated the relationship between flash extent and LNO$_x$ production. Figure 10 in

Pollack et al. (2016) indicated a weak to moderate positive correlation exists between

cumulative flash area and LNO$_x$ production per flash over these events. I investigated

whether a more relevant relationship exists between the mean flash areas for each event

and their respective mean moles NO flash^{-1}. The mean flash area was calculated for each

event using the sum of the flash energy during the convection, which is proportional to

total flash area (Bruning and Thomas, 2015), given the time periods specified in Table 3

of Pollack et al. (2016) and dividing by the total number of flashes in that time interval.

Since the LMA data is based on the slightly larger 3-hour moving spatial masks I initially

defined (Bruning, 2014a, 2014b), I included a second data point for the 29-30 May case,

which is based on 10-min masks that cover the more specific portion of the convection

considered in the simulation. The mean flash area for this data point uses the same

method as described above, except only the flash data within the LMA 3D coverage is

used (23:40-03:00 UTC). Figure 30 shows a weak to moderate positive correlation

($r = +0.42$, $n = 13$, $p = 0.01$) also exists when the mean flash area is considered instead of

total flash area. Although this relationship is moderate at best, it suggests the correlation

is not due to chance and that mean flash area explains 18% of the variability in mean

LNO$_x$ production. Therefore, the relationship is worth further exploration since it

indicates the potential development of a parameterization scheme for LNO$_x$ production

per flash based on flash rate.
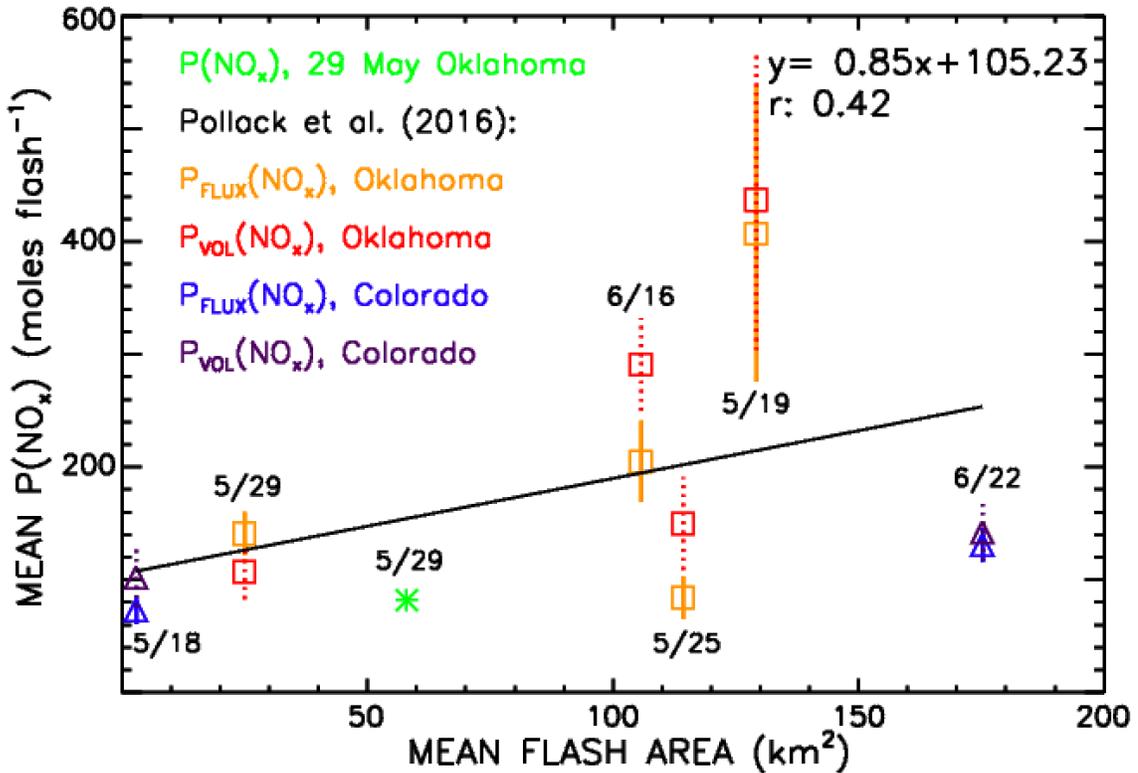
Figure 30. Correlation between the mean flash area and LNO$_x$ production per flash for six convective events observed during DC3. The squares and triangles represent Oklahoma and Colorado convection, respectively. LNO$_x$ production using the flux-based approach is represented by orange and blue, while the volume-based approach is represented by red and purple. The green asterisk represents the 29-30 May event based on data within the 10-min moving spatial masks and 3D coverage of the central OK LMA network (23:40-03:00 UTC).

7.4 Flash rate variation between LNO$_x$ production scenarios

After the WRF simulations without chemistry, with chemistry and no LNO$_x$, and different LNO$_x$ production scenarios were run, variations in the model-simulated flash rates were noticed. The number of total flashes simulated from 22:10-02:00 UTC model time varies by less than 100 flashes between the run with no chemistry (14,419 flashes) and the run with chemistry but no LNO$_x$ production (14,344 flashes). Figure 31 shows slight variation in the flash rate time series occurs around 23:10 UTC, 00:00 UTC, and 02:00 UTC. I decided to investigate the cause of these differences in flash rate. Since

the GOCART aerosols have a direct effect on the radiation in the model, I hypothesize that the resulting heating/cooling changes can affect the calculation of the ICEFLUX storm parameter used in this case study to predict lightning activity. With the chemistry turned on variations in the aerosol concentrations may result, affecting the radiation and, in turn the kinematics of the storm.
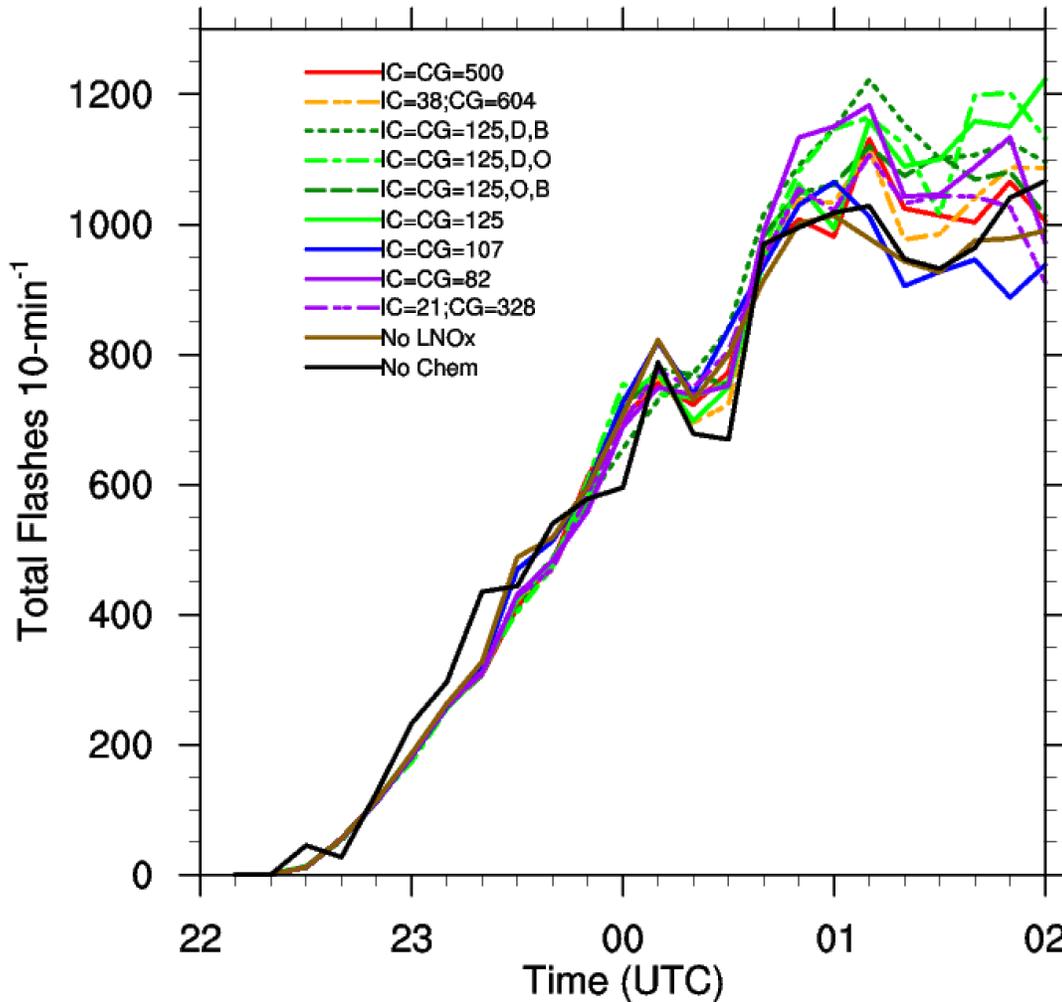
Figure 31. Model-simulated flash rate time series based on the meteorology only run (No Chem), chemistry run with no lightning chemistry (No LNO$_x$), and nine chemistry runs with varying LNO$_x$ production scenarios, vertical flash channel length distributions, and IC:CG ratios. Each LNO$_x$ production scenario used the observed flash channel vertical distribution and IC:CG ratio, unless the scenario in the legend contains a D for the DeCaria vertical distribution or a B for the Boccippio IC:CG ratio.

As each of the nine LNO$_x$ production scenarios were tested, their individual flash rate time series showed additional variation from the runs with and without chemistry, as well as between each scenario. Also, the total number of flashes predicted by the nine scenarios from 22:10-02:00 UTC varies by roughly 1,200 flashes. The initial assumption of 125 moles NO flash^{-1} tested four different combinations of flash channel length vertical distributions (default and observed) and IC:CG ratios (default and observed). The two runs that apply the observed IC:CG ratios show similar changes in flash rates, just like the two runs that use the Boccippio IC:CG ratios. A comparison of the total number of flashes showed the two scenarios using the DeCaria flash channel length vertical distributions (DeCaria et al., 2000) produced roughly 195-460 more flashes than the two scenarios using the observed vertical profile. This suggests the CG and IC LNO$_x$ emitted at lower altitudes (6.5 km) in the DeCaria scheme may cause the lightning activity to increase. Also included are two runs that both use 82 moles NO flash^{-1}. While the variation in their flash rates is similar, the simulation that assumed equal LNO$_x$ production between the CG and IC flashes shows higher flash rates and predicts more flashes (15,076 flashes) than the run that presumed the CG LNO$_x$ production was larger (14,631 flashes). When 107 moles NO flash^{-1} is assumed, the fluctuation in flash rates is similar to the run with no lightning chemistry.

Among the six scenarios using the observed vertical distributions and IC:CG ratios, the total number of flashes simulated between 22:10-02:00 UTC does not increase or decrease as the moles NO flash^{-1} increases. While the magnitude of the flash rate peaks differ between the six runs, they generally occur at the same time (i.e., 00:10 UTC, 00:50 UTC, 01:10 UTC, and 01:50 UTC) and show a maximum peak between 01:00-

01:10 UTC. However, the simulations that assumed 107 and 125 moles NO flash^{-1} each

show two flash rate peaks after 01:10 UTC instead of one. The run using 107 moles also

indicates there is one peak at 01:00 UTC instead of at ±10 minutes like the other five

scenarios.

Since these differences are most noticeable after 00:00 UTC, a closer look was

taken at the potential variables driving these changes. The ICEFLUX storm parameter

considers the nonprecipitation ice and snow that are present at the 390 hPa pressure level.

Figure 32 shows the total ICEFLUX time series for each of the 10 scenarios evolves

similarly to the simulated flash rates over the 2-hour period; however, based on the time

series it is the nonprecipitation snow (Figure 33) that drives the ICEFLUX and not the

nonprecipitation ice (Figure 34). The total snow mixing ratios (Figure 35) and the mean

upward vertical velocities (Figure 36) both appear to affect the fluctuations in the

nonprecipitation snow. While the snow mixing ratio causes the general shape of the

nonprecipitation snow time series to increase, the vertical velocity provides the variation

in the time series. This helps provide some explanation for what variables have a greater

influence on ICEFLUX, but since each simulation is initiated with different chemistry

assumptions (i.e., no chemistry and chemistry with and without LNO$_x$), there are likely

additional factors responsible for creating the differences in the storm parameter and flash

rate time series. However, with the use of the GOCART aerosol scheme, there is no

connection of the aerosol with the microphysics. Therefore, changes in aerosol will not

directly affect the hydrometeor mixing ratios. But, changes in vertical velocity can affect

the amount of ice and snow production in the cloud.

Each of the six simulations with differing LNO$_x$ production scenarios show a general decrease in the mean concentration of dust (Figure 37) and aged (hydrophilic) black carbon (Figure 38) and organic carbon (Figure 39) within the convective system at 390 hPa between 00:00-02:00 UTC model time. There is little variation among these three aerosols in the six simulations except for the assumption of 107 moles NO flash^{-1}, which has a slightly lower mean concentration. The general lack of variation suggests these do not contribute to the variation in flash count.

The mean NO$_x$, NO$_2$, and NO time series (Figures 40-42) do not directly contribute to the variation in flash rates, as there is no similarity in the patterns to that of ICEFLUX. However, when using the observed vertical distributions and IC:CG ratios, the time series of these gases, as expected, show that as the production of NO flash^{-1} increases, so do the mixing ratios. (i.e., 82 moles NO flash^{-1} has the lowest mean mixing ratios, while 500 moles NO flash^{-1} has the highest mean mixing ratios). The two scenarios that use the DeCaria et al. (2000) vertical distribution have the highest mixing ratios, which is likely due to how close the 390 hPa pressure level is to the peak in CG and IC lightning flash channel lengths at 6.5 km. The increasing and decreasing trends in NO$_2$ and NO, respectively, are due to photolysis shutting off at the end of the day. Although the mean HO$_2$ and OH time series (Figures 43 and 44) decrease over the 2-hour interval due to the loss of sunlight, these chemical species may play a role in the flash rate variation due to the chemical interaction with NO. The sulfate aerosol time series showed little variation in the model output from the WRF-Chem simulations with no lightning chemistry and with 107 moles NO flash^{-1} (not shown); therefore, additional LNO$_x$ production scenarios were not analyzed. The GOCART aerosol scheme does not

include nitrate, so a different aerosol scheme will need to be used to examine the

potential influence of nitrate on the variation in model flash count due to changes in NO_x.

It is not clear what is causing the ICEFLUX and flash rates to vary among the

nine different LNO_x production scenarios and WRF-Chem run without LNO_x chemistry.

However, a combination of aerosol formation reactions and feedback processes to the

storm kinematics and microphysics in the presence of varying amounts of LNO_x is likely

cause for the variation in ICEFLUX and flash rates.
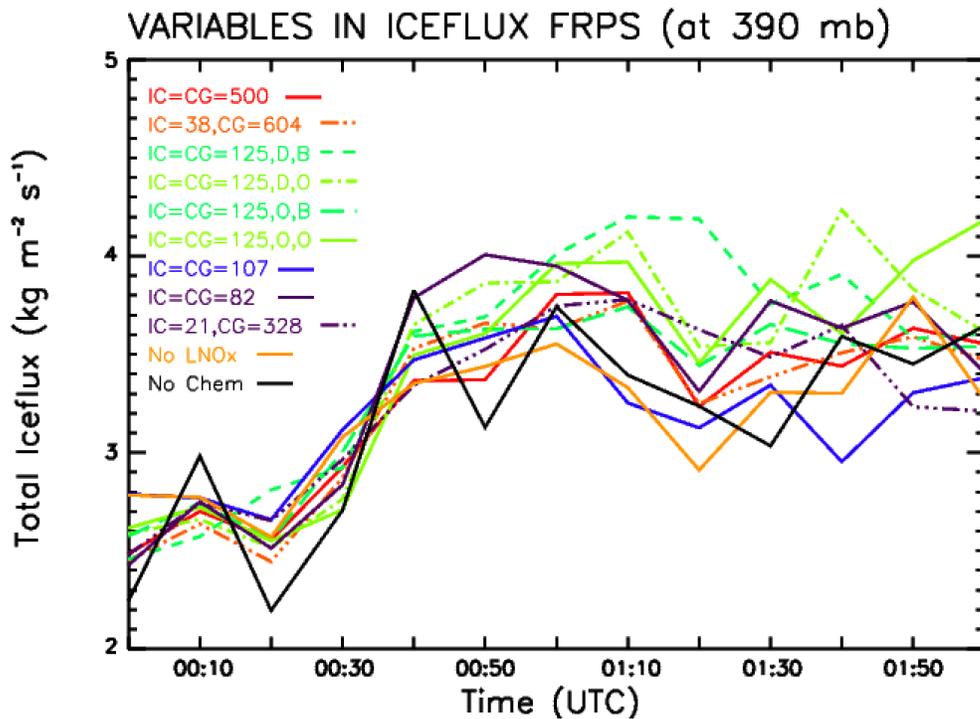
Figure 32. Total model-simulated ICEFLUX (kg m^{-2} s^{-1}) time series from 00:00 UTC to 02:00 UTC model time based on the meteorology only run (No Chem), chemistry run with no lightning chemistry (No LNO_x), and nine chemistry runs with varying LNO_x production scenarios, vertical flash channel length distributions, and IC:CG ratios. Each LNO_x production scenario used the observed flash channel vertical distribution and IC:CG ratio, unless the scenario in the legend contains a D for the DeCaria vertical distribution or a B for the Boccippio IC:CG ratio.
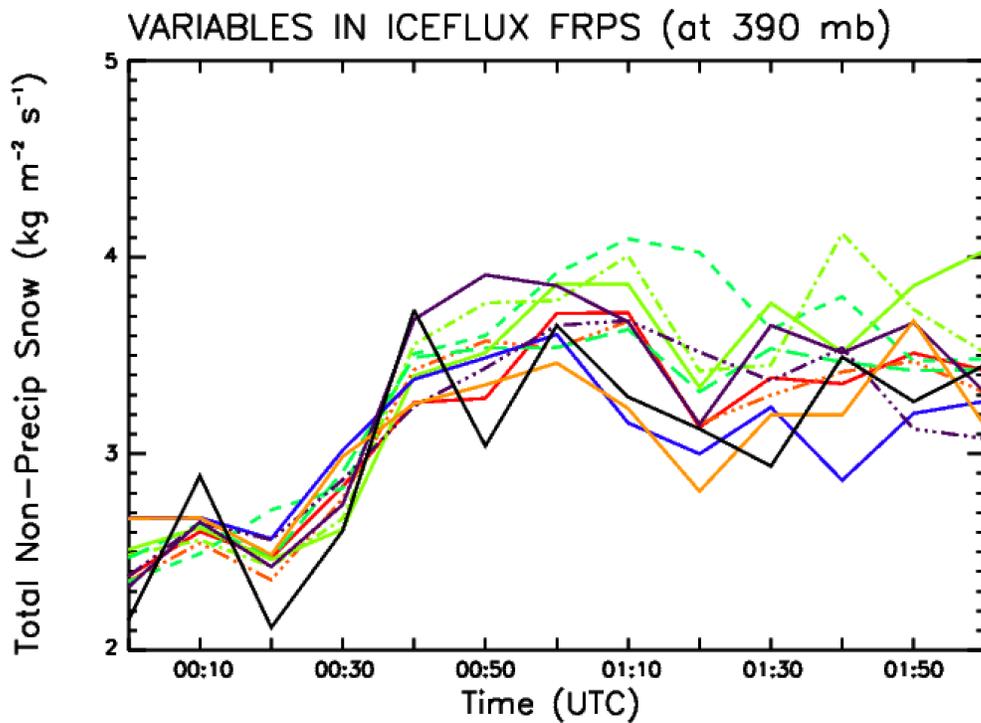
Figure 33. Same as Figure 32, except for the total model-simulated nonprecipitation snow (kg m^{-2} s^{-1}).
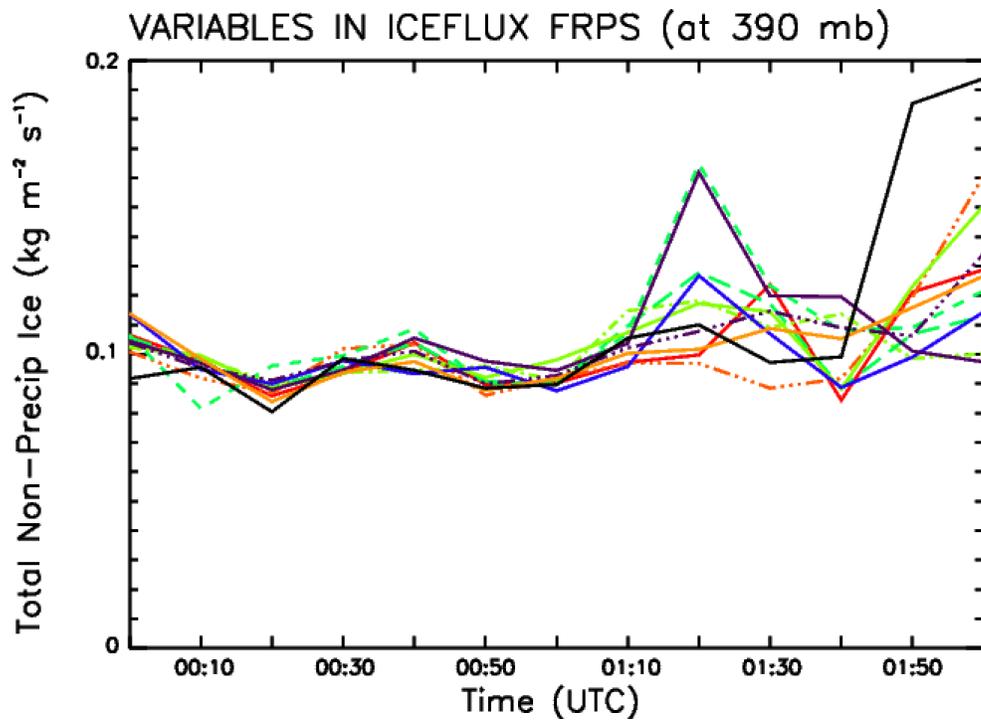
Figure 34. Same as Figure 32, except for the total model-simulated nonprecipitation ice (kg m^{-2} s^{-1}).
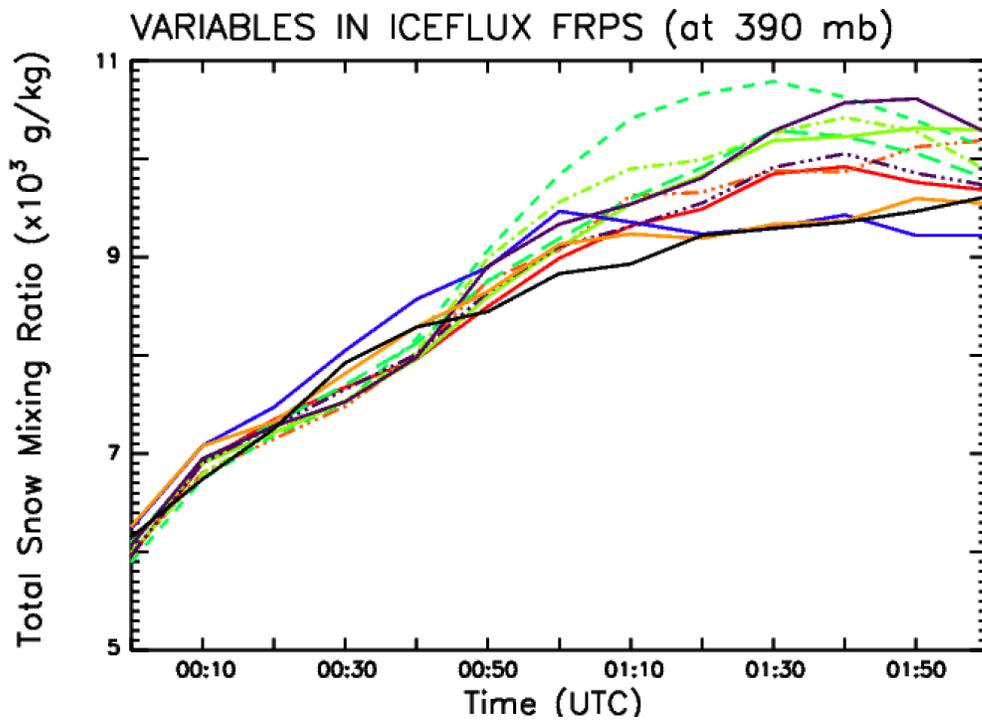
Figure 35. Same as Figure 32, except for the total model-simulated snow mixing ratio ($\times 10^3$ g kg^{-1}).
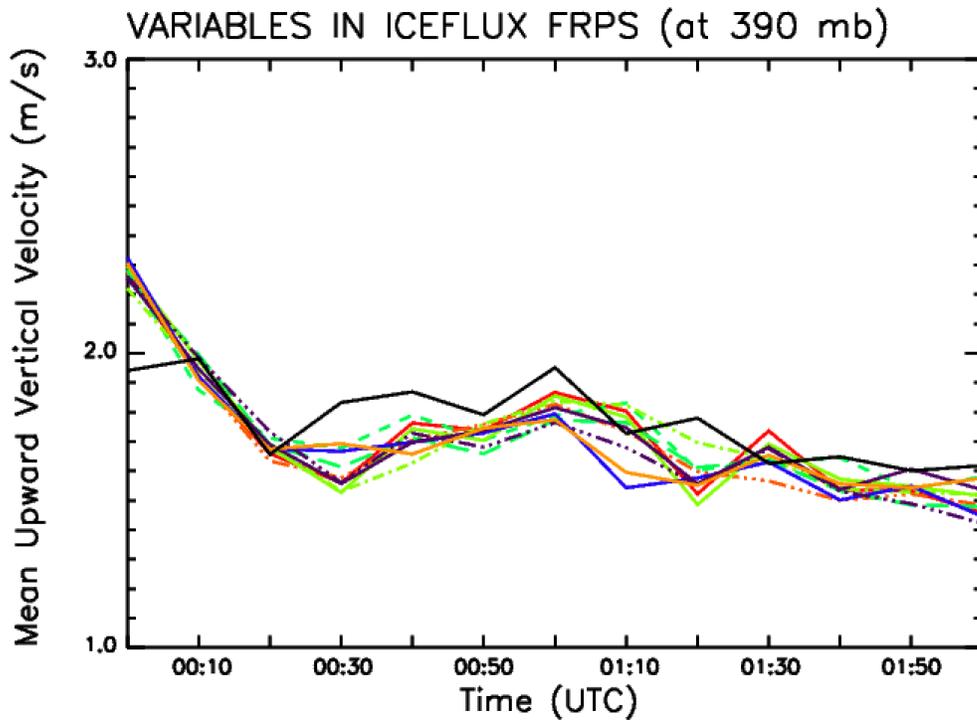
Figure 36. Same as Figure 32, except for the mean model-simulated upward vertical velocity (m s^{-1}).
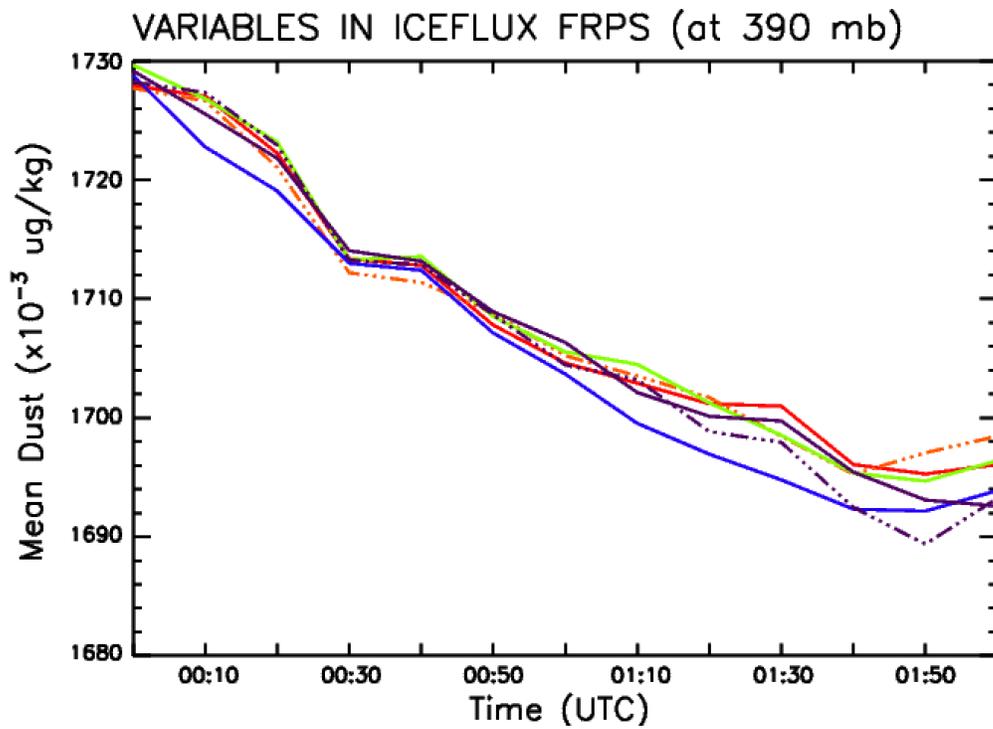
Figure 37. Same as Figure 32, except for the mean model-simulated dust (μg kg^{-1}).
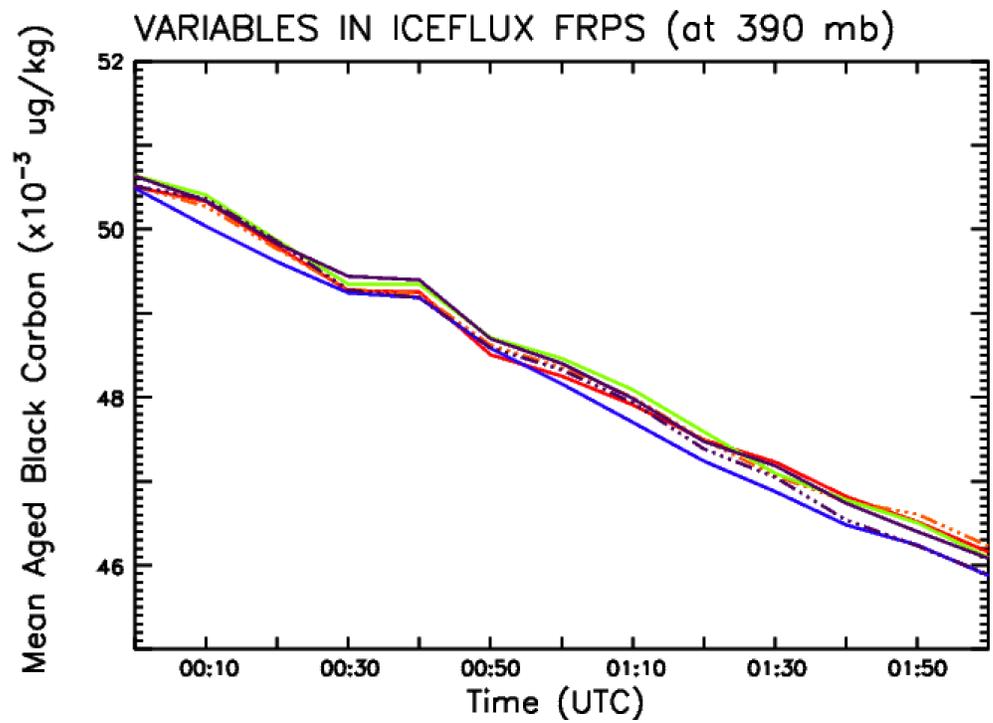
Figure 38. Same as Figure 32, except for the mean model-simulated aged (hydrophilic) black carbon (μg kg^{-1}).
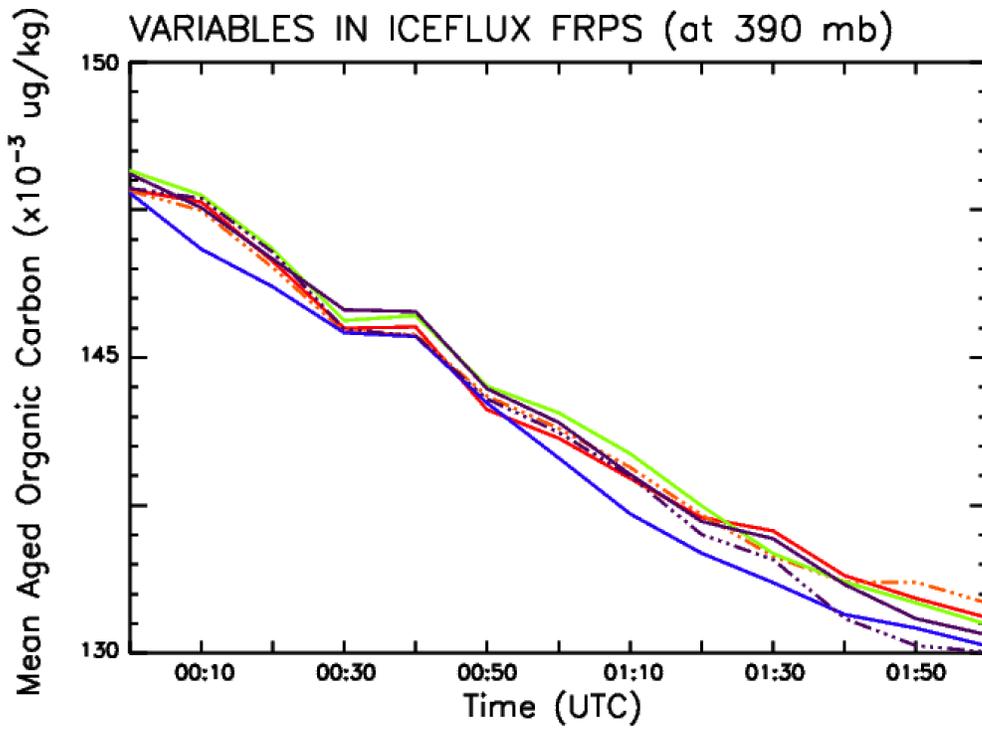
Figure 39. Same as Figure 32, except for the mean model-simulated aged (hydrophilic) organic carbon (μg kg^{-1}).
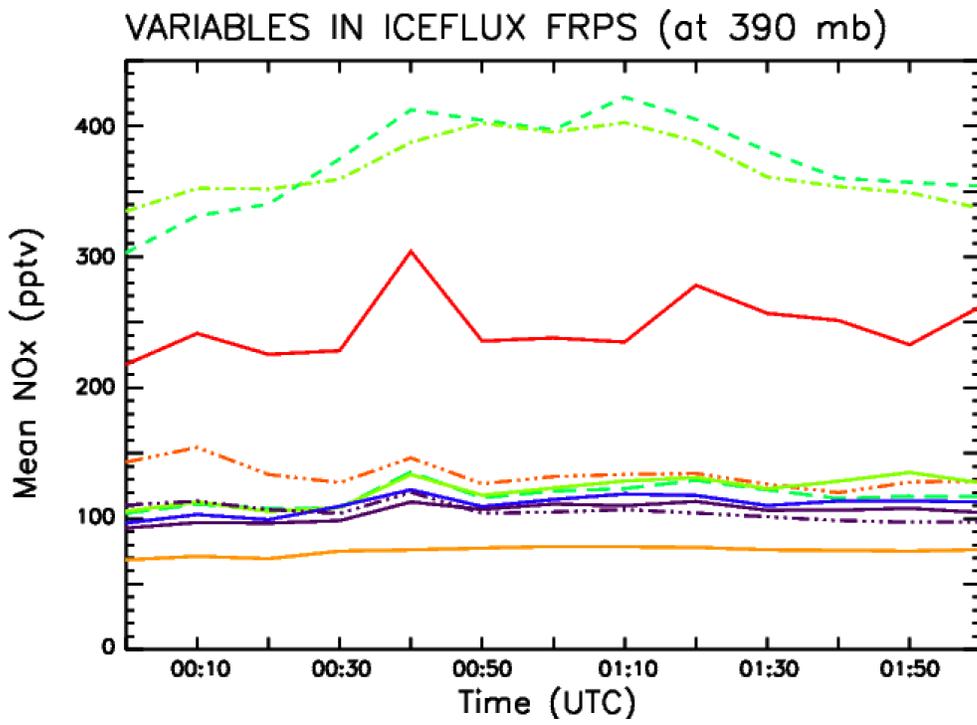
Figure 40. Same as Figure 32, except for the mean model-simulated NO$_x$ in parts per trillion volume (pptv).
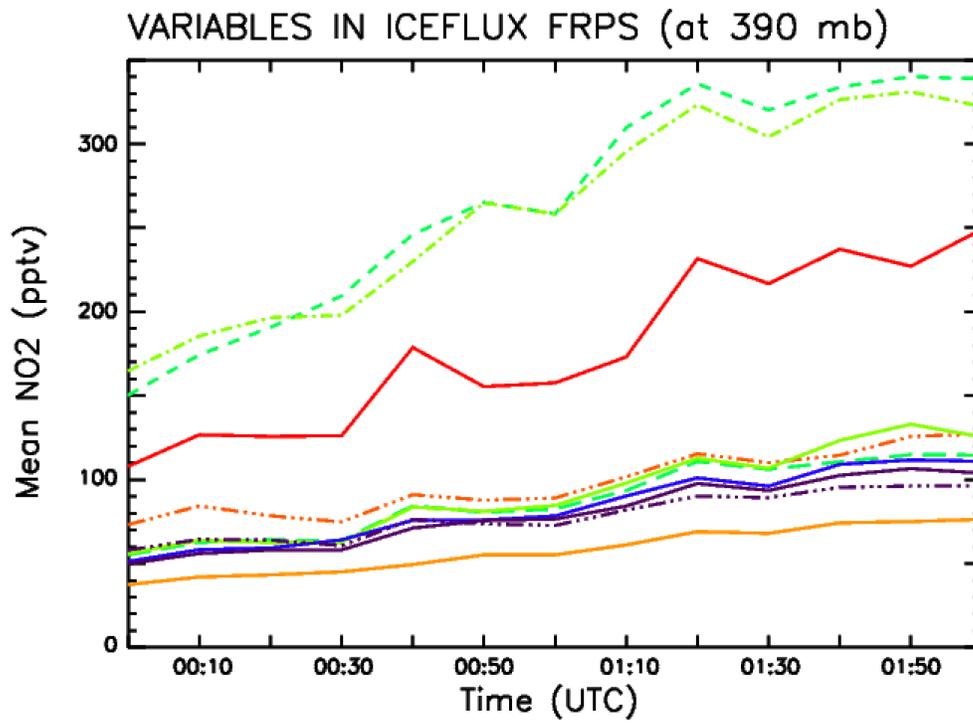
Figure 41. Same as Figure 32, except for the mean model-simulated NO_2 (pptv).
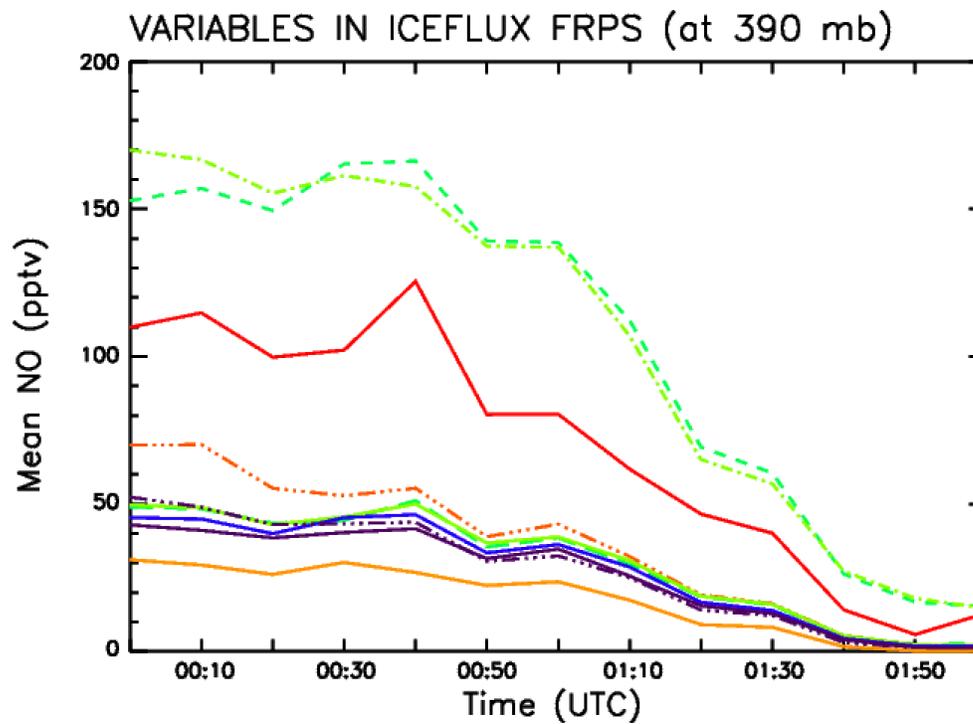
Figure 42. Same as Figure 32, except for the mean model-simulated NO (pptv).
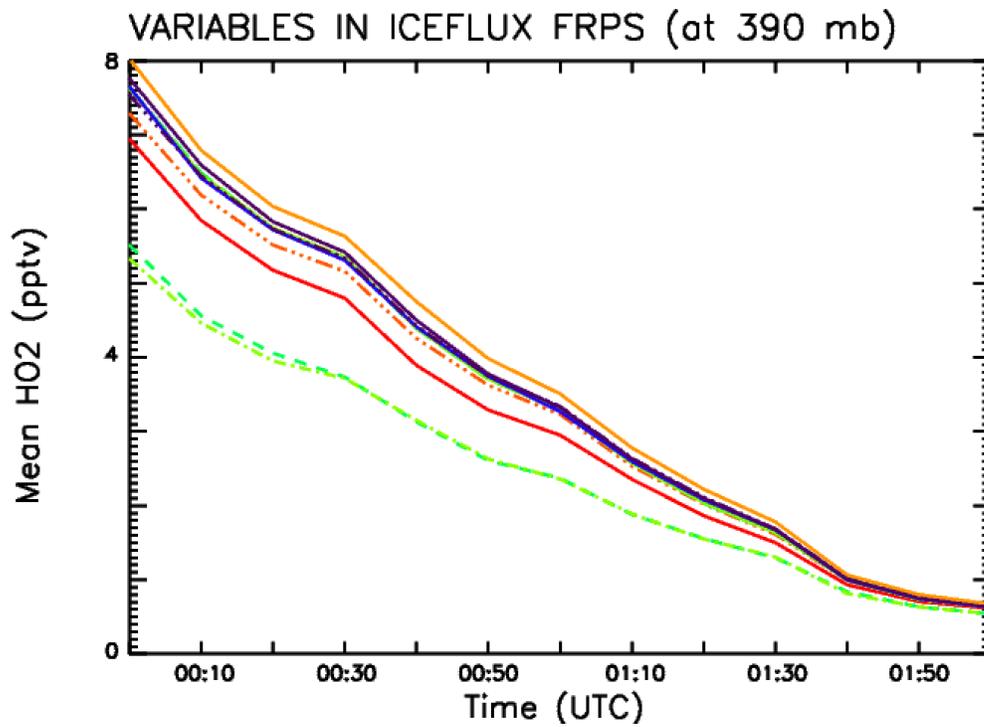
Figure 43. Same as Figure 32, except for the mean model-simulated HO$_2$ (pptv).
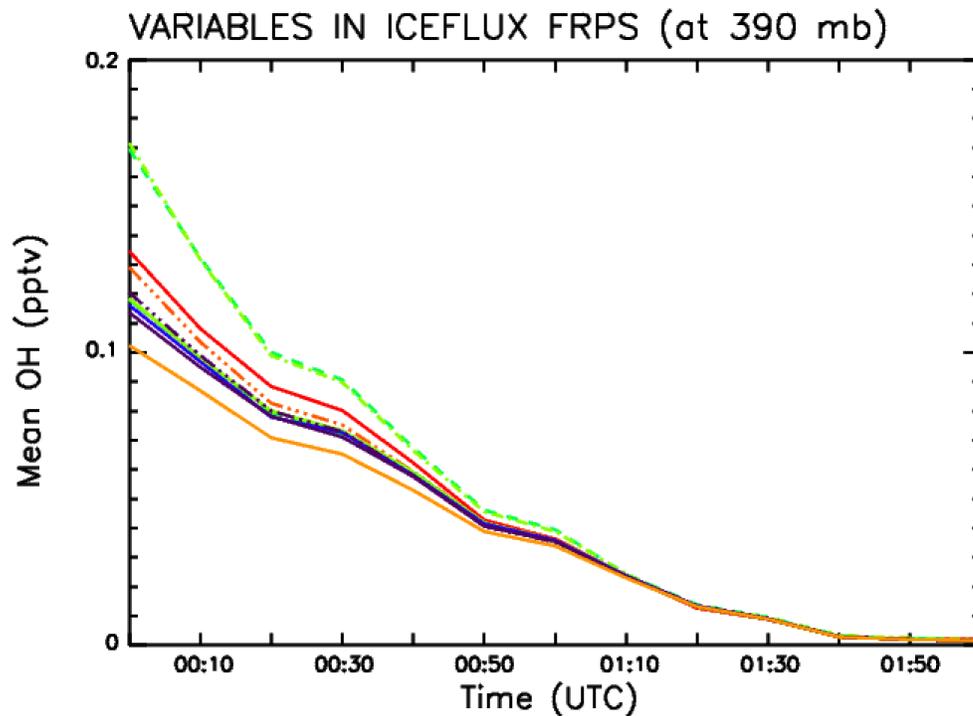
Figure 44. Same as Figure 32, except for the mean model-simulated OH (pptv).

CHAPTER 8: DOWNWIND TROPOSPHERIC CHEMISTRY

Convective outflow undergoes chemical reactions as it is transported downwind through the upper troposphere. These reactions include oxidation of NO and NO_2 photolysis, which result in O_3 production. NO_2 can be oxidized to HNO_3 and peroxyacetyl nitrate (PAN). Changes to the plume can be tracked and analyzed through the use of aircraft and satellite observations, as well as model simulations. DC3 offered a unique opportunity for aircraft to sample anvil outflow from an active thunderstorm and to locate the same air mass the following day.

8.1 Identifying and classifying areas of enhanced partial lightning NO_2 columns

Remote sensing by satellites help provide information about trace gas concentrations, such as NO_2, in the earth's atmosphere. The OMI, which is found onboard NASA's Earth Observing System (EOS)-Aura satellite, is one example of the instruments that have been used to provide NO_2 retrievals of vertical column content. OMI is a UV-Vis spectrometer and can sense sunlight that is backscattered between 270-500 nm (Boersma et al., 2011). NO dominates over NO_2 in the daytime in upper tropospheric convective outflow. However, NO_2 is easier to detect than NO through remote sensing (Schumann and Huntrieser, 2007). A near-real-time lightning NO_2 algorithm was developed by Pickering et al. (2014) for use in processing OMI data in relatively clear-sky regions to help identify areas of enhanced NO_2 due to upwind lightning. During DC3, the resulting images generated by the algorithm provided an additional real-time operational product that could be used to help justify the location of the sampling region for the downwind research flights.

As part of the DC3 lightning chemistry team in the field, I analyzed the OMI images generated daily in combination with the forward FLEXPART dispersion model and backward HYSPLIT model trajectories of the upper level air to help direct the DC3 aircraft to the general location of the convective outflow plume that was sampled the previous afternoon/evening. Post-campaign I analyzed every OMI image from May-June 2012 in detail to identify whether each area of enhanced NO_2 across the continental United States was related to lightning, as the algorithm indicated, or if these regions were related to some other feature or event, such as wildfires or anthropogenic sources. If the contributions from the non-lightning sources were above the NO_2 climatological background value, then the algorithm would incorrectly classify the source as lightning.

For example, Figure 45 shows the tropospheric lightning NO_2 columns observed by OMI at ~18:30 UTC on 30 May 2012. On this day the enhanced NO_2 over the southern Appalachian region is likely associated with the severe supercell system that was sampled by the DC3 research aircraft as the convection moved through Oklahoma the prior evening. Backward trajectories from the NOAA HYSPLIT model indicated that at 18 UTC on 30 May the air masses at 8 km, 10 km, and 12 km altitude within the region of enhanced LNO_2 passed through lightning activity over the previous 12 to 42 hours. Figure 46a shows the 8 km trajectory intercepted lightning at 00 UTC 29 May (Figure 47a), which was not part of the previous day's research flight, and the 12 km trajectory passed through the convection sampled by the DC3 aircraft between 18 UTC 29 May and 00 UTC 30 May (Figures 47b and 47c). Figure 46b also indicates that the 10 km and 12 km trajectories passed near the supercell system between 00-06 UTC 30 May. The

vast majority of the downwind impact on NO_2 was from the storm system sampled by the

aircraft.
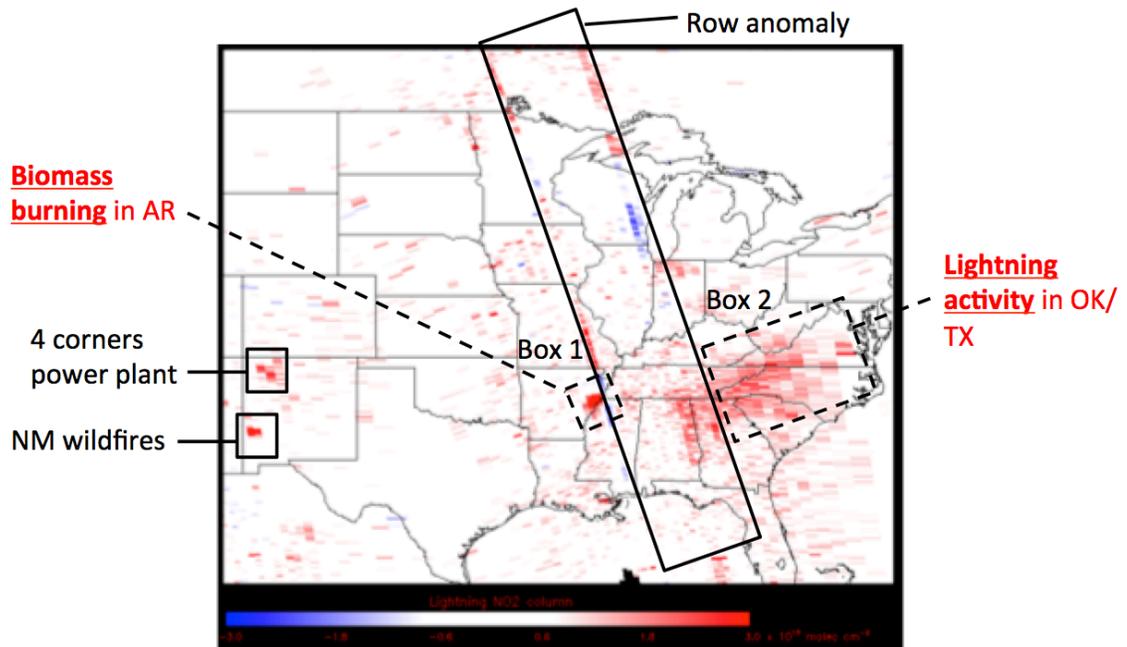
Figure 45. The OMI tropospheric lightning NO_2 columns at ~18:30 UTC on 30 May 2012. The color scale ranges from -3.0 (blue) to +3.0 (red) $\times 10^{15}$ molecules cm^{-2}.

(a)   (b)
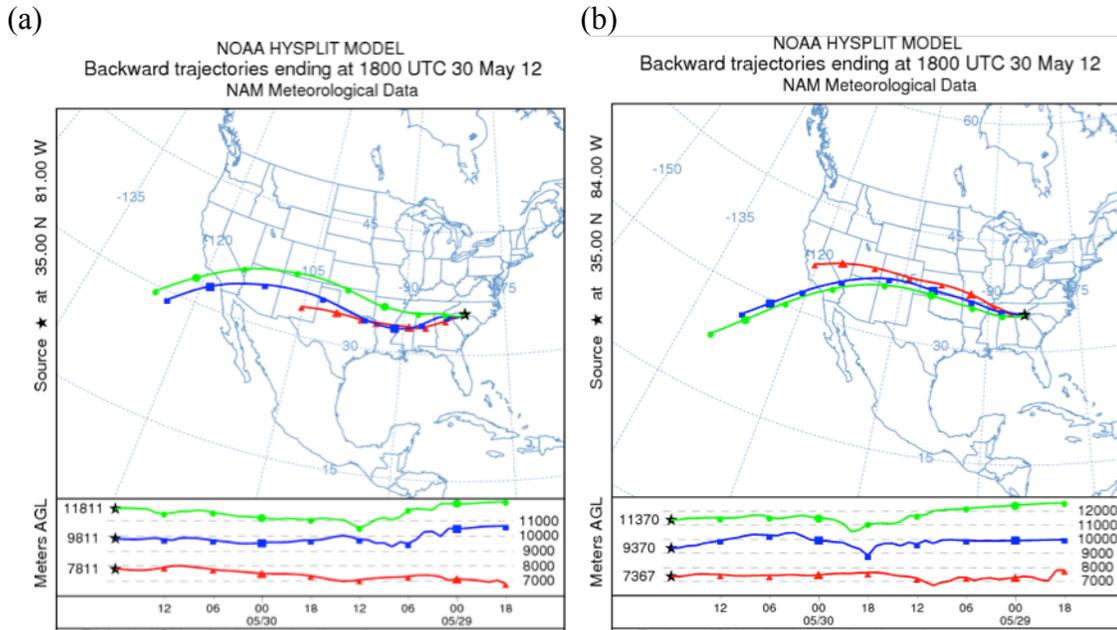
Figure 46. Backward trajectories initiating at (a) 35 °N, 81 °W and (b) 35 °N, 84 °W within the region of enhanced LNO$_2$ at 18 UTC 30 May 2012. The trajectories start at 8 km (red), 10 km (blue), and 12 km (green) above mean sea level. (The NOAA HYSPLIT model is available at http://ready.arl.noaa.gov/HYSPLIT.php.)
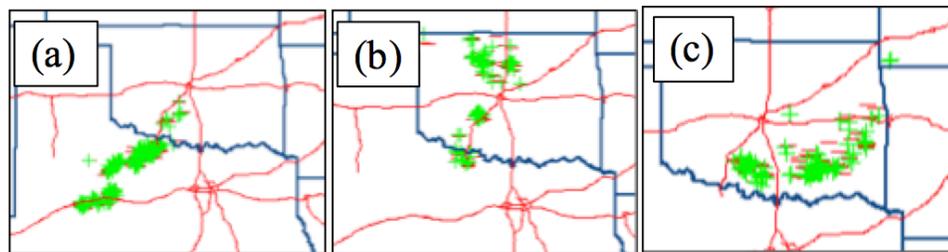
Figure 47. Location of NLDN 5-min lightning strikes at (a) 00 UTC 29 May 2012, (b) 00 UTC 30 May 2012, and 05 UTC 30 May 2012 over Oklahoma and Texas. (Available in the EOL DC3 field catalog http://catalog.eol.ucar.edu/dc3_2012/.)

Non-lightning sources were also visible in Figure 45. These included the Four

Corners Power Plant near Farmington, New Mexico, the Whitewater-Baldy fire in

southwestern New Mexico (Voiland, 2012), and agricultural burns in the Mississippi

River Valley. FLEXPART indicates elevated levels of the biomass burning tracer in the

lower troposphere in the area of the wildfire and agricultural burning (Figure 48).

133
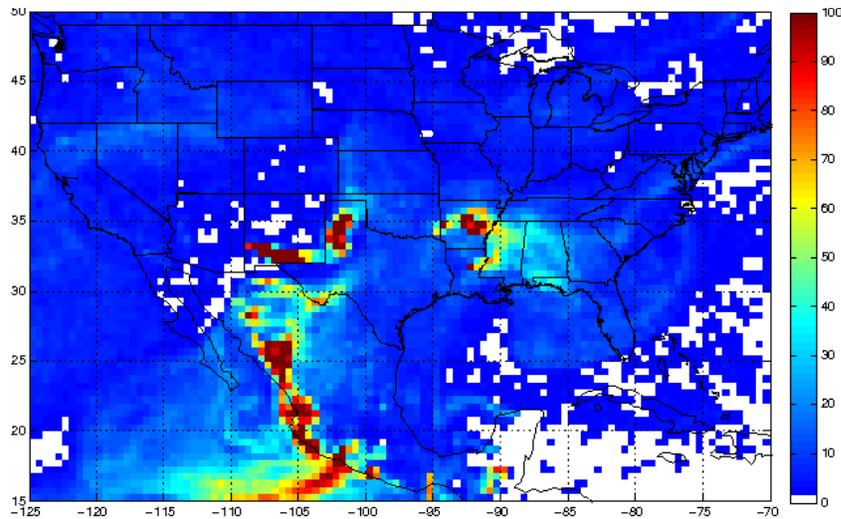
Figure 48. Forward trajectories of the biomass burning tracer in the lower troposphere from the FLEXPART dispersion model at 19 UTC 30 May 2012. Units are in ppbv. (Provided by NOAA ERSL https://www.esrl.noaa.gov/csd/groups/csd4/forecasts/dc3/.)

8.2 Aircraft observations of the convective outflow plume

Based on the satellite information and trajectories, the GV and DC8 were directed toward the southern Appalachian region on 30 May 2012 to locate and sample the convective outflow plume associated with the severe supercell system that developed along the Oklahoma/Kansas border at 21:10 UTC 29 May and moved east-southeast through Oklahoma. The aircraft set up a triangular shaped flight path from Lynchburg, Virginia, to Athens, Georgia, to Snowbird (a waypoint on the Tennessee/North Carolina border).

For the trace gas analyses, the 1-sec DC8 and GV aircraft data was averaged over 5 sec and 4 sec time intervals, respectively, to represent a 1 km × 1 km horizontal resolution based on the aircraft ground speeds. In addition, only observations within tropospheric air were included (O_3:CO ratio < 1.25; Hudman et al., 2007). Plots of the trace gas mixing ratios along the aircraft flight tracks suggest the aircraft encountered the outflow plume along the southwest-to-northeast tracks between Athens and Lynchburg.

Figures 49 and 50 show the aircraft detected NO_x mixing ratios between 1-2 ppbv at 10-12 km altitude along the southern track and the northeast corner of the triangle near Lynchburg. The CO measurements are generally above 110 ppbv within the sampling region (Figures 51 and 52); however, the portion of the track where NO_x is elevated coincides with slightly higher CO mixing ratios (120 ppbv). The DC8 observed enhanced O_3 (110-130 ppbv) between roughly 10.5-12.0 km altitude in several locations in the western half of the triangle and as it approached and exited the area (Figure 53). The GV also noticed O_3 mixing ratios between 110-130 ppbv; however, these measurements were observed between about 11.0-12.5 km altitude along the northern portion of the sampling region (Figure 54). The flight tracks appear to show that the areas with higher O_3 mixing ratios (110-130 ppbv) occurred where the NO_x < 1 ppbv, while elevated NO_x (> 1 ppbv) occurred in locations where O_3 mixing ratios slightly lower (90-110 ppbv).

The relationship between the net O_3 production rate and NO_x is a nonlinear process. Net O_3 destruction occurs at low NO_x values. As NO_x increases, the O_3 production rate also increases until the NO_x mixing ratio with peak O_3 production efficiency is reached, above which the O_3 production decreases (Monks, 2005; Schumann and Huntrieser, 2007). The aircraft observations from the downwind flight are too large to help identify what the critical NO_x threshold was on 30 May for O_3 production versus destruction; however, the observations suggest that O_3 production was more efficient when NO_x concentrations were below 1 ppbv.
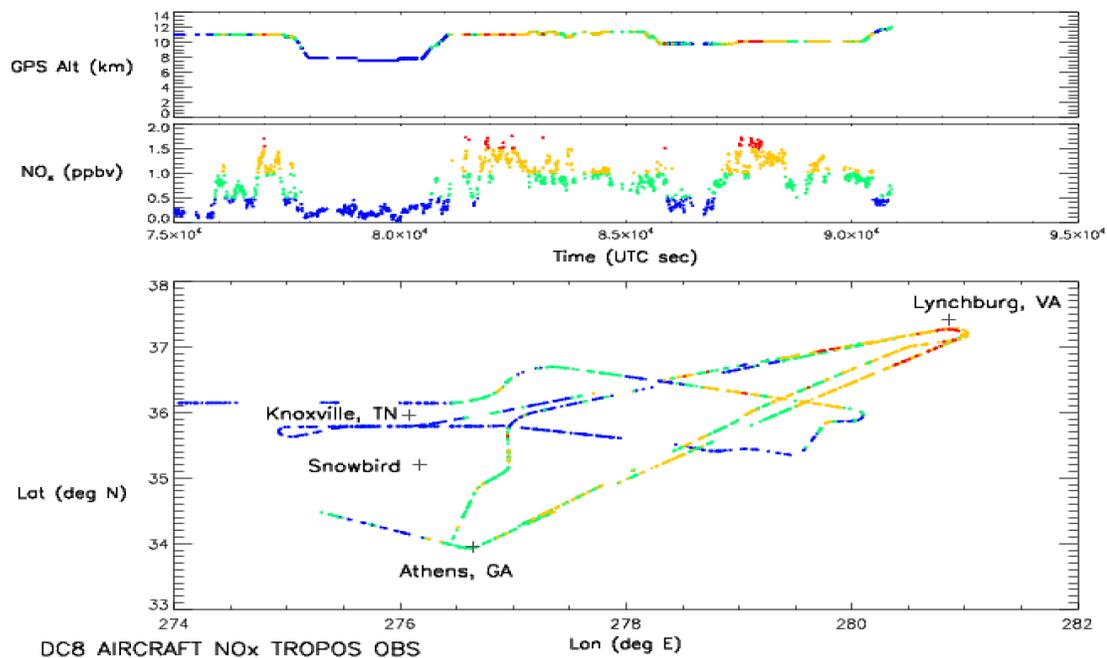
Figure 49. Tropospheric NO$_x$ mixing ratios observed along the DC8 flight track on 30 May 2012. Observations are color coded in increments of 0.5 ppbv from 0.0-2.0 ppbv, as shown in the middle panel plot.
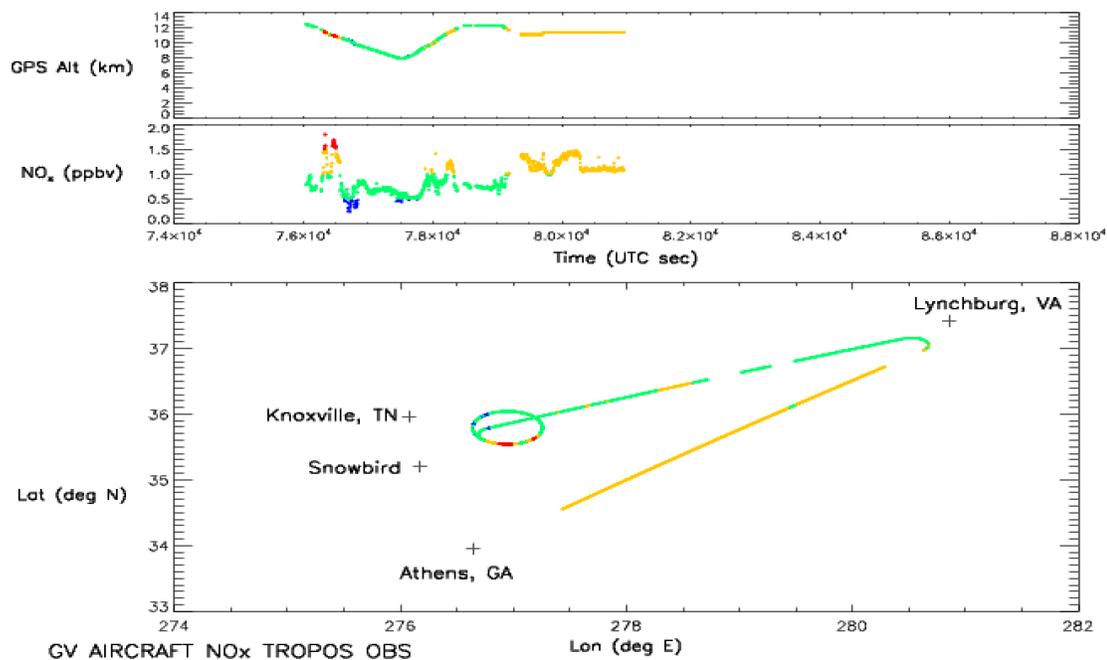
Figure 50. Tropospheric NO$_x$ mixing ratios observed along the GV flight track on 30 May 2012. Observations are color coded in increments of 0.5 ppbv from 0.0-2.0 ppbv, as shown in the middle panel plot.

136
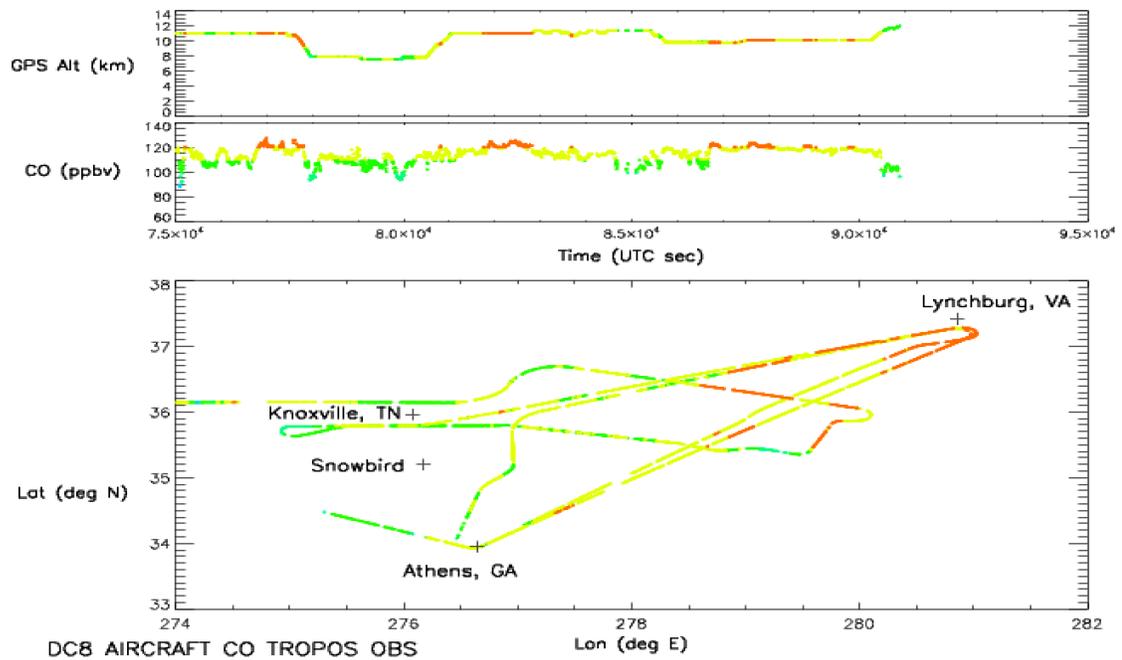
Figure 51. Tropospheric CO mixing ratios observed along the DC8 flight track on 30 May 2012. Observations are color coded in increments of 10 ppbv from 60-140 ppbv, as shown in the middle panel plot.
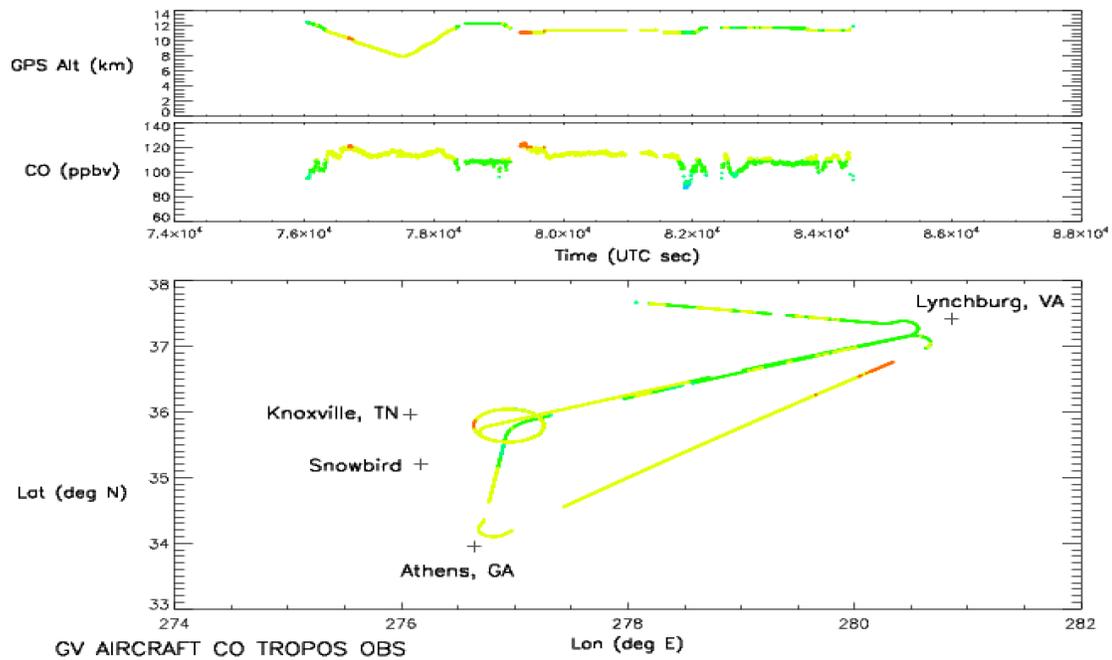
Figure 52. Tropospheric CO mixing ratios observed along the GV flight track on 30 May 2012. Observations are color coded in increments of 10 ppbv from 60-140 ppbv, as shown in the middle panel plot.
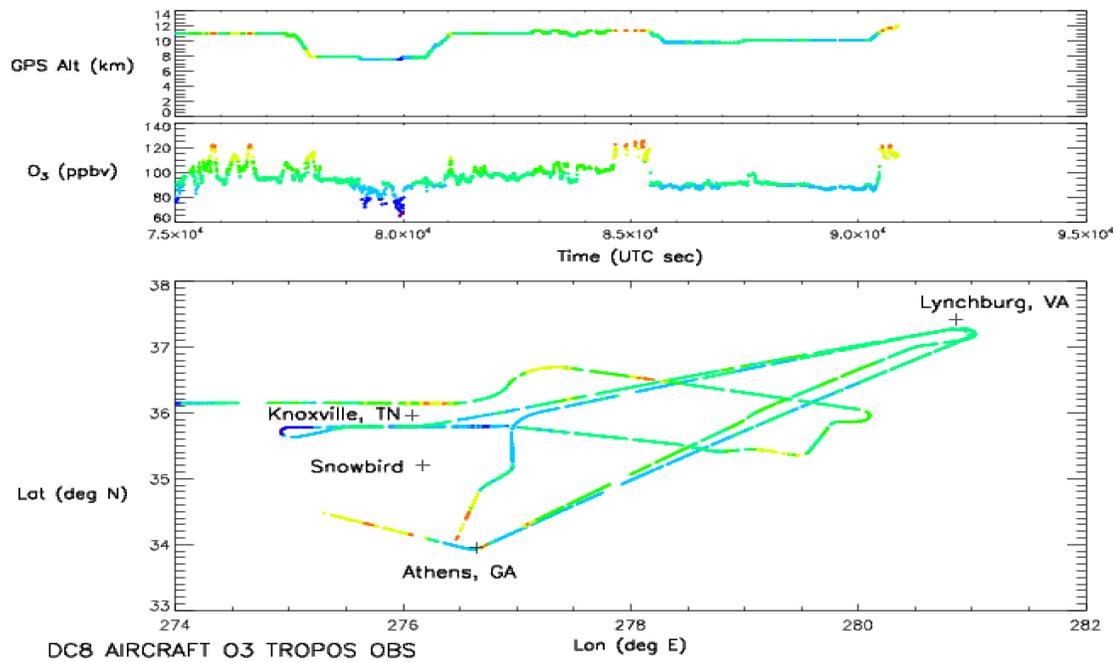
Figure 53. Tropospheric O_3 mixing ratios observed along the DC8 flight track on 30 May 2012. Observations are color coded in increments of 10 ppbv from 60-140 ppbv, as shown in the middle panel plot.
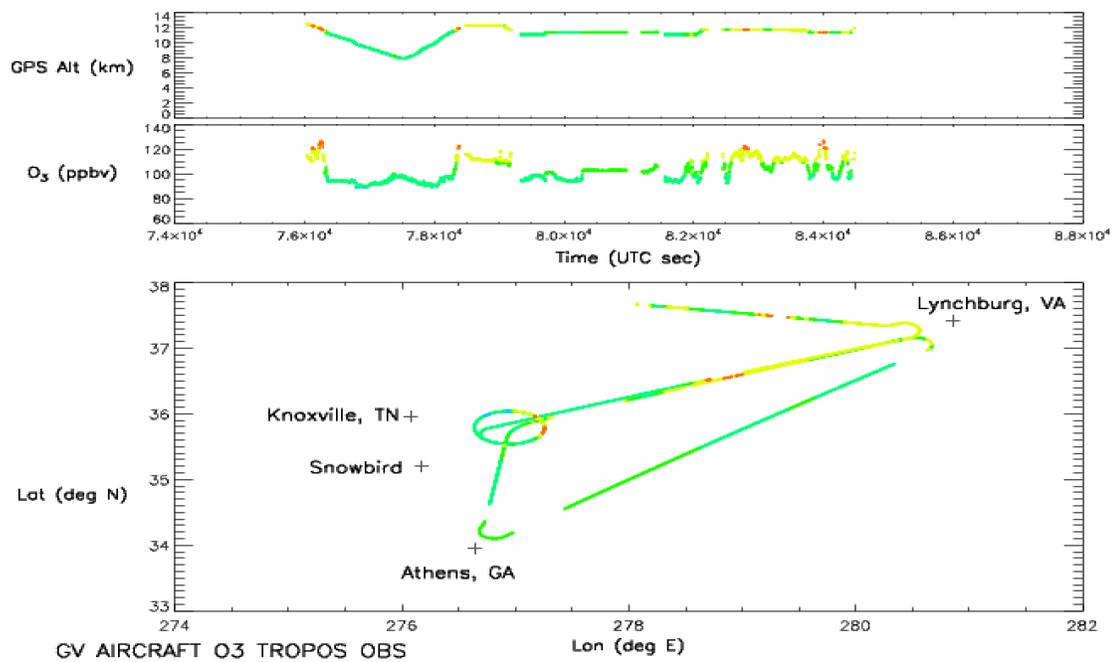
Figure 54. Tropospheric O_3 mixing ratios observed along the GV flight track on 30 May 2012. Observations are color coded in increments of 10 ppbv from 60-140 ppbv, as shown in the middle panel plot.

Figure 55 provides an example of model-derived O_3 production rates as a function of NO_x mixing ratio for the clean free troposphere. The O_3 production rate increases with increasing NO_x from roughly 0.07-0.8 ppbv and decreases with NO_x concentrations above 0.8 ppbv. According to Monks (2005), the O_3 production rate maximizes at 0.8 ppbv NO_x in the clean free troposphere (Figure 55); however, on 30 May it appears that this peak occurred at a slightly higher NO_x value (~1 ppbv) and in an upper tropospheric region influenced by convective outflow that contains enhanced HO_x and HO_x precursors (e.g., CH_2O and H_2O_2), which lead to larger O_3 production rates than for the clean free troposphere.
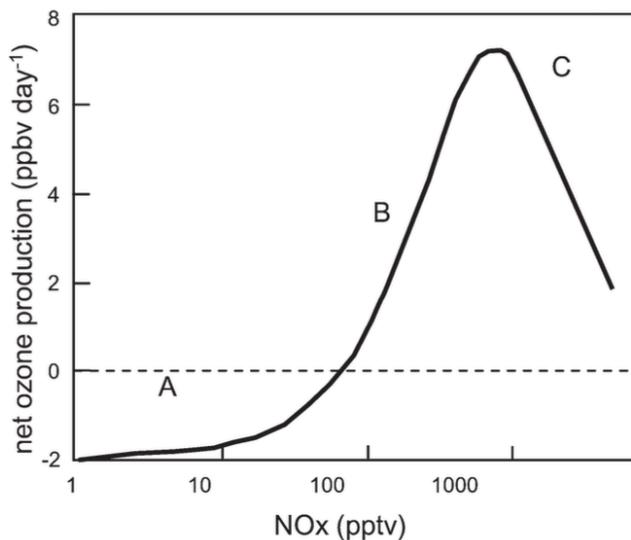
Figure 55. Schematic of the variation in net ozone production with increasing NO_x mixing ratios in the clean free troposphere (from Monks, 2005).

Figure 56 shows the mean mixing ratio profiles within tropospheric air for five trace gases measured by the aircraft over the southern Appalachian region. The CO and NO_x profiles suggest the outflow plume may extend from roughly 8-12 km; however, the mean NO_x profile appears to show the core of the plume is located between 10-12 km.

The aircraft observations suggest that the aircraft did encounter the outflow plume from the previous afternoon/evening, as indicated by the collocation of the highest NO_x and CO mixing ratios. The anti-correlation between the location of enhanced NO_x and O_3 mixing ratios suggest that may be associated with efficient O_3 production in the upper troposphere when NO_x is diluted. The aircraft observations also validate the success of the near-real-time lightning NO_2 algorithm (Pickering et al., 2014). The HYSPLIT backward trajectories also confirm the air mass within the 10-12 km layer over southern Appalachian did pass through or near the active convection.

When the aircraft sampled the anvil outflow of the active convection the previous evening, the average O_3 mixing ratio between 10.7-12.2 km altitude was 86.1 ppbv. Based on the mean O_3 profile from the downwind region in Figure 56, the average O_3 mixing ratio within this same altitude range is 105 ppbv, indicating photochemical O_3 production of 19 ppbv. The convective outflow plume experienced 12 hours of sunlight between the last time it was sampled in the anvil and the first time it was sampled in the downwind region the next day. This suggests the photochemical production rate is roughly an average of 1.6 ppbv per hour. Prior model simulations have shown O_3 enhancements of similar magnitude downwind of convection. DeCaria et al. (2005) found O_3 increased on average by 10 ppbv day^{-1} for a cloud-resolved simulation of the 12 July 1996 storm observed in Colorado during the STERAO-A campaign. More recently, analyses by Apel et al. (2015) showed O_3 increased downwind of two thunderstorms observed on 22 June 2012 in Colorado during DC3 by 11-14 ppbv over a two-day period. The O_3 enhancement observed on 30 May is likely greater than in the clean free troposphere shown by Monks (2005) because of increased HO_x and HO_x precursors in the

outflow plume over the southern Appalachians. Updrafts from the active convection the

previous afternoon/evening transported boundary layer air, which may have contained

HO_x precursors, into the upper convective region of the thunderstorms. Based on an

analysis of DC3 aircraft observations, Schroeder et al. (2014) suggest the mixing of

polluted convective outflow and stratospheric air rapidly produces OH. Three of the

stratospherically influenced samples in the Schroeder et al. (2014) analysis were from the

29-30 May convective event. The presence of these additional trace gases would have

aided in producing more O_3 in the downwind plume on 30 May than would be present in

the background air.
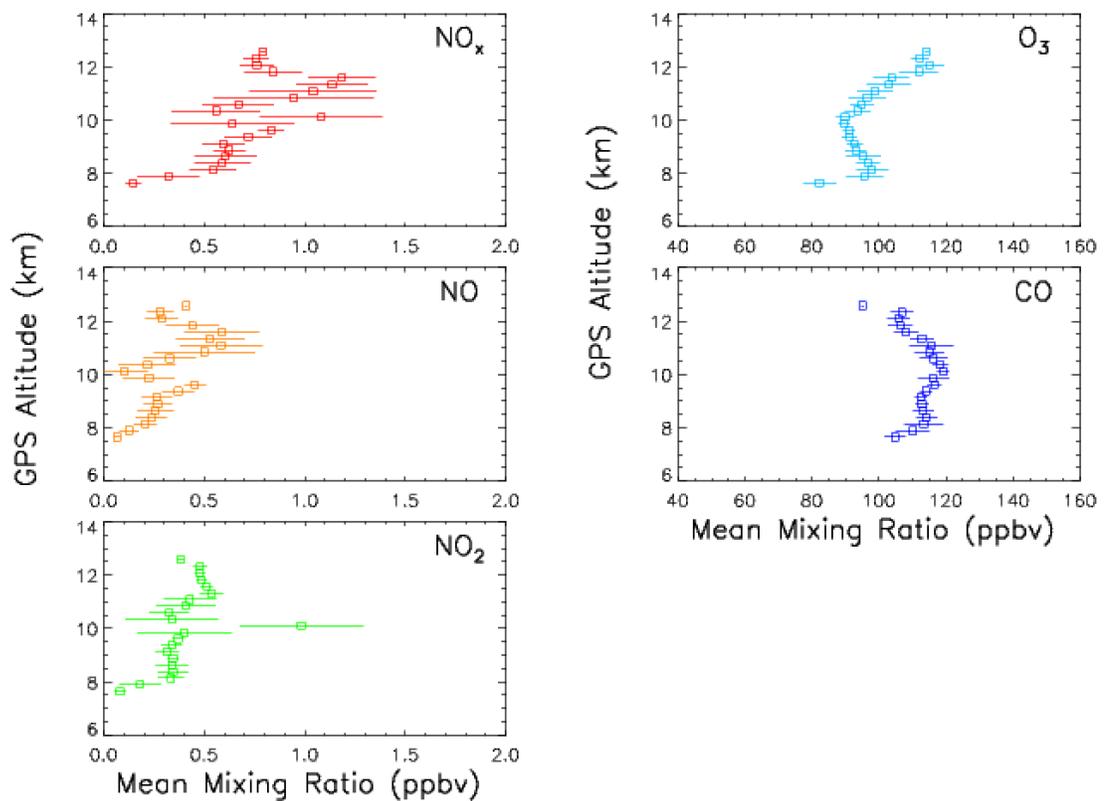
Figure 56. Mean trace gas mixing ratios based on DC8 and GV observations taken over
the southern Appalachian region within tropospheric air on 30 May 2012. Each
horizontal line represents ±1 standard deviation.

8.3 LNO$_x$ column and storm flux comparison

The mean partial NO$_2$ column (400-150 hPa) calculated for the southern Appalachian

region based on the aircraft observations is 1.59×10^{15} molecules cm^{-2} (Pickering et al.,

2014). To determine the total moles of NO$_x$ within this area, the pressure-weighted mean

NO$_x$:NO$_2$ ratio (1.9) is calculated from the mean profiles in Figure 56 and used to find the

partial NO$_x$ column (3.05×10^{15} molecules cm^{-2}). By accounting for the area of the

triangular flight track region (34,000 km^2), the column content is converted to a total NO$_x$

content of 1.72×10^6 moles. A similar calculation is performed using the mean partial

OMI LNO$_2$ column estimate (Pickering et al., 2014), which suggests the partial LNO$_x$

column is 2.26×10^{15} molecules cm^{-2}. Given the area of the sampling region, the total

LNO$_x$ estimate based on OMI data is 1.27×10^6 moles. OMI LNO$_2$ estimates have

significant uncertainty. However, comparison of OMI LNO$_x$ with the aircraft total NO$_x$

suggests that roughly 75% of the NO$_x$ in the downwind region is due to lightning.

Over the lifetime of the 29-30 May severe supercell system, approximately

31,633 total lightning flashes were observed. Using the NO$_x$ production per flash

determined by the cloud-resolved WRF-Chem simulation (82 moles), this would imply

2.59×10^6 moles were produced by this event. If it is assumed all of the LNO$_x$ in the

downwind region (1.27×10^6 moles) came from the observed supercell system, then this

suggests roughly half of the LNO$_x$ generated by the convection was lost chemically

during transport. However, it is likely that not all of the LNO$_x$ produced in the storm

exited the anvil. A slightly lower percentage of LNO$_x$ loss due to chemistry during

transport (34%) was found when the average anvil outflow LNO$_x$ fluxes estimated by

Pollack et al. (2016) for each anvil transect were considered. Using the average LNO$_x$

fluxes, the moles LNO_x exiting in the anvil outflow were calculated over the length of each aircraft transect. Between the times when visible satellite first showed the anvil becoming elongated (~22:00 UTC) and the first anvil transect (23:13 UTC), only half of the LNO_x flux observed during the first aircraft transect was used. For the time period between the last anvil transect and the end of the convective event (00:41-04:20 UTC), only half of the LNO_x flux observed during the last transect was considered. This approach suggests 74% or 1.91×10^6 moles LNO_x were advected out of the anvil during the lifetime of the 29-30 May convective event and 66% of this amount was observed in the downwind region. If true, this indicates the severe supercell system had a major impact on the upper tropospheric chemistry in the downwind environment.

However, regions of enhanced LNO_x may not be formed by one convective event or be entirely composed of LNO_x. Active convection in Alabama occurred early on 30 May, which influenced the area of enhanced LNO_x (Pickering et al., 2014). In addition, boundary layer NO_x can be carried into a storm by convective updrafts and carried away with the outflow, or NO_x from the free troposphere can be entrained into the convective plume by turbulent mixing.

CHAPTER 9: SUMMARY AND CONCLUSIONS

Lightning is dependent on updraft intensity and the hydrometeors in the mixed-phase region of a convective cloud. Therefore, it is necessary that the inputs to FRPSs from a simulation accurately represent the kinematic and microphysical characteristics of the observed storm. Eighteen FRPSs were evaluated based on their performance in a cloud-resolved simulation of the 29-30 May 2012 severe supercell system that was observed in Oklahoma by ground-based and airborne measurements during DC3. The observed storm location, dimensions, and vertical motion are represented reasonably well by the WRF model prior to and with the convective damping and LDA assumptions. However, the damping and LDA improve the microphysics by providing a better representation of the anvil area and slightly reducing the maximum altitude and value of the graupel mixing ratio. The model storm initiation is delayed 1-hr compared with observations; however, the simulated radar reflectivity and flash rates indicate this offset is not maintained and ranges from 30-50 minutes as the storm evolves. To further improve the model-simulated hydrometeors' mixing ratio and vertical extent, altitude-specific scaling factors derived by comparison of the model output with DLA proxy observations are applied during the simulation to the hydrometeors in the FRPS code (i.e., the hydrometeors were not adjusted in the microphysics scheme), thereby adjusting the hydrometeors closer to the observations. These steps highlight the dependency FRPSs have on the proper representation of storm parameters in models.

The damping and LDA, along with scaling hydrometeors to proxy observations, provided the best results for modifying the hydrometeors. This allowed for the most

representative FRPS to be selected for this model set up. The scheme most similar to the observed flash rate trends and total number of flashes during the storm is based on ICEFLUX (Finney et al., 2014). The UAH UV scheme (Carey et al., 2015) provided the best comparison to the observations of any non-hydrometeor scheme. These results are described in Cummngs et al. (2017a).

Using the ICEFLUX scheme, ten WRF-Chem simulations are run to investigate the mean LNO_x production per flash and the transport and distribution of other trace gases for the 29-30 May 2012 convective event (Cummings et al., 2017b). The simulations included one run with no lightning chemistry and nine runs with different LNO_x production scenarios. A comparison of the aircraft and model-simulated CO and O_3 mixing ratios indicates the convective transport is slightly underestimated in the model. To compensate for the transport underestimate, one model layer below each layer the aircraft flew within was analyzed. This adjustment showed the model-simulated CO and O_3 mixing ratios are within 1% and 3% of the aircraft observations, respectively.

With lightning chemistry turned off in the model, the overall mean NO_x from the four model layers the aircraft flew in is underestimated by ~55%. A comparison of the aircraft and model-simulated NO_x mixing ratios from the nine different LNO_x production scenarios suggested 82 moles flash^{-1} achieved a best match within 5% of the observations. This estimate is roughly three times smaller than the mean 250 moles NO flash^{-1} calculated by Schumann and Huntrieser (2007) from a survey of the literature which included theoretical estimates, and values derived from laboratory studies, field data, and cloud-resolved model simulations from 1976-2007; however, the value I derived for the May 29-30 DC3 storm is within the lower end of the range of estimates

(33-660 moles fl^{-1}) reported by Schumann and Huntrieser. My estimate for the observed

storm is also six times smaller than the mean value suggested by Ott et al. (2010) for

midlatitude and subtropical storms (500 moles fl^{-1}). The observed vertical wind shear

between the anvil outflow and steering level (~700 hPa) for the 29-30 May severe

supercell system (24 m s^{-1}) suggests longer flashes and larger LNO_x production than

tropical and subtropical convection (67-391 moles $flash^{-1}$); however, despite the strong

shear, this is a high flash rate event with small flash extents (~6.5 km), which suggests

the vertical wind shear is not the dominant influence on the LNO_x production for this

case.

Four of the LNO_x production scenarios investigated the use of default model

parameters for the fractional CG and IC flash channel vertical profiles (DeCaria et al.,

2000) and IC:CG ratios (Boccippio et al., 2001) versus the use of observed data based on

my model modifications. The model parameter that had a greater influence on the mean

NO_x mixing ratio in the anvil outflow for this convective event was the vertical

distributions. With the default profiles the CG LNO_x peaks below the altitude at which it

maximizes in the observed storm and the lower IC LNO_x peak does not exist. This

causes the LNO_x to be emitted lower in the troposphere and not be as close to the altitude

of the anvil outflow as is the case with the observed profiles. The default vertical profiles

caused the model to underestimate the observed NO_x in the anvil outflow by < 20%,

despite using a higher LNO_x production scenario (125 moles NO $flash^{-1}$) than the final

scenario that was selected (i.e., 82 moles $flash^{-1}$ and the observed model parameters).

A weak positive correlation was found between LNO_x production and the total

flash area over several DC3 storms (Pollack et al., 2016). My analysis of a more

meaningful relationship between LNO_x production and mean flash area over the several storms (including the May 29-30 case) yielded a somewhat more moderate correlation. When combined with the moderate negative correlation found between the total flash rate in the observed 29-30 May severe supercell system and flash extent ($r = -0.69$) or energy per flash ($r = -0.70$), it is possible that a new parameterization scheme may be developed to estimate LNO_x production as a function of time from the flash rate in models.

One of the goals in DC3 was to be able to measure changes in the composition and chemistry of the upper troposphere by taking measurements of the same convective outflow while the storm is active and 12-48 hours downwind. Based on aircraft observations, roughly 19 ppbv of O_3 was produced by photochemical reactions during the outflow plume's transit to the southern Appalachian region. While this photochemical production is higher than prior estimates (DeCaria et al., 2005; Apel et al., 2015), the influence of LNO_x from nearby convection in Alabama may have played a role in the O_3 production in this downwind region.

DC3 provided a unique opportunity to use observations from ground-based, upper air, and remote sensing instrumentation to further investigate the role lightning and lightning chemistry have on the composition of the upper troposphere both during and following convection. It is also providing greater detail on lightning characteristics (e.g., flash extent and energy), which can be used to better understand LNO_x production, better parameterize it in models of all scales, and reduce the uncertainty in the global LNO_x budget.

CHAPTER 10: FUTURE WORK

Upon completion of my PhD I intend to apply the knowledge I gained from my graduate school research experience toward bridging the gap between research and operational forecasting and to continue furthering the atmospheric chemistry community's interest in LNO_x, climate, and air quality. Sections 10.1 and 10.2 provide a brief overview of this continued work. However, there are several areas where additional research related to the application of FRPSs and the relationship between lightning and LNO_x production should be explored. Section 10.3 discusses these topics.

10.1 The DC3 6-7 June 2012 Colorado convective event

The 6-7 June 2012 Colorado convective event is a highly desired case to analyze because of the excellent coverage provided by ground-based (i.e., LMA and radar), upper air, and aircraft observations. The synoptic situation indicated the development of afternoon convection over northeast Colorado with an approaching cold front from the northwest and a shortwave trough moving along a ridge of high pressure over the Central Plains. An important meteorological feature that developed that afternoon was an area of low-level convergence, known as the "Denver Cyclone" (Wilczak and Glendening, 1988; Wilczak and Christian, 1990; Vu et al., 2016).

A significant amount of time was spent trying to select the best model domain set-up, initialization conditions, and physics schemes to simulate the observed convection. Each combination that was evaluated is provided in Table 14. Overall, the size and features of the convection were not satisfactory. The NEXRAD indicated a convective line oriented from the southwest to northeast, which became more north-to-south oriented

with time. The model simulations predicted a convective line that was either tilted more toward the southwest or oriented from north-to-south. Several set-ups also produced multiple lines of convection (i.e., NARR) or the convection was delayed and had more emphasis on the southern portion of the line (i.e., ECMWF). However, in each simulation the stratiform and anvil areas became larger than the observations soon after the convection began to develop, with cells that were not as individualized and radar reflectivities > 30 dBZ that covered a larger area. The maximum radar reflectivities were also lower than the observed. Convective damping (Li et al., 2017) and LDA (Fierro et al., 2012) methods were evaluated, but the model-simulated reflectivity was fairly similar to the previous WRF runs that did not employ these techniques.

A closer analysis of the meteorological source data showed the GFS and NARR lacked the surface mesoscale circulation pattern of the "Denver Cyclone" and the NAM-ANL and ECMWF were lacking the north-northwesterly winds of the low-level circulation between Denver and the Front Range. This difference in the low-level wind pattern may explain part of the variation between the simulated and observed convection.

The real-time 12 UTC NCAR WRF 3 km forecast used during the DC3 field campaign provided a good representation of the convection observed over the Colorado domain on 6-7 June, as well as its timing. While the forecast was run with the Morrison two-moment microphysics and YSU PBL schemes, it was also initialized using the 15 km Data Assimilation Research Testbed (DART) ensemble run. Based on the results from the WRF simulations evaluated in Table 14, further testing is suggested, especially using the real-time output from the DC3 forecasts.

Table 14. WRF model physics options evaluated for 6-7 June 2012 Colorado convective event.

WRF Model Physics Options	Simulation Set-ups											
INITIALIZATION TIME												
12 UTC	×	×	×	×								
18 UTC					×	×	×	×	×	×	×	×
DOMAINS												
Single (1 km horizontal resolution, 421×481 grids)	×	×	×									
Single (1 km horizontal resolution, 655×721 grids)				×								
Parent (3 km horizontal resolution, 700×735 grids); Nested (1 km horizontal resolution, 900×972 grids)					×	×	×	×				
Parent (3 km horizontal resolution, 500×464 grids); Nested (1 km horizontal resolution, 813×771 grids)										×	×	×
INITIAL/BOUNDARY CONDITIONS												
NAM-ANL (12 km, 6-hr)				×	×	×	×	×	×	×	×	×
ECMWF (6-hr)		×										
NARR (3-hr)	×											
GFS (6-hr)			×									
MICROPHYSICS SCHEMES												
Morrison two-moment	×	×	×	×	×	×		×		×	×	
Thompson							×					
NSSL two-moment									×			×
PLANETARY BOUNDARY LAYER SCHEMES												
YSU	×	×	×	×	×	×	×		×	×	×	×
MYJ								×				
CONVECTIVE DAMPING											×	×
LIGHTNING DATA ASSIMILATION											×	×

10.2 Flash rate parameterization schemes for the Florida Space Coast

Florida is the lightning capital of the United States. Its irregular coastlines, inland bodies of water, and land-water thermal contrasts help support the development of mesoscale boundaries involved in convective initiation (Hodanish et al., 1997; Lericos et al., 2002). KSC/CCAFS are located on the eastern edge of "lightning alley, " which stretches across central Florida (Roeder et al., 2014). At these facilities, lightning safety is of the utmost importance because employees and vehicles are exposed daily to rapidly changing weather. Therefore, forecasting the onset and termination of lightning is critical from an operational and safety standpoint. However, the difficulty and uncertainty in forecasting lightning cessation is costly to KSC/CCAFS, both financially and in delaying outdoor work required for readying space vehicles and payloads for launch (Roeder and Glover, 2005). Previous research has generally concentrated on lightning initiation forecasts (e.g., Gremillion and Orville, 1999; Wolf, 2006; Roeder and McNamara, 2011; Woodard et al., 2012). A few studies have investigated lightning cessation, but they only focused on observational data (e.g., Stano et al., 2010; Preston and Fuelberg, 2015; Davey and Fuelberg, 2017). I plan to build on this work and help improve the current guidelines used in terminating a lightning advisory by using a cloud-resolved model with FRPSs.

In April-June 2017, aircraft flights will be conducted to validate instrument performance onboard the GOES-R satellite (now NOAA's GOES-16 satellite), including the GLM, which was launched in November 2016 (Padula and Goodman, 2016). The NASA ER-2 aircraft will be used to conduct these flights over regions equipped with LMAs. One of these areas is KSC/CCAFS, which has a dense network of ground-based meteorological instrumentation, including several lightning detection networks. Onboard

the aircraft is instrumentation used to optically detect lightning and remotely sense trace gases (e.g., NO_2).

Assuming a convective event occurs over or within range of the KSC/CCAFS ground-based instrumentation (e.g., local lightning detection networks and radar) during the GOES-R validation mission, a cloud-resolved thunderstorm simulation will be performed and the results will be compared with surface, upper air, and aircraft observations. NASA's Applied Meteorology Unit (AMU) has tuned the NCAR Advanced Research WRF (WRF-ARW) to develop a local mesoscale model that is representative of the meteorological environment in and around KSC/CCAFS (Watson, 2013). This local model will be used to incorporate and evaluate FRPSs for the Florida Space Coast and will help identify the best FRPS(s) for the case study.

The cloud-resolved thunderstorm analysis will also be expanded to include all types of convection (e.g., single cell and multicell), as well as storms with low and high flash counts. If different schemes are more appropriate for certain flow regimes, thunderstorm types, seasons, etc., this information will be critical when implementing the FRPSs into the local mesoscale model and also for forecasting lightning cessation. This research would also benefit local operational forecasters (e.g., United States Air Force's 45th Weather Squadron) and allow for the testing of FRPSs in an environment (i.e., subtropics) other than the midlatitude (Barthe and Barth, 2008; Barthe et al., 2010; Cummings et al., 2017a) and tropical (Cummings et al., 2013) regions where FRPSs have previously been evaluated in cloud-resolved simulations.

10.3 Additional investigations stemming from the dissertation research

Based on the performance of the 18 FRPSs in the 29-30 May case study, there are several aspects of the FRPS application in cloud-resolved models that need to be explored further. First, as new FRPSs are developed or evolve, the schemes should be assessed using the same set of convective events and same model configuration for evaluation. These events should represent thunderstorms of varying type, severity, location, and flash rates. A complex set of cases will help validate a FRPS's performance by ensuring the scheme is performing as intended when applied in a model set-up and by testing the limits of its application. Similar intercomparison studies have been performed in the past using specific weather phenomena (e.g., 10 July 1996 STERAO-A storm) to investigate the performance of LNO_x parameterization schemes (Barth et al., 2007), FRPSs (Barthe et al., 2010), and microphysics schemes (Morrison et al., 2015). This evaluation process will allow for a better understanding of the performance of each FRPS, especially when the schemes are tested on a new convective event.

Second, the FRPS equations are applied to each model processor within the model domain for this case study. Sensitivity studies should be performed to explore how the number of model processors used may modify the model-simulated flash counts, especially when the equations are nonlinear or linear with non-zero y-intercepts, and if there is a better way to apply the FRPSs in online simulations versus using model output to perform the calculations offline. Also, identification of limitations for the horizontal and vertical resolutions at which FRPSs can be applied would also be beneficial. For example, are flash rates significantly overestimated when a 1 km x 1 km horizontal

153

resolution is used because that resolution resolves storm features (e.g., vertical velocity and hydrometeors) more finely than was the case when the scheme was developed?

Another topic that requires additional investigation is the potential aerosol effects on flash rates. As the nine different LNO_x production scenarios were evaluated in WRF-Chem, the simulated flash rate time series varied. While the GOCART aerosol scheme used in the model simulation of the 29-30 May case study is connected to the radiation schemes in WRF-Chem, it is not connected with the cloud microphysics schemes and does not contain the nitrate aerosol. Therefore, a different aerosol scheme, which offers these features (e.g., the Model for Simulating Aerosol Interactions and Chemistry (MOSAIC)), should be used to further examine the potential influence the changes in NO_x due to lightning have on aerosol concentrations (e.g., nitrates and sulfates) and storm microphysics and kinematics. Any potential relationships will be especially important for chemistry-climate simulations and will further strengthen the need to reduce uncertainty in the global LNO_x budget.

Finally, my results suggest the development of a parameterization scheme that determines LNO_x production per flash based on flash rate may be possible; however, this is based on a small sample size, which showed a weak to moderate positive correlation between mean flash area and LNO_x production per flash. A larger dataset needs to be constructed and also focus on data within the LMA network's 3D coverage where the detection efficiency is highest. This is important for accurately capturing the flash extent and area, since flash size may become distorted as the distance from the network increases.

REFERENCES

Adams-Selin, R. D., S. C. van den Heever, and R. H. Johnson (2013), Impact of graupel parameterization schemes on idealized bow echo simulations, *Mon. Wea. Rev.*, 141, 1241-1262, doi:10.1175/MWR-D-12-00064.1.

Allen, D. J., and K. E. Pickering (2002), Evaluation of lightning flash rate parameterizations for use in a global chemical transport model, *J. Geophys. Res.*, 107(D23), 4711, doi:10.1029/2002JD002066.

Allen, D., K. Pickering, B. Duncan, M. Damon (2010), Impact of lightning NO emissions on North American photochemistry as determined using the Global Modeling Initiative (GMI) model, *J. Geophys. Res.*, 115, D22301, doi:10.1029/2010JD014062.

Allen, D. J., K. E. Pickering, R. W. Pinder, B. H. Henderson, K. W. Appel, and A. Prados (2012), Impact of lightning-NO on eastern United States photochemistry during the summer of 2006 as determined using the CMAQ model, *Atmos. Chem. Phys.*, 12, 1737-1758, doi:10.5194/acp-12-1737-2012.

Apel, E. C., et al. (2015), Upper tropospheric ozone production from lightning NO_x-impacted convection: Smoke ingestion case study from the DC3 campaign, *J. Geosphy. Res. Atmos.,* 120, 2505-2523, doi:10.1002/2014JD022121.

Banerjee, A., A. T. Archibald, A. C. Maycock, P. Telford, N. L. Abraham, X. Yang, P. Braesicke, and J. A. Pyle (2014), Lightning NOx, a key chemistry-climate interaction: Impacts of future climate change and consequences for tropospheric oxidising capacity, *Atmos. Chem. Phys.,* 14, 9871-9881, doi:10.5194/acp-14-9871-2014.

Barth, M. C., S.-W. Kim, W. A. Skamarock, A. L. Stuart, K. E. Pickering, and L. E. Ott (2007), Simulations of the redistribution of formaldehyde, formic acid, and peroxides in the 10 July 1996 Stratospheric-Tropospheric Experiment: Radiation, Aerosols, and Ozone deep convection storm, *J. Geophys. Res., 112*, D13310, doi:10.1029/2006JD008046.

Barth, M. C., et al. (2015), The Deep Convective Clouds and Chemistry (DC3) field campaign, *Bull. Amer. Meteor. Soc.,* 96, 1281-1309, doi:10.1175/BAMS-D-13-00290.1.

Barthe, C., and M. C. Barth (2008), Evaluation of a new lightning-produced NOx parameterization for cloud resolving models and its associated uncertainties, *Atmos. Chem. Phys.*, 8, 4691-4710, doi:10.5194/acp-8-4691-2008.

Barthe, C., G. Molinié, and J.-P. Pinty (2005), Description and first results of an explicit electrical scheme in a 3D cloud resolving model, *Atmos. Res.*, 76, 95-113, 2005.

Barthe, C., W. Deierling, and M. C. Barth (2010), Estimation of total lightning from various storm parameters: A cloud-resolving model study, *J. Geophys. Res.*, 115, D24202, doi:10.1029/2010JD01445.

Basarab, B. M. (2015), Prediction of total lightning in Colorado and Alabama thunderstorms based on storm dynamical and microphysical variables, M.S. thesis, 93 pp., Dep. of Atmos. Sci., Colorado State Univ., Fort Collins, Colorado. [Available at http://hdl.handle.net/10217/166859.]

Basarab, B. M., S. A. Rutledge, and B. R. Fuchs (2015), An improved lightning flash rate parameterization developed from Colorado DC3 thunderstorm data for use in cloud-resolving chemical transport models, *J. Geophys. Res. Atmos.*, 120, 9481-9499, doi:10.1002/2015JD023470.

Bela, M. M., M. C. Barth, O. B. Toon, A. Fried, C. R. Homeyer, H. Morrison, K. A. Cummings, Y. Li, K. E. Pickering, D. J. Allen, et al. (2016), Wet scavenging of soluble gases in DC3 deep convective storms using WRF-Chem simulations and aircraft observations, *J. Geophys. Res. Atmos.*, 121, 4233-4257, doi:10.1002/2015JD024623.

Blakeslee, R., and W. Koshak (2016), LIS on ISS: Expanded global coverage and enhanced applications, *The Earth Observer*, 28(3), 4-14. [Available at https://eospso.gsfc.nasa.gov/sites/default/files/eo_pdfs/May_June_2016_color%20508.pdf]

Blakeslee, R. J., et al. (2014), Lightning Imaging Sensor (LIS) for the International Space Station (ISS): Mission description and science goals, paper presented at *XV International Conference on Atmospheric Electricity*, Norman, OK.

Boccippio, D. J., K. L. Cummins, H. J., Christian, and S. J. Goodman (2001), Combined satellite- and surface-based estimation of the intracloud-cloud-to-ground lightning ratio over the continental United States, *Mon. Wea. Rev.*, 129, 108-122.

Boersma, K. F., et al. (2011), An improved tropospheric NO2 column retrieval algorithm for the Ozone Monitoring Instrument, *Atmos. Meas. Tech.*, 4, 1905-1928, doi:10.5194/amt-4-1905-2011.

Bond, D. W., R. Zhang, X. Tie, G. Brasseur, G. Huffines, R. E. Orville, and D. J. Boccippio (2001), NO_x production by lightning over the continental United States, J. Geophys. Res., 106, doi:10.1029/2000JD000191.

Bruning, E. (2014a), OKLMA HDF5 Flash Data and NetCDF Grids. Version 1.0. UCAR/NCAR-Earth Observing Laboratory. http://data.eol.ucar.edu/dataset/353.202. Accessed 03 Mar 2017.

Bruning, E. (2014b), COLMA HDF5 Flash Data and NetCDF Grids. Version 1.0. UCAR/NCAR-Earth Observing Laboratory. http://data.eol.ucar.edu/dataset/353.203. Accessed 03 Mar 2017.

Bruning, E. C., and D. R. MacGorman (2013), Theory and observations of controls on lightning flash size spectra, *J. Atmos. Sci.,* 70, 4012-4029,doi:10.1175/JAS-D-12-0289.1.

Bruning, E. C., and R. J. Thomas (2015), Lightning channel length and flash energy determined from moments of the flash area distribution, *J. Geophys. Res. Atmos.,* 120, 8925-8940, doi:10.1002/2015JD023766.

Bryan, G. H., and H. Morrison (2012), Sensitivity of a simulated squall line to horizontal resolution and parameterization of microphysics, *Mon. Wea. Rev.*, 140, 202-225, doi:10.1175/MWR-D-11-00046.1.

Buechler, D. E., W. J. Koshak, H. J. Christian, and S. J. Goodman (2014), Assessing the performance of the Lightning Imaging Sensor (LIS) using deep convective clouds, *Atmos. Res.*, 135-136, 397-403, doi:10.1016/j.atmosres.2012.09.008.

Carey, L. D., and S. A. Rutledge (1996), A multiparameter radar case study of the microphysical and kinematic evolution of a lightning producing storm, *Meteorol. Atmos. Phys.*, 59, 33-64, doi:10.1007/BF01032000.

Carey, L. D., A. L. Bain, and R. Mathee (2014), Kinematic and microphysical control of lightning in multicell convection over Alabama during DC3, paper presented at 23rd International Lightning Detection Conference/5th International Lightning Meteorology Conference, Intl. Lightning Meteorolog. Conf., Tucson, Ariz., 18-21 March.

Carey, L. D., E. V. Schultz, C. J. Schultz, A. L. Bain, R. M. Mecikalski, W. Deierling, W. A. Petersen, and K. E. Pickering (2015), Kinematic and microphysical control of lightning flash rate over northern Alabama, Proc. Seventh Conference on the Meteorological Applications of Lightning Data, 95th Annual Meeting, AMS, Phoenix, AZ, 4-8 Jan.

Cecil, D. J., D. E. Buechler, and R. J. Blakeslee (2014), Gridded lightning climatology from TRMM-LIS and OTD: Dataset description, *Atmos. Res.*, 135-136, 404-414, doi:10.1016/j.atmosres.2012.06.028.

Chameides, W. L., D. H. Stedman, R. R. Dickerson, D. W. Rusch, and R. J. Cicerone (1997), NO_x production in lightning, *J. Atmos. Sci.*, 34, 143-149.

Chin, M., R. B. Rood, S.-J. Lin, J. F. Muller, and A. M. Thompson (2000), Atmospheric sulfur cycle in the global model GOCART: Model description and global properties, *J. Geophys. Res.*, 105, 24671-24687.

Choi, Y., J. Kim, A. Eldering, G. Osterman, Y. L. Yung, Y. Gu, and K. N. Liou (2009), Lightning and anthropogenic NO_x sources over the United States and the western North Atlantic Ocean: Impact on OLR and radiative effects, *Geophys. Res. Lett.,* 36, L17806, doi:10.1029/2009GL039381.

Chmielewski, V. C., and E. C. Bruning (2016), Lightning mapping array flash detection performance with variable receiver thresholds, *J. Geophys. Res. Atmos.*, 121, doi:10/1002/2016JD025159.

Christian, H. J., R. J. Blakeslee, D. J. Boccippio, W. L. Boeck, D. E. Buechler, K. T. Driscoll, S. J. Goodman, J. M. Hall, W. J. Koshak, D. M. Mach, and M. F. Stewart (2003), Global frequency and distribution of lightning as observed from space by the Optical Transient Detector, *J. Geophys. Res.*, 108(D1), 4005, doi:10.1029/2002JD002347.

Chronis, T. G., S. J. Goodman, D. Cecil, D. Buechler, F. J. Robertson, J. Pittman, and R. J. Blakeslee (2008), Global lightning activity from the ENSO perspective. *Geophys. Res. Lett.,* 35, doi:10.1029/2008GL034321.

Cooray, V. (2003), Geographical variability of thunderclouds, in The lightning flash, pp. 6-12, The Institution of Electrical Engineers, London, United Kingdom.

Cummins, K. L., and M. J. Murphy (2009): An overview of lightning locating systems: History, techniques, and data uses, with an in-depth look at the U.S. NLDN, *IEEE Trans. On Electromagn. Compat.*, *51*(3), 499-518, doi:10/1109/TEMC.2009.2023450.

Cummings, K. A., K. E. Pickering, M. C. Barth, and M. Weisman (2012), Application of flash rate parameterization schemes and resulting lightning NO_x production in cloud-resolved WRF forecasts, 92nd American Meteorological Society Annual Meeting, New Orleans, LA, 22-26 January 2012, 1.3.

Cummings, K. A., T. L. Huntemann, K. E. Pickering, M. C. Barth, W. C. Skamarock, H. Höller, H.-D. Betz, A. Volz-Thomas, and H. Schlager (2013), Cloud-resolving chemistry simulation of a Hector thunderstorm, *Atmos. Chem. Phys.*, 13, 2757-2777.

Cummings, K. A., et al. (2016), WRF-Chem simulations of lightning-NOx production and transport in an Oklahoma storm during DC3, 96th American Meteorological Society Annual Meeting, New Oreans, LA, 10-14 January 2016.

Cummings, K. A., et al. (2017a), Evaluation of lightning flash rate parameterization schemes in a cloud-resolved WRF simulation of the 29-30 May 2012 Oklahoma supercell storm system observed during DC3, *J. Geophys, Res.*, submitted.

Cummings, K. A., et al. (2017b), Lightning NO_x production, transport and resulting chemistry in a cloud-resolved WRF simulation of the 29-30 May 2012 Oklahoma supercell storm system observed during DC3, *J. Geophys, Res.*, in prep.

Davey, M. J., and H. E. Fuelberg (2017), Using radar-derived parameters to forecast lightning cessation for nonisolated storms, *J. Geophys. Res. Atmos.*, 122, doi:10/1002/2016JD025734.

DeCaria, A. J., K. E. Pickering, G. L. Stenchikov, J. R. Scala, J. L. Stith, J. E. Dye, B. A. Ridley, and P. Laroche (2000), A cloud-scale model study of lightning-generated NO_x in an individual thunderstorm during STERAO-A, *J. Geophys. Res.*, 105, doi:10.1029/2000JD900033.

DeCaria, A. J., K. E. Pickering, G. L. Stenchikov, and L. E. Ott (2005), Lightning-generated NO_x and its impact on tropospheric ozone production: A 3-D modeling study of a STERAO-A thunderstorm, *J. Geophys. Res.*, 110, D14303, doi:10.1029/2004JD05556.

Deierling, W. (2006), The relationship between total lightning and ice fluxes, Ph.D. dissertation, Univ. of Alabama in Huntsville, Huntsville, AL, 175 pp.

Deierling, W., and W. A. Petersen (2008), Total lightning activity as an indicator of updraft characteristics, *J. Geophys. Res.*, *113*, D16210, doi:10.1029/2007JD009598.

Deierling, W., W. A. Petersen, J. Latham, S. Ellis, and H. J. Christian (2008), The relationship between lightning activity and ice fluxes in thunderstorms, *J. Geophys. Res.*, *113*, D15210, doi:10.1029/2007/JD009700.

DiGangi, E. (2014), A study of the electrical, microphysical, and kinematic properties of the 29 May Kingfisher supercell, M.S. thesis, 106 pp., School of Meteorol., Univ. of Oklahoma, Norman, Oklahoma. [Available at http://hdl.handle.net/11244/14246.]

DiGangi, E. A., D. R. MacGorman, C. L. Ziegler, D. Betten, M. Biggerstaff, M. Bowlan, and C. Potvin (2016), An overview of the 29 May 2012 Kingfisher supercell during DC3, *J. Geophys. Res. Atmos.*, *121*, 14,316-14,343, doi:10.1002/2016JD025690.

Dolan, B., S. A. Rutledge, S. Lim, V. Chandrasekar, and M. Thurai (2013), A robust C-band hydrometeor identification algorithm and application to a long-term polarimetric radar dataset, *J. Appl. Meteor. Climatol., 52*, 2162-2186.

Earth Networks (2017), https://www.earthnetworks.com/why-us/networks/lightning/.

Emmons, L. K., S. Watlers, P. G. Hess, J.-F. Lamarque, G. G. Pfister, D. Fillmore, C. Granier, A. Guenther, D. Kinnison, T. Laepple, J. Orlando, X. Tie, G. Tyndall, C. Wiedinmyer, S. L. Baughcum, and S. Kloster (2010), Description and evaluation of the Model for Ozone and Related chemical Tracers, version 4 (MOZART-4), *Geosci. Model Dev.,* 3, 43-67.

Fehr, T., H. Höller, and H. Huntrieser (2004), Model study on production and transport of lightning-produced NO$_x$ in a EULINOX supercell storm, *J. Geophys. Res.,* 109, D09102, doi:10.1029/2003JD003935.

Fierro, A. O., J. Gao, C. L. Ziegler, K. M. Calhoun, E. R. Mansell, and D. R. MacGorman (2016), Assimilation of flash extent data in the variational framework at convection-allowing scales: Proof-of-concept and evaluation for the short-term forecast of the 24 May 2011 tornado outbreak, *Mon. Wea. Rev.,* 144, 4373–4393.

Fierro, A. O., E. R. Mansell, D. R. MacGorman, and C. L. Ziegler (2013), The implementation of an explicit charging and discharge lightning scheme within the WRF-ARW model: Benchmark simulations of a continental squall line, a tropical cyclone, and a winter storm, *Mon. Wea. Rev.*, *141*, 2390-2415, doi:10.1175/MWR-D-12-00278.1.

Fierro, A. O., E. R. Mansell, C. L. Ziegler, and D. R. MacGorman (2012), Application of a lightning data assimilation technique in the WRF-ARW model at cloud-resolving scales for the tornado outbreak of 24 May 2011, *Mon. Wea. Rev.*, 140, 2609-2627, doi:10.1175/MWR-D-11-00299.1.

Finney, D. L., R. M. Doherty, O. Wild, H. Huntrieser, H. C. Pumphrey, and A. M. Blyth (2014), Using cloud ice flux to parametrise large-scale lightning, *Atmos. Chem. Phys.*, *14*, 12665-12682, doi:10.5194/acp-14-12665-2014.

Fiore, A. M., L. W. Horowitz, E. J. Dlugokencky, and J. J. West (2006), Impact of meteorology and emissions on methane trends, 1990-2004, *Geophys. Res. Lett.,* 33, L12809, doi:10.1029/2006GL026199.

Fried, A., et al. (2016), Convective transport and scavenging of formaldehyde to the upper troposphere and lower stratosphere in thunderstorms over the central United States during the 2012 DC3 study, *J. Geophys. Res. Atmos.,* 121, 7430-7460, doi:10.1002/2015JD024477.

Fuchs, B. R., S. A. Rutledge, E. C. Bruning, J. R. Pierce, J. K. Kodros, T. J. Lang, D. MacGorman, P. Krehbiel, and W. Rison (2015), Environmental controls on storm intensity and charge structure in multiple regions of the continental United States, *J. Geophys. Res. Atmos.*, *120*, 6575-6596, doi:10.1002/2015JD023271.

Giannaros, T., V. Kotroni, and K. Lagouvardos (2015), Predicting lightning activity in Greece with the Weather Research and Forecasting (WRF) model, *Atmos. Res.,* 156, 1-13, doi:10.1016/j.atmosres.2014.12.009.

Giannaros, T. M., K. Lagouvardos, and V. Kotroni (2016), Performance evaluation of an operational lightning forecasting system in Europe, *Nat. Hazards*, doi:10.1007/s11069-016-2555-y.

Goodman, S. J., R. J. Blakeslee, W. Koshak, D. Mach, J. Bailey, D. Buechler, L. Carey, C. J. Schultz, M. Bateman, E. W. McCaul, Jr., and G. T. Stano (2013), The GOES-R Geostationary Lightning Mapper (GLM): A new eye on lightning, 93rd American Meteorological Society Annual Meeting, Austin, TX, 5-10 January 2013, TJ30.1.

Grell, G. A., S. E. Peckham, R. Schmitz, S. A. McKeen, G. Frost, W. C. Skamarock, and B. Eder (2005), Fully coupled "online" chemistry within the WRF model, *Atmos. Env.,* 39, doi:10.1016/j.atmosenv.2005.04.027.

Gremillion, M. S., and R. E. Orville (1999), Thunderstorm characteristics of cloud-to-ground lightning at the Kennedy Space Center, Florida: A study of lightning initiation signatures as indicated by the WSR-88D, *Wea. Forecasting*, 14, 640-649, doi:10.1175/1520-0434(1999)014<0640:TCOCTG>2.0.CO;2.

Gurevich, A. V., and K. P. Zybin (2005), Runaway breakdown and the mysteries of lightning, *Physics Today*, 58, 37-43.

Heckman, S., and C. Liu (2010), The application of total lightning detection for severe storm prediction, In 10th European Conference on Applications of Meteorology, Zurich, Abstract.

Helsdon Jr., J. H., G. Wu, and R. D. Farley (1992), An intracloud lightning parameterization scheme for a storm electrification model, *J. Geophys. Res.*, 97(D5), 5865-5884, doi:10.1029/92JD00077.

Heymsfield, A. J., and K. M. Miller (1988), Water vapor and ice mass transported into the anvils of CCOPE thunderstorms: Comparison with storm influx and rainout, *J. Atmos. Sci.*, 45(22), 3501-3514.

Heymsfield, A. J., and A. G. Palmer (1986), Relationships for deriving thunderstorm anvil ice mass for CCOPE storm water budget estimates, *J. Climate Appl. Meteor.*, 25, 691-702.

Hill, R. D., R. G. Rinker, H. D. and Wilson (1980), Atmospheric nitrogen fixation by lightning, *J. Atmos. Sci.,* 37, 179-192.

Hodanish, S., D. Sharp, W. Collins, C. Paxton, and R. E. Orville (1997), A 10-yr monthly lightning climatology of Florida: 1986-95, *Wea. Forecasting*, 12, 439-448.

Holle, R. L., N. W. S. Demetriades, and A. Nag (2014), Lightning warnings with NLDN cloud and cloud-to-ground lightning data, Preprints, Fifth Int. Lightning Meteorology Conf./23rd Int. Lightning Detection Conf., Tucson, AZ. [Available online at http://www.vaisala.com/Vaisala%20Documents/Scientific%20papers/2014%20ILDC%20ILMC/ILMC-Friday/Holle%20et%20al-Lightning%20Warnings%20with%20NLDN-2014-ILDC-ILMC.pdf.]

Hudman, R. C., et al. (2007), Surface and lightning sources of nitrogen oxides over the United States: Magnitudes, chemical evolution, and outflow, *J. Geophys. Res.*, 112, D12S05, doi:10.1029/2006JD007912.

Huntrieser, H., H. Schlager, C. Feigl, and H. Höller (1998), Transport and production of NO_x in electrified thunderstorms: Survey of previous studies and new observations at midlatitudes, *J. Geophys. Res.,* 103, doi:10.1029/98JD02353.

Huntrieser, H., U. Schumann, H. Schlager, H., Höller, A. Giez, H.-D. Betz, D. Brunner, C. Forster, O. Pinto Jr., and R. Calheiros (2008), Lightning activity in Brazilian thunderstorms during TROCCINOX: Implications for NO_x production, *Atmos. Chem. Phys.,* 8, 921-953, doi:10.5194/acp-8-921-2008.

Huntrieser, H., et al. (2009), NOx production by lightning in Hector: First airborne measurements during SCOUT-O3/ACTIVE, *Atmos. Chem. Phys.,* 9, 8377-8412.

Huntrieser, H., H. Schlager, M. Lichtenstern, P. Stock, T. Hamburger, H. Höller, H., Schmidt, H.-D. Betz, A. Ulanovsky, et al. (2011), Mesoscale convective systems observed during AMMA and their impact on the NOx and O3 budget over West Africa, *Atmos. Chem. Phys.,* 11, doi:10.5194/acp-11-2503-2011.

Huntrieser, H., et al. (2016), On the origin of pronounced O3 gradients in the thunderstorm outflow region during DC3, *J. Geophys. Res. Atmos.,* 121,6600-6637, doi:10.1002/2015JD024279.

Iacono, M. J., J. S. Delamere, E. J. Mlawer, M. W. Shephard, S. A. Clough, and W. D. Collins (2008), Radiative forcing by long-lived greenhouse gases: Calculations with the AER radiative transfer models, *J. Geophys. Res.*, 113, D13103, doi:10.1029/2008JD009944.

Jayaratne, E. R., C. P. R. Saunders, and J. Hallett (1983), Laboratory studies of the charging of soft-hail during ice crystal interactions, *Q. J. R. Meteorol. Soc.*, 109, 609-630, doi:10.1002/qj.49710946111.

Jaeglé, L., D. J. Jacob, Y. Wang, A. J. Weinheimer, B. A. Ridley, T. L. Campos, G. W. Sachse, and D. E. Hagen (1998), Sources and chemistry of NO_x in the upper troposphere over the United States, *Geophys. Res. Lett.,* 25, doi:10.1029/97GL03591.

Koshak, W. (2014), Global lightning nitrogen oxides production, in *The Lightning Flash*, pp. 819-860, The Institution of Engineering and Technology, London, United Kingdom.

Koshak, W., H. Peterson, A. Biazar, M. Khan, and L. Wang (2014), The NASA Lightning Nitrogen Oxides Model (LNOM): Application to air quality modeling, *Atmos. Res.,* 135-136, 363-369, doi:10.1016/j.atmosres.2012.12.015.

Krehbiel, P. R., R. J. Thomas, W. Rison, T. Hamlin, J. Harlin, and M. Davis (2000), GPS-based mapping system reveals lightning inside storms, *EOS. Trans. AGU*, 81(3), 21-25, doi:10.1029/00EO00014.

Kuhlman, K. M., C. L. Ziegler, E. R. Mansell, D. R. MacGorman, and J. M. Straka (2006), Numerically simulated electrification and lightning of the 29 June 2000 STEPS supercell storm, *Mon. Wea. Rev.*, 134, 2734-2757.

Lacis, A. A., D. J. Wuebbles, and J. A. Logan (1990), Radiative forcing of climate by changes in the vertical distribution of ozone, *J. Geophys. Res.,* 95, 9971-9981, doi:10.1029/JD095iD07p09971.

LaJoie, M., and A. Laing (2008), The influence of the El Niño-Southern Oscillation on cloud-to-ground lightning activity along the Gulf Coast. Part 1: Lightning climatology. *Mon. Wea. Rev.,* 136, doi:10.1175/2007MWR2227.1.

Latham, J., W. A. Petersen, W. Deierling, and H. J. Christian (2007), Field identification of a unique globally dominant mechanism of thunderstorm electrification, *Q. J. R. Meteorol. Soc.*, *133*, 1453-1457, doi:10.1002/qj.133.

Lericos. T. P., H. E. Fuelberg, A. I. Watson, and R. Holle (2002), Warm season lightning distributions over the Florida peninsula as related to synoptic patterns, *Wea. Forecasting*, 17, 83-98.

Li, Y., K. E. Pickering, D. J. Allen, M. C. Barth, M. M. Bela, K. A. Cummings, L. D. Carey, R. M. Mecikalski, A. O. Fierro, T. L. Campos, A. J. Weinheimer, G. S. Diskin, and M. I. Biggerstaff (2017), Evaluation of deep convective transport in storms from different convective regimes during the DC3 field campaign using WRF-Chem with lightning data assimilation, *J. Geophys. Res. Atmos.*, in review.

Liaskos, C. E., D. J. Allen, and K. E. Pickering (2015), Sensitivity of tropical tropospheric composition to lightning NOx production as determined by replay simulations with GEOS-5, *J. Geophys., Res. Atmos.,* 120. 8512-8534, doi:10.1002/2014JD022987.

Liu, C., and S. Heckman (2011), The application of total lightning detection and cell tracking for severe weather prediction, Proc. Fifth Conference on the Meteorological Applications of Lightning Data, 91st Annual Meeting, AMS, Seattle, WA, 24-27 Jan.

Liu, C., D. J. Cecil, E. J. Zipser, K. Kronfeld, and R. Robertson (2012), Relationships between lightning flash rates and radar reflectivity vertical structures in thunderstorms over the tropics and subtropics, *J. Geophys. Res.*, 117, D06212, doi:10.1029/2011JD017123.

Liu, C., J. Anderson, and S. Heckman (2015), Lightning detection networks for commercial aviation – technology, meteorology and applications, In 2015 International Conference on Lightning and Static Electricity, Toulouse, France.

Lund, N. R., D. R. MacGorman, T. J. Schuur, M. I. Biggerstaff, and W. D. Rust (2009), Relationship between lightning location and polarimetric radar signatures in a small mesoscale convective system, *Mon. Wea. Rev.*, 127, 4151-4170, doi:10.1175/2009MWR2860.1.

MacGorman, D. R., and W. D. Rust (1998), *The Electrical Nature of Storms*, 422pp., Oxford Univ. Press, Oxford.

MacGorman, D. R., W. D. Rust, P. Krehbiel, W. Rison, E. Bruning, and K. Wiens (2005), The electrical structure of two supercell storms during STEPS, *Mon. Wea. Rev.*, 133, 2583-2607, doi:10.1175/MWR2994.1.

Magi, B. I. (2015), Global lightning parameterization from CMIP5 climate model output, *J. Atmos. Oceanic Technol.*, 32, 434-452, doi:10.1175/JTECH-D-13-00261.1.

Mansell, E. R., D. R. MacGorman, C. L. Ziegler, and J. M. Straka (2002), Simulated three-dimensional branched lightning in a numerical thunderstorm model, *J. Geophys. Res.*, 107, 4075, doi:10.1029/2000JD000244.

Mansell, E. R., D. R. MacGorman, C. L. Ziegler, and J. M. Straka (2005), Charge structure and lightning sensitivity in a simulated multicell thunderstorm, *J. Geophys. Res.*, 110, D012101, doi:10.1029/2004JD005287.

Mansell, E. R., C. L. Ziegler, and E. C. Bruning (2010), Simulated electrification of a small thunderstorm with two-moment bulk microphysics, *J. Atmos. Sci.,* 67, 171-194, doi:10.1175/2009JAS2965.1.

Marchand, M. R., and H. E. Fuelberg (2014), Assimilation of lightning data using a nudging method involving low-level warming, *Mon. Wea. Rev.,* 142, 4850–4871.

Martin, R. V., B. Sauvage, I. Folkins, C. E. Sioris, C. Boone, P. Bernath, and J. Ziemke (2007), Space-based constraints on the production of nitric oxide by lightning, *J. Geophys. Res.,* 112, doi:10.1029/2006JD007831.

Martini, M., D. J. Allen, K. E. Pickering, G. L. Stenchikov, A. Richter, E. J. Hyer, and C. J. Loughner (2011), The impact of North American anthropogenic emissions and lightning on long-range transport of trace gases and their export from the continent during summers 2002 and 2004, *J. Geophys. Res.,* 116, D07305, doi:10.1029/2010JD014305.

McCaul, Jr., E. W., K. Fuell, G. Stano, and J. Case (2011), Lightning Forecast Algorithm (LFA) overview, NASA Short-term Prediction Research and Transition Center (SPoRT) Training, October 2011.

McCaul, E. W., S. J. Goodman, K. M. LaCasse, and D. J. Cecil (2009), Forecasting lightning threat using cloud-resolved model simulations, *Weather Forecasting*, 24, 709-729, doi:10.1175/2008WAF2222152.1.

Mecikalski, R. M., and L. D. Carey (2017), Lightning characteristics relative to radar, altitude and temperature for a multicell, MCS, and supercell over northern Alabama, *Atmos. Res.*, 191, 128-140, doi:10.1016/j.atmosres.2017.03.001.

Mecikalski, R. M., A. L. Bain, and L. D. Carey (2015), Radar and lightning observations of deep moist convection across northern Alabama during DC3: 21 May 2012, *Mon. Wea. Rev.*, 143, 2774-2794, doi:10.1175/MWR-D-14-00250.1.

Monks, P. S. (2005), Gas-phase radical chemistry in the troposphere, *Chem. Soc. Rev.*, 34, 376-395, doi:10.1039/b307982c.

Morrison, H., and W. W. Grabowski (2008), A novel approach for representing ice microphysics in models: Description and tests using a kinematic framework, *J. Atmos. Sci.*, 65, 1528-1548, doi:10.1175/2007JAS2491.1.

Morrison, H., and J. A. Milbrandt (2011), Comparison of two-moment bulk microphysics schemes in idealized supercell thunderstorm simulations, *Mon. Wea. Rev.*, 139, 1103-1130, doi:10.1175/2010MWR3433.1.

Morrison, H., J. A. Milbrandt, G. H. Bryan, K. Ikeda, S. A. Tessendorf, and G. Thompson (2015), Parameterization of cloud microphysics based on the prediction of bulk ice particle properties. Part II: Case study comparisons with observations and other schemes, *J. Atmos. Sci.*, 72, 312-339, doi:10.1175/JAS-D-14-0066.1.

Nag, A., S. Mallick, V. A. Rakov, J. S. Howard, C. J. Biagi, J. D. Hill, M. A. Uman, D. M. Jordan, K. J. Rambo, J. E. Jerauld, B. A. DeCarlo, K. L. Cummins, and J. A. Cramer (2011), Evaluation of U.S. National Lightning Detection Network performance characteristics using rocket-triggered lightning data acquired in 2004-2009, *J. Geophys. Res.*, 116, D02123, doi:10.1029/2010JD014929.

Neu, J. L., and M. J. Prather (2012), Toward a more physical representation of precipitation scavenging in global chemistry models: Cloud overlap and ice physics and their impact on tropospheric ozone, *Atmos. Chem. Phys.,* 12(7), 3289-3310, doi:10.5194/acp-12-3289-2012.

Orville, R. E. (2008), Development of the National Lightning Detection Network, *Bull. Amer. Meteor., 89*, 180-190, doi:10.1175/BAMS-89-2-180.

Orville, R. E., and R. W. Henderson (1986), Global distribution of midnight lightning: September 1977 to August 1978, *Mon. Wea. Rev.*, 114, 2640-2653.

Ott, L. E., K. E. Pickering, G. L. Stenchikov, H. Huntrieser, and U. Schumann (2007), Effects of lightning NO_x production during the 21 July European Lightning Nitrogen Oxides Project storm studied with a three-dimensional cloud-scale chemical transport model, *J. Geophys. Res.,* 112, D05307, doi:10.1029/2006JD007365.

Ott, L. E., K. E. Pickering, G. L. Stenchikov, D. J. Allen, A. J. DeCaria, B. Ridley, R.-F. Lin, S. Lang, and W.-K. Tao (2010), Production of lightning NOx and its vertical distribution calculated from three-dimensional cloud-scale chemical transport model simulations, *J. Geophys. Res.,* 115, D04301, doi:10.1029/2009JD011880.

Padula, F., and S. Goodman (2016), GOES-R validation field campaign, paper presented at GOES-R Science Seminar.

Pan, L. L., et al. (2014), Thunderstorms enhance tropospheric ozone by wrapping and shedding stratospheric air, *Geophys. Res. Lett.,* 41, 7785-7790, doi:10.1002/2014GL061921.

Petersen, W. A., and S. A. Rutledge (2001), Regional variability in tropical convection: Observations from TRMM, *J. Clim.*, *14*, 3566-3586.

Petersen, W. A., H. J. Christian, and S. A. Rutledge (2005), TRMM observations of the global relationship between ice water content and lightning, *Geophys. Res. Lett.*, 32, L14819, doi:10.1029/2005GL023236.

Pickering, K. E., Y. Wang, W.-K. Tao, C. Price, and J.-F. Müller (1998), Vertical distributions of lightning NOx for use in regional and global chemical transport models, *J. Geophys. Res.*, 103(D23), 31203-31216, doi:10.1029/98JD02651.

Pickering, K. E., A. M. Thompson, R. R. Dickerson, W. T. Luke, D. P. McNamara, J. P. Greenberg, and P. R. Zimmerman (1990), Model calculations of tropospheric ozone production potential following observed convective events, *J. Geophys. Res.,* 95, D9, doi:10.1029/JD095iD09p14049.

Pickering, K. E., et al. (1996), Convective transport of biomass burning emissions over Brazil during TRACE A, *J. Geophys. Res.,* 101(D19), 23,993-24,012, doi:10.1029/96JD00346.

Pickering, K. E., E. Bucsela, D. A. Allen, K. A. Cummings, Y. Li, D. MacGorman, and E. Bruning (2014), Estimates of lightning NOx production per flash from OMI NO2 and lightning observations, paper presented at XV International Conference on Atmospheric Electricity, 15-20 June 2014, Norman, OK.

Pollack, I. B., et al. (2016), Airborne quantification of upper tropospheric NOx production from lightning in deep convective storms over the United States Great Plains, *J. Geophys. Res. Atmos.,* 121, 2002-2028, doi:10.1002/2015JD023941.

Preston, A. D., and H. E. Fuelberg (2015), Improving lightning cessation guidance using polarimetric radar data, *Wea. Forecasting*, 30, 308-328, doi:10.1175/WAF-D-14-00031.1.

Price, C. (2009), Will a drier climate result in more lightning? *Atmos. Res.*, 91, doi:10.1016/j.atmosres.2008.05.016.

Price, C., and D. Rind (1992), A simple lightning parameterization for calculating global lightning distributions, *J. Geophys. Res.*, 97(D9), 9919-9933, doi:10.1029/92JD00719.

Price, C., and D. Rind (1993), What determines the cloud-to-ground fraction in thunderstorms?, *Geophys. Res. Lett.,* 20, 463-466.

Price, C., J. Penner, and M. Prather (1997), NO_x from lightning. 1. Global distribution based on lightning physics, *J. Geophys. Res.*, 102, 5929-5941, doi:10.1029/96JD03504.

Rakov, V. A. (2016), *Fundamentals of Lightning*, 248pp., Cambridge Univ. Press, Cambridge.

Rakov, V. A., and M. A. Uman (2003) Lightning effects on the chemistry of the atmosphere, in *Lightning: Physics and effects*, pp. 507-527, Cambridge University Press, New York.

Reeve, N., and R. Toumi (1999), Lightning activity as an indicator of climate change, *Quart. J. Roy. Meteor. Soc.,* 125, 893-903.

Ridley, B. A., J. E. Dye, J. G. Walega, J. Zheng, F. E. Grahek, and W. Rison (1996), On the production of active nitrogen by thunderstorms over New Mexico, *J. Geophys. Res.,* 101, doi:10.1029/96JD01706.

Rison, W., R. J. Thomas, P. R. Krehbiel, T. Hamlin, and J. Harlin (1999), A GPS-based three-dimensional lightning mapping system: Initial observations in central New Mexico, *Geophys. Res. Lett.*, 26(23), 3573-3576, doi:10.1029/1999GL010856.

Roeder, W. P. and J. E. Glover (2005), Preliminary results from phase-1 of the statistical forecasting of lightning cessation project, paper presented at Conference on Meteorological Applications of Lightning Data, Am. Meteor. Soc., San Diego, CA.

Roeder, W. P., and T. M. McNamara (2011), Using temperature layered VIL as automated lightning warning guidance, paper presented at 5th Conference on Meteorological Applications of Lightning Data, Paper 688, 10 pp.

Roeder, W. P., L. L. Huddleston, W. H. Bauman III, and K. B. Doser (2014), Weather research requirements from Cape Canaveral Air Force Station and NASA Kennedy Space Center, paper presented at Space Traffic Management Conference, Daytona Beach, FL.

Romps, D. M., J. T. Seeley, D. Vollaro, and J. Molinari (2014), Projected increase in lightning strikes in the United States due to global warming, *Science,* 346(6211), 851-854, doi:10.1126/science.1259100.

Rossow, W. B., A. W. Walker, D. E. Beuschel, and M. D. Roiter (1996), International Satellite Cloud Climatology Project (ISCCP) documentation of new cloud data sets, WMO/TD 737, 115 pp., World Meteorol. Org., Geneva.

Rust, W. D., MacGorman, D. R., Bruning, E. C., Weiss, S. A., Krehbiel, P. R., Thomas, R. J., Rison, W., Hamlin, T., and Harlin, J.: Invert-polarity electrical structures in thunderstorms in the Severe Thunderstorm Electrification and Precipitation Study (STEPS), *Atmos. Res.*, 76, 247-271, doi:10.1016/j.atmosres.2004.11.029, 2005.

Saunders, M. (2012), Characteristics of WTLN-derived lightning, Honors theses, 26 pp., Dept. of Earth, Ocean, and Atmos. Sciences, Florida State Univ., Tallahassee, Florida. [Available at http://purl.flvc.org/fsu/fd/FSU_migr_uhm-0055.]

Saunders, C. P. R., W. D. Keith, and R. P. Mitzeva (1991), The effect of liquid water on thunderstorm charging, *J. Geophys. Res.*, 96(D6), 11007-11017, doi:10.1029/91JD00970.

Schroeder, J. R., L. L. Pan, T. Ryerson, G. Diskin, J. Hair, S. Meinardi, I. Simpson, B. Barletta, N. Blake, and D. R. Blake (2014), Evidence of mixing between polluted

convective outflow and stratospheric air in the upper troposphere during DC3, *J. Geophys. Res. Atmos.*, 119, 11,477-11,491, doi:10.1002/2014JD022109.

Schumann, U. and H. Huntrieser (2007), The global lightning-induced nitrogen oxides source, *Atmos. Chem. Phys.*, 7, 3823-3907, doi:10.5194/acp-7-3823-2007.

Schwartz, C. S., G. S. Romine, R. A. Sobash, K. R. Fossell, and M. L. Weisman (2015), NCAR's experimental real-time convection-allowing ensemble prediction system, *Wea. Forecasting*, 30, 1645-1653, doi:10.1175/WAF-D-15-0103.1.

Stano, G. T., H. E. Fuelberg, and W. P. Roeder (2010), Developing empirical lightning cessation forecast guidance for the Cape Canaveral Air Force Station and Kennedy Space Center, *J. Geophys. Res.*, 115, doi:10.1029/2009JD013034.

Starr, S., D. Sharp, F. Merceret, J. Madura, and M Murphy (1998), LDAR, a three-dimensional lightning warning system: Its development and use by the government, and transition to public availability, NASA contractor report, NASA, Kennedy Space Center, FL, 9 pp..

Stolzenburg, M., T. C. Marshall, W. D. Rust, E. Bruning, D. R. MacGorman, and T. Hamlin (2007), Electric field values observed near lightning flash initiations, *Geophys. Res. Lett.*, 34, L04804, doi:10.1029/2006GL028777.

Takahashi, T. (1978), Riming electrification as a charge generation mechanism in thunderstorms, *J. Atmos. Sci.*, 35(8), 1536-1548.

Thomas, R. J., P. R. Krehbiel, W. Rison, S. J. Hunyady, W. P. Winn, T. Hamlin, and J. Harlin (2004), Accuracy of the lightning mapping array, *J. Geophys. Res.*, 109, D14207, doi:10.1029/2004JD004549.

Turman, B. N. (1978), Analysis of lightning data from the DMSP satellite, *J. Geophys. Res.*, 83(C10), 5019-5024, doi:10.1029/JC083iC10p05019.

Uman, M. A. (2001), *The Lightning Discharge*, Dover Publications, Inc., Mineola, New York, 377 pp.

Van Weverberg, K. (2013), Impact of environmental instability on convective precipitation uncertainty associated with the nature of the rimed ice species in a bulk microphysics scheme, *Mon. Wea. Rev.*, 141, 2841-2849, doi:10.1175/MWR-D-13-00036.1.

Vivekanandan, J., D. S. Zrnic, S. Ellis, R. Oye, and A. V. Ryzhkov (1999), Cloud microphysics retrievals using S-band dual-polarization radar measurements, *Bull. Am. Meteorol. Soc.*, 80, 381-388.

Voiland, A. (2012), Fire in New Mexico, Available online at

https://earthobservatory.nasa.gov/NaturalHazards/view.php?id=78135, Accessed 22 August 2012.

Vu, K. T., et al. (2016), Impacts of the Denver Cyclone on regional air quality and aerosol formation in the Colorado Front Range during FRAPPÉ 2014, *Atmos. Chem. Phys.*, 16, 12039012058, doi:10.5194/acp-16-12039-2016.

Wallace, J. M. and Hobbs, P. V. (2006), Cloud Microphysics, in *Atmospheric Science: An introductory survey*, pp. 209-269, Academic Press, MA.

Watson, L. R. (2013), Range-specific high-resolution mesoscale model setup: Data assimilation, Final report, NASA Applied Meteorology Unit, Kennedy Space Center, FL, 41 pp.

Wiens, K. C., S. A. Rutledge, and S. A. Tessendorf (2005), The 29 June 2000 supercell observed during STEPS. Part II: Lightning and charge structure, *J. Atmos. Sci.*, 62(12), 4151-4177, doi:10.1175/JAS3615.1.

Wilczak, J. M., and T. W. Christian (1990), Case study of an orographically induced mesoscale vortex (Denver Cyclone), *Mon. Wea. Rev.*, 118, 1082-1102, doi:10.1175/1520-0493(1990)118<1082:CSOAOI>2.0.CO;2.

Wilczak, J. M., and J. W. Glendening (1988), Observations and mixed-layer modeling of a terrain-induced mesoscale gyre: The Denver Cyclone, *Mon. Wea. Rev.*, 116, 2688-2711, doi:10.1175/1520-0493(1988)116<2688:OAMLMO>2.0.CO;2.

Wilkinson, J. M., and F. J. Bornemann (2014), A lightning forecast for the London 2012 Olympics opening ceremony, *Weather*, 69, 16-19, doi:10.1002/wea.2176.

Williams, E. R. (1985), Large-scale charge separation in thunderclouds, *J. Geophys. Res.*, 90(D4), 6013-6025, doi:10.1029/JD090iD04p06013.

Williams, E. R. (2005), Lightning and climate: A review, *Atmos. Res.*, *76*, 272-287, doi:10.1016/j.atmosres.2004.11.014.

Wolf, P. (2006), Anticipating the initiation, cessation, and frequency of cloud-to-ground lightning, utilizing WSR-88D reflectivity data, *Electron. J. Oper. Meteor.*, 8(1), 1-19.

Wong, J., M. C. Barth, and D. Noone (2013), Evaluating a lightning parameterization based on cloud-top height for mesoscale numerical simulations, *Geosci. Model. Dev.*, *6*, 429-443, doi:10.5194/gmd-6-429-2013.

Woodard, C. J., L. D. Carey, W. A. Petersen, and W. P. Roeder (2012), Operational

utility of dual-polarimetric variables in lightning initiation forecasting, *Electron. J. Oper. Meteor.*, 13(6), 79-102.

Zhang, R., X. Tie, and D. W. Bond (2003), Impacts of anthropogenic and natural NO_x sources over the U.S. on tropospheric chemistry, *PNAS*, 100, doi:10.1073/pnas.252763799.

Ziegler, C. L. (2013a), A diabatic Lagrangian technique for the analysis of convective storms. Part I: Description and validation via an observing system simulation experiment*, J. Atmos. Oceanic Technol.,* 30, 2248-2265, doi:10.1175/JTECH-D-12-00194.1.

Ziegler, C. (2013b), NSSL MGAUS Oklahoma-Texas Sounding Data. Version 1.0. UCAR/NCAR - Earth Observing Laboratory. https://doi.org/10.5065/D63R0R84. Accessed 25 Feb 2014.

Zipser, E. J., and K. R. Lutz (1994), The vertical profile of radar reflectivity of convective cells: A strong indicator of storm intensity and lightning probability?, *Mon. Wea. Rev.*, 122(8), 1751-1759.